UNIVERSITÀ DI PARMA

UNIVERSITA' DEGLI STUDI DI PARMA

DOTTORATO DI RICERCA IN

Scienza e Tecnologia dei Materiali

CICLO XXXIV

Synthesis and Characterization of Nanostructured Calcium Phosphate Matrices for Biomedical and Environmental Applications

Coordinatore:

Chiar.mo Prof. Enrico Dalcanale, PhD

Tutore:

Chiar.mo Dott. Michele Iafisco, PhD

Dottoranda:

Francesca Carella

Anni Accademici 2018/2019 – 2021/2022

Table of contents

List of acronyms

A: Absorbance

ACP: Amorphous Calcium Phosphate

AM: Artificial Mucus

ATR: Attenuated total reflection

CaP: Calcium Phosphate

CF: Cystic Fibrosis

CFTR: Cystic Fibrosis Transmembrane conductance Regulator

CFU: Colony Forming Units

Col: Colistin

DLS: Dynamic Light Scattering

ECHA: European Chemicals Agency

ELS: Electrophoretic Light Scattering

FDA: Food and Drug Administration

FT-IR: Fourier Transform InfraRed spectroscopy

GI: Germination Index

HA: Hydroxyapatite

HPLC: High-Performance Liquid Chromatography

ICP-OES: Inductively Coupled Plasma – Optical Emission Spectrometry

LDCs: Least Developed Countries

MIC: Minimum Inhibitory Concentration

NPs: NanoParticles

OCE: Octocrylene

OCN: Octinoxate

OCP: OctaCalcium Phosphate

PA: Pseudomonas Aeruginosa

PAD: Padimate O

PDI: PolyDispersity Index

RhB: Rhodamine B

ROS: Reactive Oxygen Species

RT: Room Temperature

SEM-FEG: Scanning Electron Microscopy - Field Emission Gun

SILF: Simulated Interstitial Lung Fluid

SPF: Sun Protection Factor

SSA: Specific Surface Area

TCP: Tri-Calcium Phosphate

TEM: Transmission Electron Microscope

TGA: ThermoGravimetric Analysis

UV: Ultraviolet

UV-Vis: UV–visible spectrophotometry

XRD: X-ray Diffraction

ZP: Zeta Potential

Aim of the work

Calcium phosphates (CaPs) constitute the inorganic component of hard tissues in vertebrates (e.g., bones and teeth) and they are widely present in nature as vertebrate bones, mammalian teeth, and fish scales or in milk and blood as the principal calcium source. It is well-known that the main application of CaPs is in medicine, where they are used as biomaterials in orthopedics for regenerating or replacing bone tissue or as drug delivery systems. However, the high tunability of this material and the excellent properties of CaPs made them a versatile material that can also be useful in other fields. CaPs can be prepared by chemical synthesis and also from biogenic sources. Focusing on the food wastes, the rapid growth of the fish industry has increased the interest to face the high amount of fish waste to be treated. Therefore, the evaluation of fish bones as a source of CaPs has recently gained the attention of researchers.

For these reasons, one of the goals of this Ph.D. thesis consisted in the preparation of CaPs with synthetic methods or extracted by biogenic materials. The second main task consists in the evaluation of the obtained CaPs for biomedical applications and other innovative fields that are not connected to the medical topic. Starting from the biomedical field, CaPs were used as porous scaffold for hard tissue engineering or as drug delivery system. Regarding the innovative fields, CaPs were prepared to be an innovative ingredient for sunscreen formulations for the cosmetic field, and a controlled-release fertilizer and thus as a natural phosphorous source for the agriculture field.

In detail, the first part of the research work consisted in the design, preparation, and evaluation *in vitro* of a new therapeutic formulation based on inhalable and biodegradable CaP NPs functionalized with Colistin (Col) for the cystic fibrosis treatment. The material was prepared by wet chemical processes, and once achieved the optimized Col functionalization, the final material was physically, and chemically characterized. Moreover, in vitro experiments were also conducted to evaluate its biocompatibility, antimicrobial and antibiofilm efficacy.

The second part of the Ph.D. thesis was focused on the production of a 3D macroporous scaffold from natural sources (mussel shells) for bone regeneration application. Mussel shells were chosen as a natural $CaCO_3$ source and, therefore, as a precursor of CaP

powder. This powder was employed to prepare porous scaffolds by direct foaming method. Finally, both powders and 3D structures were characterized, and the mechanical properties of the scaffolds were also investigated.

In the third part of this Ph.D. thesis, a novel and safe CaP-based ingredient for sunscreen formulations was designed, prepared and optimized from natural sources (fish bones). In particular, this work was divided in three main parts: i) the preparation of a natural CaP derived from fish bone industry waste; ii) the determination of the best interaction between CaP and UV-filters; and iii) the optimization of the booster effect of CaP by using the doping process. The physical and chemical properties of the obtained powders were explored through different methods of characterization and the SPF booster performances were determined by the SPF in vitro analysis. Finally, to evaluate the variations made by the presence of CaP in the formulations, an accelerated stability study was carried out on marketable creams.

The last part of this thesis was focused on the development of a circular economy for P reuse. In particular, CaP-based waste materials were easily processed and tested for fertilizer application in agriculture. This obtained materials are designed to be used as phosphorous “delivery systems” for plant. The thermal conversion of fish bones leads to the production of CaP-based fertilizers and bio stimulants for plant growth. The obtained CaPs were characterized from the physical-chemical point of view and then tested as bio stimulants and as fertilizers.

1. Introduction

1.1. Calcium Phosphates: a multifunctional class of materials

Calcium phosphates (CaPs) are a family of materials and minerals that constitute the inorganic component of hard tissues in vertebrates (e.g., bones and teeth). They are present in nature as vertebrate bones, mammalian teeth, and fish scales or in milk and blood as the principal calcium source.[1,2] The main application of CaPs is in medicine, where they are used as biomaterials in orthopedics for regenerating or replacing bone tissue, or as drug delivery systems. This is possible because of their excellent biological properties like high biocompatibility, bioactivity, lack of toxicity or inflammatory and immunity responses, osteoconductivity, osteoinductivity and bioresorbability.[3] In particular, the high biocompatibility of CaPs is due to their chemical and structural similarity to the mineral phase of bone, which allow to be recognized by the body as a sort of endogenous material. Moreover, the physical and chemical characteristics of CaPs such as crystal phases, particle size, morphology, crystallinity, porosity, density, composition, Ca/P atomic ratio, or pH stability range, are related to their functions and can be tailored modifying the parameters in CaP synthesis.[4–6] Notably, the preparation of different CaP crystal phases induces the achievement of different morphologies, chemical compositions, or structures (Figure 1.1).[4–6]

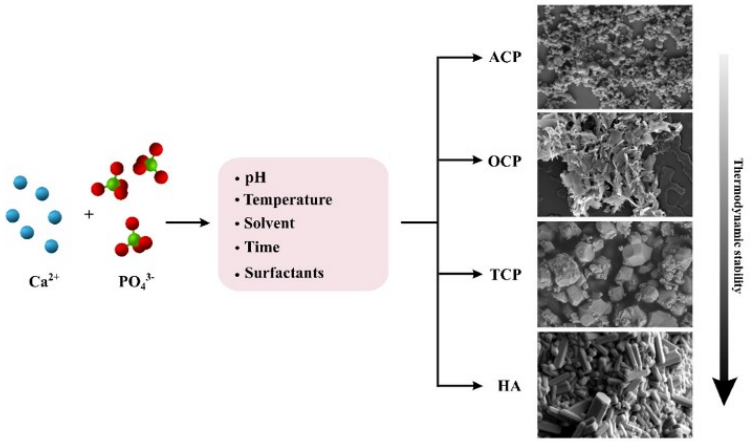

Figure 1.1 - Principal synthesis parameters that influence the characteristics of calcium phosphates as well as the formation of different crystal phases (ACP: amorphous calcium phosphate, OCP: octacalcium phosphate, TCP: tricalcium phosphate, HA: hydroxyapatite, respectively).[7]

Part of the content of this chapter was published as E. Campodoni "Design and development of bio-hybrid multifunctional materials for regenerative medicine", L. Degli Esposti "Tailoring calcium phosphate nanoparticles for medical applications: a functional by design approach", F. Carella, L. Degli Esposti, et al. "The Use of Calcium Phosphates in Cosmetics, State of the Art
and Future Perspectives", and F. Carella, M. Seck, L. Degli Esposti, et al. "Thermal conversion of fish bones into fertilizers and biostimulants for plant growth – A low tech valorization process for the development of circular economy in least developed countries".

1.2. Description of the most relevant calcium phosphate phases

In this section, the main proprieties, and functions of the four more relevant CaP phases, previously reported in Figure 1.1, will be described.

1.2.1. Amorphous Calcium Phosphate

Amorphous calcium phosphate (ACP) is a non-crystalline CaP phase ($Ca_9(PO_4)_6$) and represents the mineral precursor for bone and tooth formation in vertebrates.[8,9] It is characterized by an excellent bioactivity, osteoconductivity, high cell adhesion, and tailorable biodegradation. Moreover, it is a non-crystalline phase, and for this reason it is more soluble than the crystalline CaPs, releasing a higher amount of calcium and phosphate ions in a short time span. This latter property has been harnessed in the dental field, leading to the development of ion-releasing oral care products containing ACP that trigger enamel and dentin remineralization, restoring the mineral loss caused by caries.[10–14] Commonly, ACP is obtained by a wet precipitation in an aqueous environment, even though precipitations in ethanol or by sol-gel processes were also reported.[15] It is necessary to use high supersaturation conditions, additives, and fast precipitation times in order to produce an amorphous product. ACP is not characterized by a precise stoichiometry, and on the basis of the precipitation conditions its Ca/P molar ratio ranges from 1.18 to 2.50.[16] ACP is an highly unstable CaP phase, and it easily transforms into crystalline CaPs such as octacalcium phosphate (OCP) and hydroxyapatite (HA). This is due to the high structural similarity in the short-range order of ACP with OCP or HA, and in presence of water or moisture it rearranges spontaneously to form a crystalline lattice. The crystallization process is affected by many factors, such as pH, temperature, humidity, and the presence of ions/additives.[15,16] As the superior ion-releasing properties of ACP are lost with the spontaneous crystallization, many studies were conducted to stabilize ACP in the long term to enhance its shelf-life. The most common stabilizers of ACP are ions such as Mg^{2+}, CO_3^{2-} and $P_2O_7^{4-}$, as they hinder crystalline lattice formation.[17,18] Otherwise, other common stabilizers are organic molecules that attach to the ACP surface and inhibit the dissolution–reprecipitation mechanisms of crystallization. Among them, the most successful stabilizers are casein phosphopeptide, which is a milk protein, or citrate, which is a relatively abundant organic molecule of bone.[3,15,16,19–24] The

main application of this CaP phase regards the biomedical field, in which it has found application as bone repair material in self-setting injectable cements, in the preparation of coatings on metallic or polymeric bone implants, and as drug delivery platform.[15,16,25,26]

1.2.2. Octacalcium Phosphate

Octacalcium phosphate (OCP) is a CaP with formula $Ca_8H_2(PO_4)\cdot 6.5H_2O$, which has found successful application in bone-related biomaterials.[3,20,21,27–29] It is thought that OCP is a precursor of biogenic HA in hard tissues of vertebrates.[27,30] Indeed, OCP triclinic structure is very similar to the hexagonal structure of HA. It is composed of "apatitic layers" that have the same atomic arrangement of HA intercalated by "hydrated layers" that contain water molecules.[3,20,21,27–29] As a consequence of this, OCP diffraction pattern closely resembles HA diffraction pattern, except for the presence of the high intensity (100) peak at very low diffraction angle. Moreover, OCP has good osteoconductivity and it can convert into HA through a dissolution–reprecipitation mechanism or a topotaxial conversion mechanism.[27] Synthetic OCP can be obtained by wet precipitation at neutral or mildly acidic pH or by the hydrolysis of α-tricalcium phosphate (TCP) or dicalcium phosphate.[27] Interestingly, the Ca/P molar ratio of OCP (1.33) is variable and can change according to the quantity of calcium present in the structure. Its structure could be both Ca-deficient (Ca/P 1.26), or it can present an excess of calcium (Ca/P up to 1.48).[4]

1.2.3. Tricalcium Phosphate

Tricalcium phosphate (TCP) is characterized by the chemical formula $Ca_3(PO_4)_2$ and a Ca/P ratio of 1.50.[4] TCP exists in two allotropic forms that have same chemical composition but different structure, density, and solubility: α-TCP and β-TCP. The latter allotropic form is the more thermodynamically stable, but usually is further stabilized by including magnesium ions into calcium ion vacancy. β-TCP has a lower interfacial energy than HA, and for this reason, it can induce the precipitation of an apatitic layer in aqueous ionic solutions. Moreover, it is osteoconductive and osteoinductive.[31] On the other hand, α-TCP has similar properties, but it is more soluble and reactive than β-TCP.[3,20,21,32–34] Usually, TCPs are obtained by high-temperature solid-state reaction of solid Ca and P precursors (e.g., calcium carbonate and ammonium hydrogen phosphate), or by thermal

transformation of CaP precursors with a Ca/P molar ratio equal to 1.50 (calcium-deficient hydroxyapatite or ACP). Depending on the reaction temperature, a different allotropic form can be produced. Indeed, to obtain β-TCP, the CaP precursors are calcined at 700–800 °C, while to achieve α-TCP the process temperature increases up to 1200 °C. In addition, α-TCP could also be prepared by thermal transformation of crystalline β-TCP. This process represents the most direct and simplest approach to produce α-TCP.[33,35–37] TCPs, especially α-TCP, founds their main application in biomedical fields as self-setting CaP cements. Cements are formed when TCP or a blend of CaP powders are mixed with an aqueous solution, obtaining a viscous paste that can be injected in the bone defect and progressively hardens in situ, restoring mechanical resistance.[38] The hardening is due to the hydrolysis of TCP that recrystallizes into HA, as the newly formed crystallites interlock with one another during growth, forming a hard conglomerate.[39]

1.2.4. Hydroxyapatite

Among all the other CaP phases, hydroxyapatite (HA) is the most used CaP phase because it is the most thermodynamically stable phase in physiological conditions. It is the mineral phase of vertebrate bones, mammalian teeth, and fish scales, it has the formula of $Ca_{10}(PO_4)_6(OH)_2$ and a Ca/P ratio of 1.67. The HA hexagonal crystal structure, reported in Figure 1.2, contains calcium ions in two different crystallography symmetry sites in its unit cell, called Ca(I) and Ca(II).

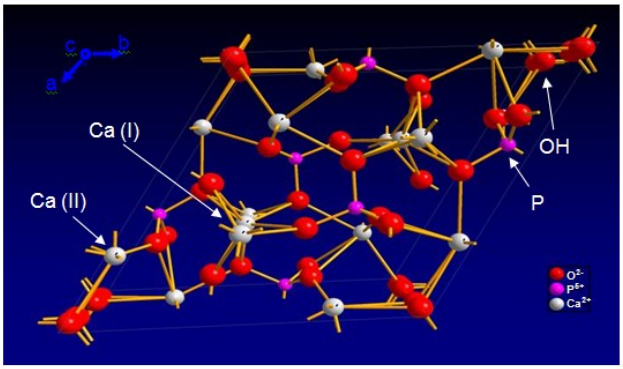

Figure 1.2 – HA hexagonal crystal structure in which are visible the position of Ca^{2+} divided in the two different symmetry sites: Ca(I) and Ca(II), P^{5+} and O^{2-} ions.[40]

As represented in Figure 1.2, Ca(I) ions site is identified by columns along the three-fold axes, and each Ca(I) ion is nine-coordinated with O atoms. On the other hand, Ca(II) ions are seven-coordinated, with six O atoms and one OH^- ion.[41–43] A peculiarity of HA

structure consists in its highly flexibility and its capacity to tolerate high lattice distortion. This allows the incorporation of substituting ions replacing Ca^{2+}, PO_4^{3-} or OH^- ions, without introducing modification in HA crystalline structure.[44–48] However, the ionic substitutions can greatly alter HA properties, e.g., increase HA solubility, bioactivity, stability, or impart additional capabilities such as magnetic sensitivity or luminescence.[3,20,21,32,49] Commonly, HA is synthesized so as to have the same crystallinity, chemical composition, ion doping, size, and morphology of the biogenic minerals, which in this case is defined as biomimetic HA.[50] It is worth to mention that biological and biomimetic HAs are non-stoichiometric, indeed they contain foreign doping ions in their hexagonal structure such as Na^+, K^+, Mg^{2+}, Sr^{2+}, $Fe^{2+/3+}$, Zn^{2+}, CO_3^{2-}, Cl^-, or F^-.[3,20,21,32,49] Among others, carbonate doping is one of the most common substitutions and it could be carried out in two different ways. Indeed, CO_3^{2-} ions substitution can be an A-type when it substitutes OH^- ions or it can be a B-type when it substitutes PO_4^{3-} ions.[51–53] In particular, type B carbonate-HA is characterized by higher reactivity and lower crystallinity, and it is present in young bones. In contrary, type A carbonate-HA is present in mature bones, and it shows lower reactivity and higher crystallinity.[54] Another important ion substitution is the magnesium one, which affect the HA biological activity, increasing the HA nucleation and inhibiting the HA crystallization.[52] Typically, HA is characterized by several features, such as superior bioactivity, osteoconductivity, non-toxicity, non-immunogenicity, and biocompatibility in comparison to other CaP phases.[50] Moreover, another peculiar feature of HA is its pH-dependent water solubility. This material is stable in alkaline solutions, poorly soluble at neutrality and soluble at acidic pH.[55–57] Therefore, this pH sensitivity can be harnessed for pH-triggered drug delivery applications, where a drug associated to HA is released only when the material encounters an acidic environment, as in the cases of inflammatory regions or in endosomes and lysosomes after cellular intake.[58] Furthermore, it has also been demonstrated that HA nanocrystal size and morphology can significantly affect its biocompatibility, bioactivity, and cell and tissue penetration capability.[59–62]

The high tunability of this material for its use in several kind of applications has led toward the increase of the interest in the study of this material. For these reasons, one of the goals of this thesis consisted in the preparation of HA. Both traditional and more innovative methods were studied obtaining different HA principally based material, which were then tested for several applications.

1.3. CaPs preparation: common methods and innovative solutions

As previously mentioned, all the functions of CaPs and thus their final application are tightly related to their physicochemical characteristics, such as particle size, morphology, crystallinity, porosity, density, composition, Ca/P atomic ratio, or pH stability range. These characteristics can be tailored by modifying the parameters in CaP synthesis.[4–6] The preparation of CaPs could be achieved following several methods and they can be derived from both synthetic precursors and natural sources. In the next sections there were reported the most common methods of CaPs productions and the innovative ones, accordingly with the literature.[63–73] In particular, Sadat-Shojai at el. have reported in their review a comparison between the CaPs preparation methods in term of process cost.[71] On the other hand, Shavandi et al.[66] and Agbeboh et al.[63] have described advantages and disadvantages of each method of preparation in their reviews. Eventually, Bee et al.[72] and Mohd Pu'Ad et al.[65] have described in detail the preparation of CaPs from biogenic sources, while Terzioglu et al.[73] have reported the CaPs extraction from a huge variety of fishes.

1.3.1. Preparation of CaPs with synthetic methods

The synthetic preparation of CaPs could be classified in wet methods, dry methods, hydrothermal methods or high temperature processes, and combined methods (Figure 1.3).

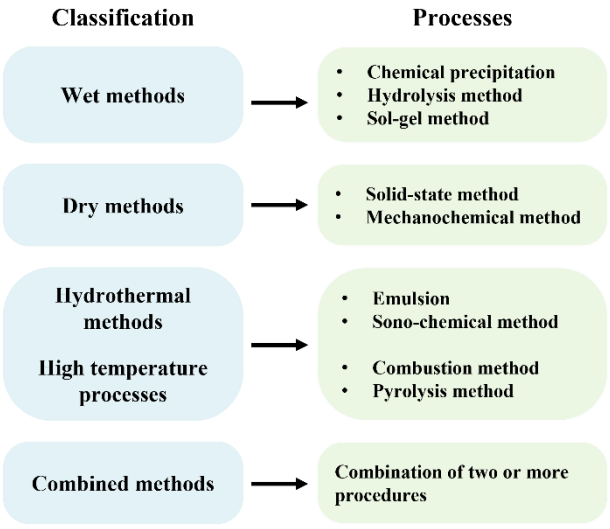

Figure 1.3 - Scheme of the classification of synthetic methods for CaP preparation.

Figure 1.3 shows the main processes that belongs at each synthetic method classified, accordingly with the already published literature.[63,64,66–71] Briefly, wet methods are well known as wet chemical precipitation methods, and they are commonly used to achieve CaPs with nanosized structure and a regular morphology.[63,67,71] These methods involve the reaction between chemical precursors in solution, that could be carried out at different temperatures or pressure, with several solvents and by varying apparatus or chemicals.[64,67,69] On the other hand, dry methods do not require the use of any solvent. Commonly, the precursors utilized in these latter methods are mixed mechanochemically to produce CaPs. Moreover, dry methods are not affected by processing parameters, thus they do not necessitate of controlled conditions during the synthesis.[63,64,67,69–71] Furthermore, hydrothermal methods are basically a wet chemical precipitation conducted at elevated pressure and temperatures. The high temperature characteristic of this process lead to an increase of the crystallinity of the final CaP material.[64,67,69,71] In the high-temperature processes, instead, the temperature is raised so as to completely or partially burn the precursors. In the case of combustion, it is a redox chemical reaction between an oxidant (calcium nitrate and HNO_3) and an organic molecule (urea, hydrazine, citric acid, and glycine) in aqueous medium. This led to the degradation of precursors and the production of CaPs. In the case of pyrolysis, instead, CaPs can form from a gas phase of reactants which was generated by the physical evaporation of liquid precursors.[64,67,70,71] Finally, the combination method consists in the mix of two or more previously described methods.

1.3.2. Preparation of CaPs from biogenic sources

As previously described, CaPs are widely present in nature and they are the main mineral phase in vertebrate bones, mammalian teeth, and fish scales. Therefore, CaPs cannot be only synthesized by chemical reactions, but they can be also prepared with several ways from biogenic sources. According to the literature, the extraction of biominerals from biowastes is the most well-known method for the preparation of CaPs using biogenic sources.[63,65,66,71–73] The conversion of these by-products in high added value products, applying the principles of circular economy, is nowadays a significant topic for social, environmental, and economic reasons. Indeed, the management and disposal of food waste are becoming a huge issue generating concerns not only for the economic point of

view but also for aquatic and terrestrial environments.[73] Among all the biowastes that could be used for the CaPs production, which are fully explained in the reviews by Sadat-Shojai et al.,[71] Mohd Pu'ad et al.[65] and Agbeboh et al.[63], this thesis focused its attention on food industry by-products (Figure 1.4).

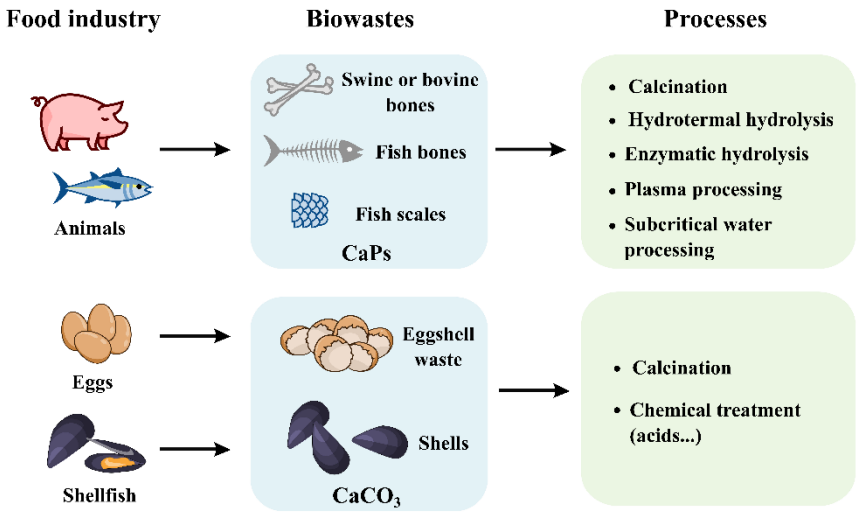

Figure 1.4 - Scheme of the preparation of calcium phosphates from food industry by-product sources.[7]

As reported in Figure 1.4, animal bones constituted mainly by CaPs are subjected to the organic components removal by thermal treatment to obtain CaPs.[74] On the other hand, eggshells or seashells made of calcium carbonate ($CaCO_3$), are usually thermal treated to convert $CaCO_3$ in CaO. Eventually, CaPs were achieved by a further precipitation with a phosphorus source.[75]

Focusing on the food wastes, the rapid growth of the fish industry has increased the interest to face the high amount of fish waste to be treated. Indeed, in the fish industry roughly > 91 million tons of fish and shellfish are consumed annually and the fish by-products account about 40–50% of the total fish caught.[73] For these reasons, the evaluation of fish bones as a source of CaPs has recently gained the attention of researchers which want to take the advantage of producing a high added value and high-quality bioengineering material.[73]

1.4. Common and innovative applications of CaPs

As described above, CaP can be modified by varying the synthesis parameters. This results in CaP-based materials with different chemical and physical properties that can be used for different types of applications. Commonly, CaPs are extensively used in the

biomedical field. However, the excellent properties of CaPs made them a versatile material that can also be useful in other fields. For example, CaPs could be used as controlled-release fertilizer or bio-stimulant in agriculture, catalyst, anticorrosive material for paintings, flame retardant agent, etc.[76–79]

One of the main purposes of this thesis thus consists in the preparation of CaP and the study of their application in biomedical as well as "not-conventional" fields. Starting from the more common biomedical field, CaPs were used as porous scaffold for hard tissue engineering or as drug delivery system (Figure 1.5A). Regarding the other fields, CaPs were prepared to be an innovative ingredient for sunscreen formulations in cosmetic, and a controlled-release fertilizer and thus a natural phosphorous source for the agriculture field (Figure 1.5B-C).

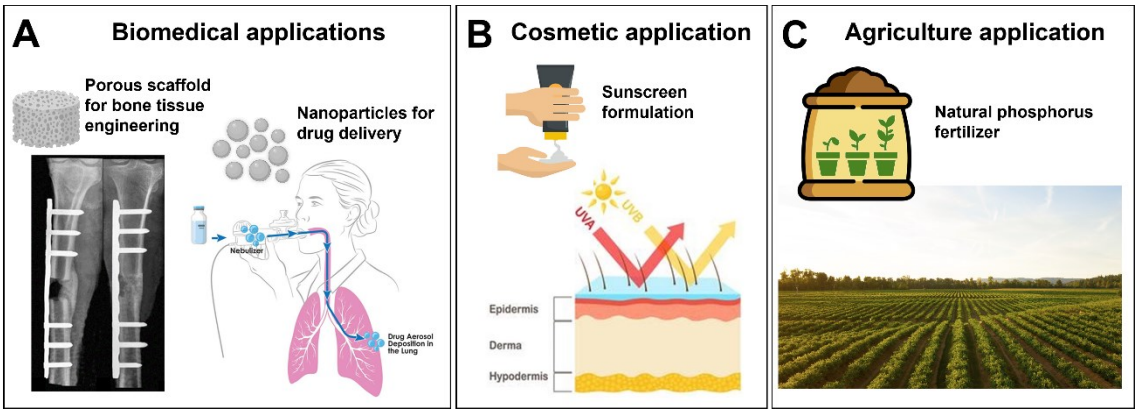

Figure 1.5 – CaP applications reported along this thesis: (A) biomedical, (B) cosmetic and (C) agriculture.

1.4.1. Biomedical applications

The biomedical field is the most studied sector of application of CaPs because they can be recognized by the body as a sort of endogenous material. Indeed, as previously reported, their chemical and structural similarity to the mineral phase of bone, is the reason for their high biocompatibility. In comparison to other materials used in orthopedics, CaPs have a higher osteoconductivity and osteoinductivity, do not induce immune responses or rejections preserving the bone-implant interface, and can stimulate bone self-healing.[80,81] In the last 50 years CaPs were used as: (i) bone replacement as three-dimensional massive bioceramics or scaffolds, (ii) as injectable self-hardening cements to fill bone defects for setting exogenous implants, (iii) as filling material in soft bio-composites and hybrid biomaterials, or (iv) as coating for metallic and polymeric

protheses.[4,19,82–84] In the case of massive CaP bioceramics, a limitation for their wider use in clinical application is related to their poor mechanical properties. Pure CaPs are characterized by being fragile, as they have both low impact resistance and low tensile stress (6 to 10 MPa), making them unsuitable for replacing bone (which has a tensile strength of 50 to 150 MPa in the case of cortical bone).[3] For these reasons, they can be used in the form of powder or cements combined with several elements, such as Fe, Ag, Cu, Mg, Mn, Sr or Zn, or are reinforced with polymers to form bio-hybrid composites.[85–90] One of the most successful applications of CaPs is as coatings of metallic or polymeric implants that have poor osteoconductivity to improve their integration with the bone.[91–96] The CaP coating can initiate a bioactive fixation of the prothesis after surgery and increase the long-term activity of the implant, and at the same time limit the fibrous tissue encapsulation around it. In addition, CaPs in the form of nanoparticles (NPs) were recently proposed as innovative materials in nanomedicine, to treat diseases not related to bone (i.e., cardiovascular diseases, cancer, etc.), harnessing their superior biocompatibility for drug delivery applications.[58,97–99] One of the main aims of the drug delivery systems is to convey a poorly bioavailable drug to the target tissue using the capability of a nanomaterial to cross biological barriers and to avoid its early clearance.[100] CaP NPs are interesting vectors for drug delivery since they can load a high variety of bioactive molecules, thus protecting the therapeutic agent from degradation in the biological environment before reaching their target site.[101–104]

In this thesis the CaP materials were optimized and studied for two biomedical applications. The first material reported was a CaP NPs-based drug delivery system developed as an inhalable formulation, while the second was a 3D porous scaffold developed for the bone regeneration.

1.4.2. Cosmetic application

An innovative application field in which CaPs could represent an excellent alternative to several currently used ingredients is the cosmetic field.

Cosmetics, as defined by the U.S. Food and Drug Administration (FDA), are substances for application to the human body aimed at cleansing, beautifying, promoting attractiveness or altering the appearance without affecting the body physiology or functions.[105] In particular, it refers to every substance placed in contact with an external part of the

human body or with the teeth and the mucous membranes of the oral cavity with the aim of cleaning, protecting, perfuming or changing their appearance.[106–108] Due to the rapid development of the petrochemical industry over the last two centuries, nowadays synthetic cosmetic materials are mass-produced and diffused worldwide.[109] During the XX century, toxic heavy metals were found in cosmetics as contaminations or impurities. Various research works report a direct relationship between chronic exposure to heavy metals in cosmetics and health problems such as skin sensitivities, allergic reactions, contact dermatitis, hair loss, respiratory disorders, cardiovascular diseases, gastrointestinal disorders, fertility problems, cancer, and even death.[110,111] The European Regulation no.1223/2009/EC permits the presence of traces of heavy metals in the finished products if it is technically inevitable. Such presence is tolerated only if the safety of the product is demonstrated and if good manufacturing practices are employed. However, in the regulation there are no precise limits of the quantity of metals tolerated in a cosmetic product, even if as a rule of thumb their concentration must be kept as low as possible. Indeed, every government is demanded to enforce limits on impurities content in cosmetic products on sale. An example is reported by the German Federal Government, which has determined appropriate limits for metal contained as impurities in cosmetics, such as 5 μg/g for As and Cd, 1 μg/g for Hg, 20 μg/g for Pb and 10 μg/g for Sb.[112,113] Another example is represented by the limits for elements present as impurities in cosmetic products imposed by the Government of Canada, which are 3 μg/g for As, Cd and Hg, 10 μg/g for Pb, and 5 μg/g for Sb.[112,114] The safety of cosmetics means not only to avoid as much as possible the presence of heavy metals, but also to ensure that the product has an adequate microbiological purity and stability.[115] For this purpose, producers usually use preservatives such as parabens, which are biodegradable and do not change the consistency or colour of products. According to different regulatory agencies such as the FDA and the European Chemicals Agency (ECHA), parabens are considered safe, but several works report that a continuous use of cosmetics containing this class of compounds can be harmful for the human body.[106,116–119] Other categories of compounds used in cosmetics for several purposes, such as UV filters for their photoprotective action or microplastics for their texture-extending and feel-modifying abilities, raise concerns both from the consumer health and environmental perspectives. For instance, in the marine environment, these chemicals can damage fragile and

precious ecosystems such as coral reef, causing a loss of biodiversity, and can bioaccumulate in the consumed fish species, again endangering human health.[120–124] To address these health and environmental concerns, it is therefore necessary to produce and use innovative, natural, and safe ingredients that have high biocompatibility and biodegradability and are non-toxic.

For these reasons, in this thesis a novel and safe CaP-based ingredient for sunscreen formulations was designed, prepared and optimized. In particular, it was studied a material able to enhance the sun protection factor (SPF) of a solar formulation, called "SPF booster".

1.4.3. Agriculture application

Another innovative application of CaPs consists in their use as fertilizers in agriculture.

Nowadays, it is very challenging to meet the food and nutritional needs of the world's ever-growing population without the extensive application of fertilizers.[125] For this reason, the increased demand for them has led to an increase of fertilizers' cost. In particular, these materials usually include both macronutrient (N, P, K, Ca, Mg and S) and micronutrient (Zn, Cu, Mn, Fe, B and Mo) in their formulations.[125] Among the other elements, P is the eleventh most abundant in the world, but its accessibility is low. The largest amount of P could be found in natural deposits. However, these are not always known, and mining them is very expensive or technically not feasible (e.g., submarine sediments).[126] Moreover, the import of this element contains uncertainties for different reasons: i) many countries with P mines are politically unstable; ii) natural deposits could contain a high concentration of hazardous chemical elements (Cd, Pb, Hg, U Cr, As, etc.), that are expensive to remove;[127] iii) the production of P is high water demand.[126] Furthermore, it is known that the leaching of P-based fertilizer from agriculture fields and the discharge of wastewater containing high amounts of P, cause the eutrophication phenomenon, which does not have yet a suitable solution.[128]

For these reasons, it is of fundamental importance to design and develop the circular economy of this element and enlarge its pool of resources with alternative and renewable ones for meeting future P demands and environmental conservation. In literature many reviews described overviews focused on technologies for the P recovery.[129–136] Recently,

the use of calcium phosphates for agricultural applications has gained attention due to their environmental safety, biocompatibility and because they contain P.[137]

In this thesis, the need to develop a circular economy for P reuse was addressed. in particular, CaP-based waste materials were processed and tested for fertilizer application in agriculture.

References:

1. McLean, F. C. & Hinrichs, M. A. The formation and behavior of colloidal calcium phosphate in the blood. *Am. J. Physiol. Content* **121**, 580–588 (1938).
2. Gaucheron, F. The minerals of milk. *Reprod. Nutr. Dev.* **45**, 473–483 (2005).
3. Eliaz, N. & Metoki, N. Calcium Phosphate Bioceramics: A Review of Their History, Structure, Properties, Coating Technologies and Biomedical Applications. *Materials (Basel).* **10**, 334 (2017).
4. Dorozhkin, S. V. Nanosized and nanocrystalline calcium orthophosphates. *Acta Biomater.* **6**, 715–734 (2010).
5. Bose, S. & Tarafder, S. Calcium phosphate ceramic systems in growth factor and drug delivery for bone tissue engineering: A review. *Acta Biomater.* **8**, 1401–1421 (2012).
6. Drouet, C. *et al.* Nanocrystalline apatites: From powders to biomaterials. *Powder Technol.* **190**, 118–122 (2009).
7. Carella, F., Degli Esposti, L., Adamiano, A. & Iafisco, M. The Use of Calcium Phosphates in Cosmetics, State of the Art and Future Perspectives. *Materials (Basel).* **14**, 6398 (2021).
8. Robinson, C. *et al.* Subunit Structures in Hydroxyapatite Crystal Development in Enamel: Implications for Amelogenesis Imperfecta. *Connect. Tissue Res.* **44**, 65–71 (2003).
9. Beniash, E., Metzler, R. A., Lam, R. S. K. & Gilbert, P. U. P. A. Transient amorphous calcium phosphate in forming enamel. *J. Struct. Biol.* **166**, 133–143 (2009).
10. Zhao, J., Liu, Y., Sun, W. & Zhang, H. Amorphous calcium phosphate and its application in dentistry. *Chem. Cent. J.* **5**, 40 (2011).
11. Cochrane, N. J., Cai, F., Huq, N. L., Burrow, M. F. & Reynolds, E. C. New Approaches to Enhanced Remineralization of Tooth Enamel. *J. Dent. Res.* **89**, 1187–1197 (2010).
12. Li, J. *et al.* Long-term remineralizing effect of casein phosphopeptide-amorphous calcium phosphate (CPP-ACP) on early caries lesions in vivo: A systematic review. *J. Dent.* **42**, 769–777 (2014).
13. Rahiotis, C. & Vougiouklakis, G. Effect of a CPP-ACP agent on the demineralization and remineralization of dentine in vitro. *J. Dent.* **35**, 695–698 (2007).
14. Poggio, C., Lombardini, M., Vigorelli, P. & Ceci, M. Analysis of dentin/enamel

remineralization by a CPP-ACP paste: AFM and SEM study. *Scanning* **35**, 366–374 (2013).

15. Combes, C. & Rey, C. Amorphous calcium phosphates: Synthesis, properties and uses in biomaterials. *Acta Biomater.* **6**, 3362–3378 (2010).
16. Dorozhkin, S. V. Amorphous calcium (ortho)phosphates. *Acta Biomater.* **6**, 4457–4475 (2010).
17. Boskey, A. L. & Posner, A. S. Magnesium stabilization of amorphous calcium phosphate: A kinetic study. *Mater. Res. Bull.* **9**, 907–916 (1974).
18. Fleisch, H., Russell, R. G. G., Bisaz, S., Termine, J. D. & Posner, A. S. Influence of pyrophosphate on the transformation of amorphous to crystalline calcium phosphate. *Calcif. Tissue Res.* **2**, 49–59 (1968).
19. Sun, R. *et al.* Highly Porous Amorphous Calcium Phosphate for Drug Delivery and Bio-Medical Applications. *Nanomaterials* **10**, 20 (2019).
20. Dorozhkin, S. V. Calcium orthophosphates. *J. Mater. Sci.* **42**, 1061–1095 (2007).
21. Wang, L. & Nancollas, G. H. Calcium Orthophosphates: Crystallization and Dissolution. *Chem. Rev.* **108**, 4628–4669 (2008).
22. Vecstaudza, J., Gasik, M. & Locs, J. Amorphous calcium phosphate materials: Formation, structure and thermal behaviour. *J. Eur. Ceram. Soc.* **39**, 1642–1649 (2019).
23. Yengopal, V. & Mickenautsch, S. Caries preventive effect of casein phosphopeptide-amorphous calcium phosphate (CPP-ACP): a meta-analysis. *Acta Odontol. Scand.* **67**, 321–332 (2009).
24. Iafisco, M. *et al.* Fluoride-doped amorphous calcium phosphate nanoparticles as a promising biomimetic material for dental remineralization. *Sci. Rep.* **8**, 17016 (2018).
25. Ito, T. *et al.* Preparation of injectable auto-forming alginate gel containing simvastatin with amorphous calcium phosphate as a controlled release medium and their therapeutic effect in osteoporosis model rat. *J. Mater. Sci. Mater. Med.* **23**, 1291–1297 (2012).
26. Zhao, J., Liu, Y., Sun, W. & Yang, X. First detection, characterization, and application of amorphous calcium phosphate in dentistry. *J. Dent. Sci.* **7**, 316–323 (2012).
27. Suzuki, O. Octacalcium phosphate: Osteoconductivity and crystal chemistry. *Acta*

Biomater. **6**, 3379–3387 (2010).

28. Komlev, V. S. *et al.* Synthesis of octacalcium phosphate by precipitation from solution. *Dokl. Chem.* **432**, 178–182 (2010).
29. Monma, H. Preparation of octacalcium phosphate by the hydrolysis of α-tricalcium phosphate. *J. Mater. Sci.* **15**, 2428–2434 (1980).
30. Dorozhkin, S. V. Bioceramics of calcium orthophosphates. *Biomaterials* **31**, 1465–1485 (2010).
31. Kotani, S. *et al.* Bone bonding mechanism of β-tricalcium phosphate. *J. Biomed. Mater. Res.* **25**, 1303–1315 (1991).
32. Kumta, P. N., Sfeir, C., Lee, D.-H., Olton, D. & Choi, D. Nanostructured calcium phosphates for biomedical applications: novel synthesis and characterization. *Acta Biomater.* **1**, 65–83 (2005).
33. Carrodeguas, R. G. & De Aza, S. α-Tricalcium phosphate: Synthesis, properties and biomedical applications. *Acta Biomater.* **7**, 3536–3546 (2011).
34. Moseke, C. & Gbureck, U. Tetracalcium phosphate: Synthesis, properties and biomedical applications. *Acta Biomater.* **6**, 3815–3823 (2010).
35. Bohner, M., Santoni, B. L. G. & Döbelin, N. β-Tricalcium Phosphate for Bone Substitution: Synthesis and Properties. *Acta Biomater.* (2020) doi:10.1016/j.actbio.2020.06.022.
36. Famery, R., Richard, N. & Boch, P. Preparation of α- and β-tricalcium phosphate ceramics, with and without magnesium addition. *Ceram. Int.* **20**, 327–336 (1994).
37. Xue, W., Dahlquist, K., Banerjee, A., Bandyopadhyay, A. & Bose, S. Synthesis and characterization of tricalcium phosphate with Zn and Mg based dopants. *J. Mater. Sci. Mater. Med.* **19**, 2669–2677 (2008).
38. Dorozhkin, S. V. Calcium orthophosphate cements for biomedical application. *J. Mater. Sci.* **43**, 3028–3057 (2008).
39. Dorozhkin, S. Calcium Orthophosphate Cements and Concretes. *Materials (Basel).* **2**, 221–291 (2009).
40. Eric M. Rivera-Muñoz. Hydroxyapatite-Based Materials: Synthesis and Characterization. in *Biomedical Engineering - Frontiers and Challenges* (InTech, 2011). doi:10.5772/19123.
41. Ran, J. *et al.* Comparisons among Mg, Zn, Sr, and Si doped nano-

hydroxyapatite/chitosan composites for load-bearing bone tissue engineering applications. *Mater. Chem. Front.* **1**, 900–910 (2017).

42. Marchegiani, F. *et al.* Hydroxyapatite synthesis from biogenic calcite single crystals into phosphate solutions at ambient conditions. *J. Cryst. Growth* **311**, 4219–4225 (2009).
43. Jokić, B. *et al.* Synthesis and characterization of monetite and hydroxyapatite whiskers obtained by a hydrothermal method. *Ceram. Int.* **37**, 167–173 (2011).
44. Uskoković, V. Ion-doped hydroxyapatite: An impasse or the road to follow? *Ceram. Int.* **46**, 11443–11465 (2020).
45. Iafisco, M., Ruffini, A., Adamiano, A., Sprio, S. & Tampieri, A. Biomimetic magnesium–carbonate-apatite nanocrystals endowed with strontium ions as anti-osteoporotic trigger. *Mater. Sci. Eng. C* **35**, 212–219 (2014).
46. Tampieri, A., Celotti, G. & Landi, E. From biomimetic apatites to biologically inspired composites. *Anal. Bioanal. Chem.* **381**, 568–576 (2005).
47. Šupová, M. Substituted hydroxyapatites for biomedical applications: A review. *Ceram. Int.* **41**, 9203–9231 (2015).
48. Boanini, E., Gazzano, M. & Bigi, A. Ionic substitutions in calcium phosphates synthesized at low temperature. *Acta Biomater.* **6**, 1882–1894 (2010).
49. Ibrahim, M., Labaki, M., Giraudon, J.-M. & Lamonier, J.-F. Hydroxyapatite, a multifunctional material for air, water and soil pollution control: A review. *J. Hazard. Mater.* **383**, 121139 (2020).
50. Dorozhkin, S. V. Calcium orthophosphates (CaPO4): occurrence and properties. *Prog. Biomater.* **5**, 9–70 (2016).
51. Spence, G., Patel, N., Brooks, R. & Rushton, N. Carbonate substituted hydroxyapatite: Resorption by osteoclasts modifies the osteoblastic response. *J. Biomed. Mater. Res. Part A* **90A**, 217–224 (2009).
52. Siddiqi, S. A. & Azhar, U. Carbonate substituted hydroxyapatite. in *Handbook of Ionic Substituted Hydroxyapatites* 149–173 (Elsevier, 2020). doi:10.1016/B978-0-08-102834-6.00006-9.
53. Gibson, I. R. & Bonfield, W. Novel synthesis and characterization of an AB-type carbonate-substituted hydroxyapatite. *J. Biomed. Mater. Res.* **59**, 697–708 (2002).
54. Landi, E., Tampieri, A., Celotti, G., Vichi, L. & Sandri, M. Influence of synthesis and

sintering parameters on the characteristics of carbonate apatite. *Biomaterials* **25**, 1763–1770 (2004).

55. Wagner, M., Hess, T. & Zakowiecki, D. Studies on the pH-dependent solubility of various grades of calcium phosphate-based pharmaceutical excipients. *J. Pharm. Sci.* (2021) doi:10.1016/j.xphs.2021.12.005.
56. Lelli, M. *et al.* Hydroxyapatite nanocrystals as a smart, pH sensitive, delivery system for kiteplatin. *Dalt. Trans.* **45**, 13187–13195 (2016).
57. Bharath, G. *et al.* Mesoporous hydroxyapatite nanoplate arrays as pH-sensitive drug carrier for cancer therapy. *Mater. Res. Express* **6**, 085409 (2019).
58. Degli Esposti, L., Carella, F., Adamiano, A., Tampieri, A. & Iafisco, M. Calcium phosphate-based nanosystems for advanced targeted nanomedicine. *Drug Dev. Ind. Pharm.* **44**, 1223–1238 (2018).
59. dos Anjos, S. *et al.* Impact of crystallinity and crystal size of nanostructured carbonated hydroxyapatite on pre-osteoblast in vitro biocompatibility. *J. Biomed. Mater. Res. Part A* **107**, 1965–1976 (2019).
60. Zhou, H. & Lee, J. Nanoscale hydroxyapatite particles for bone tissue engineering. *Acta Biomater.* **7**, 2769–2781 (2011).
61. Kramer, E., Podurgiel, J. & Wei, M. Control of hydroxyapatite nanoparticle morphology using wet synthesis techniques: Reactant addition rate effects. *Mater. Lett.* **131**, 145–147 (2014).
62. Chen, L., Mccrate, J. M., Lee, J. C.-M. & Li, H. The role of surface charge on the uptake and biocompatibility of hydroxyapatite nanoparticles with osteoblast cells. *Nanotechnology* **22**, 105708 (2011).
63. Agbeboh, N. I. *et al.* Environmentally sustainable processes for the synthesis of hydroxyapatite. *Heliyon* **6**, e03765 (2020).
64. Szcześ, A., Hołysz, L. & Chibowski, E. Synthesis of hydroxyapatite for biomedical applications. *Adv. Colloid Interface Sci.* **249**, 321–330 (2017).
65. Mohd Pu'ad, N. A. S., Koshy, P., Abdullah, H. Z., Idris, M. I. & Lee, T. C. Syntheses of hydroxyapatite from natural sources. *Heliyon* **5**, e01588 (2019).
66. Shavandi, A., Bekhit, A. E.-D. A., Sun, Z. F. & Ali, A. A Review of Synthesis Methods, Properties and Use of Hydroxyapatite as a Substitute of Bone. *J. Biomimetics, Biomater. Biomed. Eng.* **25**, 98–117 (2015).

67. Panda, S., Biswas, C. K. & Paul, S. A comprehensive review on the preparation and application of calcium hydroxyapatite: A special focus on atomic doping methods for bone tissue engineering. *Ceram. Int.* **47**, 28122–28144 (2021).

68. Nayak, A. Hydroxyapatite synthesis methodologies: An overview. *Int. J. ChemTech Res.* **2**, 903–907 (2010).

69. Fihri, A., Len, C., Varma, R. S. & Solhy, A. Hydroxyapatite: A review of syntheses, structure and applications in heterogeneous catalysis. *Coord. Chem. Rev.* **347**, 48–76 (2017).

70. Lu, B.-Q. & Zhu, Y.-J. One-dimensional hydroxyapatite materials: preparation and applications. *Can. J. Chem.* **95**, 1091–1102 (2017).

71. Sadat-Shojai, M., Khorasani, M.-T., Dinpanah-Khoshdargi, E. & Jamshidi, A. Synthesis methods for nanosized hydroxyapatite with diverse structures. *Acta Biomater.* **9**, 7591–7621 (2013).

72. Bee, S.-L. & Hamid, Z. A. A. Hydroxyapatite derived from food industry bio-wastes: Syntheses, properties and its potential multifunctional applications. *Ceram. Int.* **46**, 17149–17175 (2020).

73. Terzioğlu, P., Öğüt, H. & Kalemtaş, A. Natural calcium phosphates from fish bones and their potential biomedical applications. *Mater. Sci. Eng. C* **91**, 899–911 (2018).

74. Ideia, P. *et al.* Extraction and characterization of hydroxyapatite-based materials from grey triggerfish skin and black scabbardfish bones. *Int. J. Appl. Ceram. Technol.* **18**, 235–243 (2021).

75. Scialla, S. *et al.* Mussel Shell-Derived Macroporous 3D Scaffold: Characterization and Optimization Study of a Bioceramic from the Circular Economy. *Mar. Drugs* **18**, 309 (2020).

76. Yoon, H. Y. *et al.* Synergistic Release of Crop Nutrients and Stimulants from Hydroxyapatite Nanoparticles Functionalized with Humic Substances: Toward a Multifunctional Nanofertilizer. *ACS Omega* acsomega.9b04354 (2020) doi:10.1021/acsomega.9b04354.

77. Marchiol, L., Iafisco, M., Fellet, G. & Adamiano, A. Nanotechnology support the next agricultural revolution: Perspectives to enhancement of nutrient use efficiency. in (2020). doi:10.1016/bs.agron.2019.12.001.

78. Carella, F. *et al.* Thermal conversion of fish bones into fertilizers and biostimulants

for plant growth – A low tech valorization process for the development of circular economy in least developed countries. *J. Environ. Chem. Eng.* **9**, 104815 (2021).

79. Adamiano, A. *et al.* Calcium Phosphate Particles Coated with Humic Substances: A Potential Plant Biostimulant from Circular Economy. *Molecules* **26**, 2810 (2021).
80. Lu, J., Yu, H. & Chen, C. Biological properties of calcium phosphate biomaterials for bone repair: a review. *RSC Adv.* **8**, 2015–2033 (2018).
81. Hannink, G. & Arts, J. J. C. Bioresorbability, porosity and mechanical strength of bone substitutes: What is optimal for bone regeneration? *Injury* **42**, S22–S25 (2011).
82. Verron, E., Khairoun, I., Guicheux, J. & Bouler, J.-M. Calcium phosphate biomaterials as bone drug delivery systems: a review. *Drug Discov. Today* **15**, 547–552 (2010).
83. Epple, M. Review of potential health risks associated with nanoscopic calcium phosphate. *Acta Biomater.* **77**, 1–14 (2018).
84. WANG, Z., TANG, Z., QING, F., HONG, Y. & ZHANG, X. APPLICATIONS OF CALCIUM PHOSPHATE NANOPARTICLES IN POROUS HARD TISSUE ENGINEERING SCAFFOLDS. *Nano* **07**, 1230004 (2012).
85. O'Neill, R. *et al.* Critical review: Injectability of calcium phosphate pastes and cements. *Acta Biomater.* **50**, 1–19 (2017).
86. Ambard, A. J. & Mueninghoff, L. Calcium Phosphate Cement: Review of Mechanical and Biological Properties. *J. Prosthodont.* **15**, 321–328 (2006).
87. Xu, H. H. *et al.* Calcium phosphate cements for bone engineering and their biological properties. *Bone Res.* **5**, 17056 (2017).
88. Ginebra, M.-P., Canal, C., Espanol, M., Pastorino, D. & Montufar, E. B. Calcium phosphate cements as drug delivery materials. *Adv. Drug Deliv. Rev.* **64**, 1090–1110 (2012).
89. Boehm, A. V., Meininger, S., Gbureck, U. & Müller, F. A. Self-healing capacity of fiber-reinforced calcium phosphate cements. *Sci. Rep.* **10**, 9430 (2020).
90. Zhang, J., Liu, W., Schnitzler, V., Tancret, F. & Bouler, J.-M. Calcium phosphate cements for bone substitution: Chemistry, handling and mechanical properties. *Acta Biomater.* **10**, 1035–1049 (2014).
91. Makkar, P., Kang, H. J., Padalhin, A. R., Faruq, O. & Lee, B. In-vitro and in-vivo

evaluation of strontium doped calcium phosphate coatings on biodegradable magnesium alloy for bone applications. *Appl. Surf. Sci.* **510**, 145333 (2020).

92. Ge, X. *et al.* Controllable phase transformation of fluoridated calcium phosphate ultrathin coatings for biomedical applications. *J. Alloys Compd.* **847**, 155920 (2020).
93. Paital, S. R. & Dahotre, N. B. Calcium phosphate coatings for bio-implant applications: Materials, performance factors, and methodologies. *Mater. Sci. Eng. R Reports* **66**, 1–70 (2009).
94. Leòn, B. & A. Jahnsen, J. *Thin Calcium Phosphate Coatings for Medical Implants*. (Springer New York, 2009). doi:10.1007/978-0-387-77718-4.
95. YANG, Y., KIM, K. & ONG, J. A review on calcium phosphate coatings produced using a sputtering process?an alternative to plasma spraying. *Biomaterials* **26**, 327–337 (2005).
96. de Groot, K., Wolke, J. G. C. & Jansen, J. A. Calcium phosphate coatings for medical implants. *Proc. Inst. Mech. Eng. Part H J. Eng. Med.* **212**, 137–147 (1998).
97. Velino, C. *et al.* Nanomedicine Approaches for the Pulmonary Treatment of Cystic Fibrosis. *Front. Bioeng. Biotechnol.* **7**, (2019).
98. Adamiano, A. *et al.* Magnetic calcium phosphates nanocomposites for the intracellular hyperthermia of cancers of bone and brain. *Nanomedicine* **14**, (2019).
99. Miragoli, M. *et al.* Inhalation of peptide-loaded nanoparticles improves heart failure. *Sci. Transl. Med.* **10**, eaan6205 (2018).
100. Blanco, E., Shen, H. & Ferrari, M. Principles of nanoparticle design for overcoming biological barriers to drug delivery. *Nat. Biotechnol.* **33**, 941–951 (2015).
101. Doane, T. L. & Burda, C. The unique role of nanoparticles in nanomedicine: imaging, drug delivery and therapy. *Chem. Soc. Rev.* **41**, 2885 (2012).
102. Davis, M. E., Chen, Z. & Shin, D. M. Nanoparticle therapeutics: an emerging treatment modality for cancer. *Nat. Rev. Drug Discov.* **7**, 771–782 (2008).
103. Peer, D. *et al.* Nanocarriers as an emerging platform for cancer therapy. *Nat. Nanotechnol.* **2**, 751–760 (2007).
104. Mostaghaci, B., Loretz, B. & Lehr, C.-M. Calcium Phosphate System for Gene Delivery: Historical Background and Emerging Opportunities. *Curr. Pharm. Des.* **22**, 1529–1533 (2016).
105. Cosmetics Overview. https://www.fda.gov/industry/regulated-

products/cosmetics-overview.

106. Matwiejczuk, N., Galicka, A. & Brzóska, M. M. Review of the safety of application of cosmetic products containing parabens. *J. Appl. Toxicol.* **40**, 176–210 (2020).

107. Mesko, M. F., Novo, D. L. R., Costa, V. C., Henn, A. S. & Flores, E. M. M. Toxic and potentially toxic elements determination in cosmetics used for make-up: A critical review. *Anal. Chim. Acta* **1098**, 1–26 (2020).

108. Blanco-Dàvila, F. Beauty and the Body: The Origins of Cosmetics. *Plast. Reconstr. Surg.* **105**, 1196–1204 (2000).

109. Zhao, L. & Zhu, H. The research status of cosmetics and the establishment of biological beautiology. *Life Sci. J.* **17**, 5–11 (2020).

110. Bilal, M. & Iqbal, H. M. N. An insight into toxicity and human-health-related adverse consequences of cosmeceuticals—a review. *Sci. Total Environ.* **670**, 555–568 (2019).

111. Lim, D. S. *et al.* Non-cancer, cancer, and dermal sensitization risk assessment of heavy metals in cosmetics. *J. Toxicol. Environ. Heal. Part A* **81**, 432–452 (2018).

112. Bocca, B., Pino, A., Alimonti, A. & Forte, G. Toxic metals contained in cosmetics: A status report. *Regul. Toxicol. Pharmacol.* **68**, 447–467 (2014).

113. Germany reduces heavy metal limits in cosmetics. https://www.cosmeticsdesign-europe.com/Article/2017/07/25/Germany-reduces-heavy-metal-limits-in-cosmetics?utm_source=copyright&utm_medium=OnSite&utm_campaign=copyright.

114. Guidance on Heavy Metal Impurities in Cosmetics - Canada.ca. https://www.canada.ca/en/health-canada/services/consumer-product-safety/reports-publications/industry-professionals/guidance-heavy-metal-impurities-cosmetics.html.

115. Bashir, A. & Lambert, P. Microbiological study of used cosmetic products: highlighting possible impact on consumer health. *J. Appl. Microbiol.* **128**, 598–605 (2020).

116. Feizi, R., Jaafarzadeh, N., Akbari, H. & Jorfi, S. Evaluation of lead and cadmium concentrations in lipstick and eye pencil cosmetics. *Environ. Heal. Eng. Manag.* **6**, 277–282 (2019).

117. Khan, A. D. & MN, A. COSMETICS AND THEIR ASSOCIATED ADVERSE EFFECTS: A

REVIEW. *J. Appl. Pharm. Sci. Res.* **2**, (2019).

118. Bilal, M., Mehmood, S. & Iqbal, H. M. N. The Beast of Beauty: Environmental and Health Concerns of Toxic Components in Cosmetics. *Cosmetics* **7**, 13 (2020).
119. Bhardwaj, M., Masand, N., Sahoo, J. & Patil, V. M. Risk Assessment of Cosmetic Preservatives Using QSAR. *Int. J. Quant. Struct. Relationships* **5**, 44–62 (2020).
120. Moeller, M. *et al.* Challenges in Current Coral Reef Protection – Possible Impacts of UV Filters Used in Sunscreens, a Critical Review. *Front. Mar. Sci.* **8**, (2021).
121. Miller, I. B. *et al.* Toxic effects of UV filters from sunscreens on coral reefs revisited: regulatory aspects for "reef safe" products. *Environ. Sci. Eur.* **33**, 74 (2021).
122. Watkins, Y. S. D. & Sallach, J. B. Investigating the exposure and impact of chemical UV filters on coral reef ecosystems: Review and research gap prioritization. *Integr. Environ. Assess. Manag.* **17**, 967–981 (2021).
123. Corinaldesi, C., Marcellini, F., Nepote, E., Damiani, E. & Danovaro, R. Impact of inorganic UV filters contained in sunscreen products on tropical stony corals (Acropora spp.). *Sci. Total Environ.* **637**–**638**, 1279–1285 (2018).
124. Danovaro, R. *et al.* Sunscreens Cause Coral Bleaching by Promoting Viral Infections. *Environ. Health Perspect.* **116**, 441–447 (2008).
125. Sharma, S. *et al.* Porous nanomaterials: Main vein of agricultural nanotechnology. *Prog. Mater. Sci.* **121**, 100812 (2021).
126. Römer, W. & Steingrobe, B. Fertilizer Effect of Phosphorus Recycling Products. *Sustainability* **10**, 1166 (2018).
127. Chandrajith, R. & Dissanayake, C. B. Phosphate mineral fertilizers, trace metals and human health. *J. Natl. Sci. Found. Sri Lanka* **37**, 153 (2009).
128. Oliveira, M. & Machado, A. V. The role of phosphorus on eutrophication: a historical review and future perspectives. *Environ. Technol. Rev.* **2**, 117–127 (2013).
129. Sun, D., Hale, L., Kar, G., Soolanayakanahally, R. & Adl, S. Phosphorus recovery and reuse by pyrolysis: Applications for agriculture and environment. *Chemosphere* **194**, 682–691 (2018).
130. Shakoor, M. B., Ye, Z.-L. & Chen, S. Engineered biochars for recovering phosphate and ammonium from wastewater: A review. *Sci. Total Environ.* **779**, 146240 (2021).
131. Perera, M. K., Englehardt, J. D. & Dvorak, A. C. Technologies for Recovering Nutrients from Wastewater: A Critical Review. *Environ. Eng. Sci.* **36**, 511–529

(2019).

132. Günther, S., Grunert, M. & Müller, S. Overview of recent advances in phosphorus recovery for fertilizer production. *Eng. Life Sci.* **18**, 434–439 (2018).

133. Li, B. *et al.* Phosphorous recovery through struvite crystallization: Challenges for future design. *Sci. Total Environ.* **648**, 1244–1256 (2019).

134. Patel, A., Mungray, A. A. & Mungray, A. K. Technologies for the recovery of nutrients, water and energy from human urine: A review. *Chemosphere* **259**, 127372 (2020).

135. Pathy, A., Ray, J. & Paramasivan, B. Challenges and opportunities of nutrient recovery from human urine using biochar for fertilizer applications. *J. Clean. Prod.* **304**, 127019 (2021).

136. Liu, H. *et al.* Phosphorus recovery from municipal sludge-derived ash and hydrochar through wet-chemical technology: A review towards sustainable waste management. *Chem. Eng. J.* **417**, 129300 (2021).

137. Gilbert, N. Environment: The disappearing nutrient. *Nature* **461**, 716–718 (2009).

2. Analytical methods

The description of the fundamental principles of most of the techniques reported in this section was inspired by other previously published PhD theses focused on similar materials.[1–4]

2.1. Attenuated total reflection

Attenuated total reflection (ATR) is a sampling method commonly used with the Fourier transform infrared (FT-IR) spectroscopy, which is a very useful technique for recognizing vibrational transitions of functional groups contained in samples produced by the absorption of infrared radiation by the sample. Indeed, even if present in completely different molecules, functional groups are easily recognizable because they are characterized by three fixed parameters: i) position (linked to vibrational energy), ii) intensity (related to the efficiency of energy transfer) and iii) shape of the peaks (influenced by interactions with the chemical environment). For this reason, this technique is often used on a qualitative level, while the quantitative method is underused.

The main advantage of ATR consists in the possibility to directly examine samples in solid or liquid state without any kind of sample preparation. For example, solid samples are usually firmly clamped in contact to the ATR crystal to remove trapped air that could reduce the signal intensity. Usually, ATR crystals could be made by diamond that is an optimal material for this purpose due to its excellent mechanical properties and its high refractive index. Moreover, this sampling technique prevents the strong attenuation of the IR signal in a highly absorbing solution due to the limited path length into the sample. In particular, ATR takes advantage of the evanescent wave resulting from the total internal reflection. Indeed, an infrared light beam passed through the ATR crystal reflecting at least once on the internal surface in contact with the sample and this phenomenon produces the evanescent wave which expands into the sample. Finally, the resulting beam is collected by a detector (Figure 2.1).[5,6]

Part of the content of this chapter has been published in Journal of Environmental Chemical Engineering 2021, 9 (1), 104815 as "Carella F., Seck M., et al. Thermal conversion of fish bones into fertilizers and biostimulants for plant growth – A low tech valorization process for the development of circular economy in least developed countries", in Molecules 2021, 26 (9), 2810 as "Adamiano A., Fellet G., et al Calcium Phosphate Particles Coated with Humic Substances: A Potential Plant Biostimulant from Circular Economy", and in Marine Drugs 2020, 18 (6), 309 as "Scialla S., Carella F., et al. Mussel Shell-Derived Macroporous 3D Scaffold: Characterization and Optimization Study of a Bioceramic from the Circular Economy"

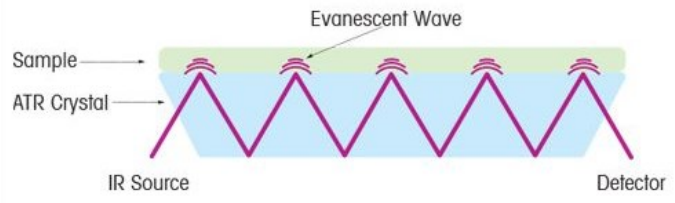

Figure 2.1 – ATR operation diagram which shows the infrared light beam that is reflected in the crystal forming the evanescent wave in the sample.

In this thesis, FTIR–ATR analyses to characterize the samples composition were performed using a Nicolet iS5 spectrometer (Thermo Fisher Scientific Inc., Waltham, MA, USA) with a resolution of 4 cm^{-1} by accumulation of 16 scans covering the 4000 to 400 cm^{-1} range, using a diamond ATR accessory model iD7.

2.2. Inductively coupled plasma – optical emission spectrometry

Inductively coupled plasma – optical emission spectrometry (ICP-OES) is a technique by which is possible to quantify elemental traces contained in liquid samples. Solid samples, instead, require an acid dissolution and elements extraction, or acid digestion so as to make analytes available in the final solution. Once prepared, the sample solution is nebulized in the spray chamber,[7] immediately vaporized by plasma, and then analysed.

The plasma is composed by ionized argon gas generated at the end of the quartz torch by an electrical spark applied for a short time in combination with a high-frequency electric current supplied in the induction coil.[8] Plasma has high temperature (almost 10.000K in the centre) and high energy used for the excitation-emission of the sample. Indeed, when the high energy is given to the sample, its component atomic elements initially convert atoms into ions and subsequently promote them to excited states. The return in the ground energy position of these elements, develop emission photon which have characteristic energies determined by the quantized energy level structure for the atoms or ions. By elaborating the photons wavelength, is possible to recognize the concentrations of elements contained in the sample, thanks to the direct proportion between the intensity of the signal and the amount of photon.

In an ICP-OES instrument, the direction in which the emission photons are collected, filtered and, detected could be decided between radial or axial. In particular, in radial mode the observation zone is a lateral (90°) view of the plasma plume, instead in the axial

mode it is a top view of the plasma plume. This latter observation zone gains in sensitivity but also could increase the interferences intensity, especially when complex matrices are analysed.[9] Figure 2.2 shows an ICP-OES instrument scheme with radial configuration of the detection system.

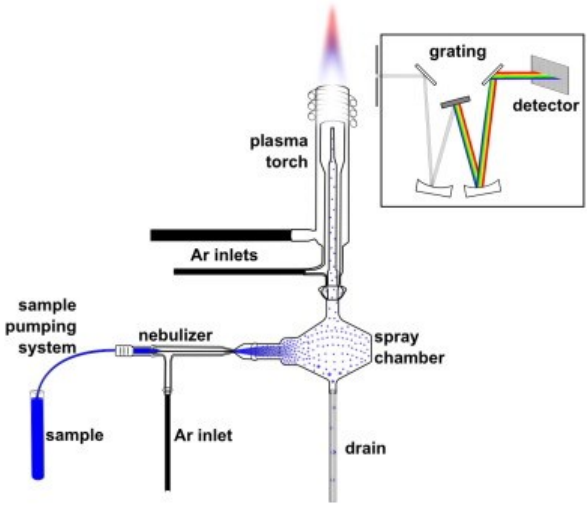

Figure 2.2 - ICP-OES instrument scheme with radial configuration of the detection system.[9]

The instrument utilized in this thesis for the element quantification was a Liberty 200 spectrometer (Agilent Technologies 5100 ICP–OES, Varian, Palo Alto, Santa Clara, CA USA). Most of the sample preparation was performed by dissolving 10mg of sample powder in 50mL of 1 wt. % HNO_3 solution. On the other hand, few samples (commonly natural sources) were dissolved by microwave assisted digestion. Briefly, 10 mg of sample, 5 mL of HNO_3 (65.0 wt.%) and 1 mL of H_2O_2 (35.0 wt.%) were put in a PTFE sealed vessel located in a High-Performance Microwave Digestion - MLS 1200 Mega (Milestone, Bergamo, Italy) oven. The digestion program followed was divided in 5 steps: 2 min at 250 W, 2 min at 0 W, 6 min at 250 W, 5 min at 400 W, and 5 min at 600 W. Once the obtained solutions were cooled at room temperature, it was added water up to 50 mL.

A concentration/emission calibration curve in the concentration range 1 – 100 ppm was carried out for each investigated element by dilution in nitric acid solution from certified 1000ppm standard solutions (Sigma Aldrich, St. Luis, MO, USA). The most abundant elements among those detected were quantified using the wavelength reported in the following table (Table 2.1).

Table 2.1 – List of the most element wavelength used to quantify the composition of samples by ICP-OES.

Element	Wavelength (nm)
Ca	422.673
Fe	238.204
Mg	285.213
Mn	257.610
P	213.618
Zn	202.548

2.3. Ultraviolet–visible spectrophotometry

Ultraviolet–visible (UV-Vis) spectrophotometry is the most widely used technique for quantitative analysis.[10] It is based on the selective absorption of radiation belonging to the visible range (380 - 700 nm) and near ultraviolet (200 - 380 nm) by chemical species contained in a material.[11] UV-Vis instrument measures the intensity of the transmitted light passed through the sample (I) and compares it to the intensity of the incident light (I0). The ratio I/I_0 is called Transmittance and is commonly expressed as a percentage (%T). The experimental law most used in order to explain the radiation absorption phenomena, trasform trasmittance into absorbance and determine absorbing species concentration is the Lambert-Beer law (Equation 2.1):

$$A = -log_{10}\left(I/_{I_0}\right) = log_{10}(1/_T) = \varepsilon bC \qquad \text{(Equation 2.1)}$$

This law states that the absorbance (A) of an absorber contained in a solution is directly proportional to its molar concentration (C indicated in mol L^{-1}), for a fixed optical path length (b) which corresponds to the length traveled from the radiation in the sample holder (cuvette), usually 1 cm. Moreover, A is also directly proportional with the molar extinction coefficient (ε expressed in cm L mol^{-1}) that is definite for each substance and varies depending on the wavelength of the absorbed radiation, the nature of the solvent, the pH and the chemical species it absorbs.[12,13]

UV–Vis spectrophotometers are generally composed by five main components: the light source, monochromator, sample holder, detector, and interpreter. In particular, the exciting radiation generated by tungsten lamp for the visible region and deuterium lamp

for the ultraviolet region, is sent to the monochromator which selects the individual wavelengths (monochromatic bands). The monochromatic radiations pass towards the sample which in part absorbs them, while the trasmitted part reaches the detector, generally a multiplier phototube. There are two classes of spectrophotometers: single and double beam. In single beam spectrophotometers configuration, the test sample is measured in sequence after the reference. In the double beam configuration, instead, light from the source after passing through the monochromator is split into two separate beams by the chopper. One beam is used for the reference, while the other one is used for sample determination (Figure 2.3).

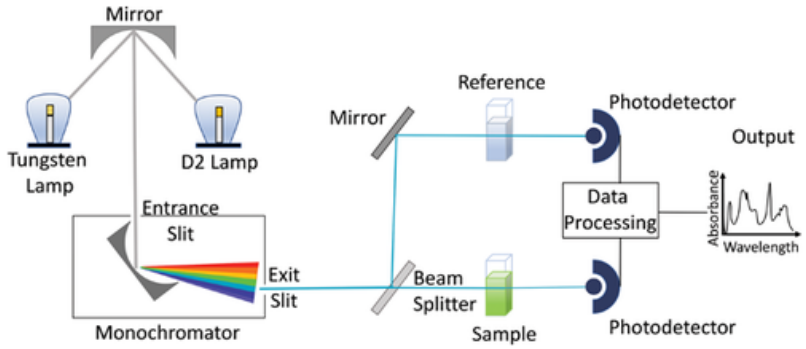

Figure 2.3 - UV-vis double beam spectrophotometer diagram.[14]

This latter configuration is advantageous because sample and reference reading can be conducted simultaneously so that measure becomes independent from variations in the intensity and spectral composition of the light source.[11]

During this Ph.D. thesis, samples were analysed in quartz cuvette using UV/VIS/NIR double beam Spectrometer Lambda 750 (PerkinElmer). Spectra were recorded at several different range of wavelenght depending on the kind of absorbant analysed, with a resolution of 1 nm. Beforehand, a complete absorption spectrum to evaluate the wavelenght in which the sample shows its maximum absorbance was carried out. Moreover to quantify test solutions, it was also performed a calibration for each absorbant by analysing various concentration of its solution at known and increasing concentration. The concentration range of the prepared solution depended on the molar extinction coefficient of the absorbant.

2.4. Scanning electron microscope

Scanning electron microscope (SEM) is one of the common techniques for the micro-morphology characterization of materials.[15–17] This electron microscope take advantage from a source of a focused electrons beam that hit and react with the sample so as to generate an image of the area intended to be observed. The Figure 2.4 shows a schematic diagram of SEM microscope, in which is possible to observe that the creation of the SEM image is the result of secondary electrons (SEs) and/or backscatter electrons (BSE) signals produced by the interaction of the focused electrons beam with the sample.[18–20]

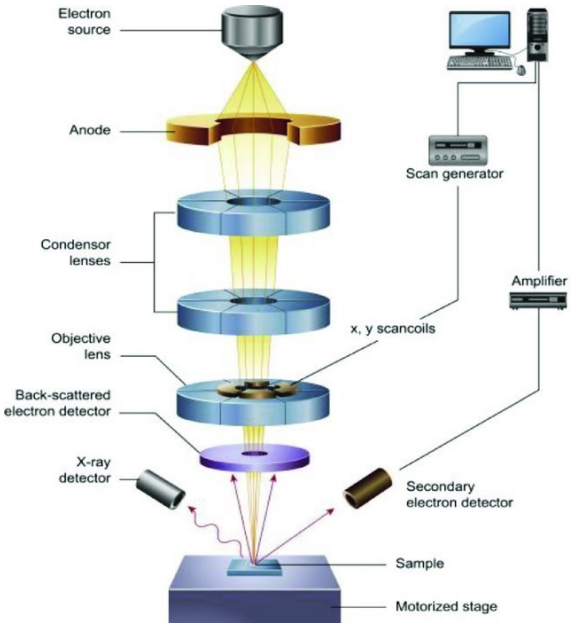

Figure 2.4 - Schematic diagram of a SEM microscope.[21]

Commonly, the source is a tungsten cathode (electron gun) that generates electrons, and then they are accelerated towards an anode. Subsequently by passing through condenser lenses and scanning coils contained in the electron optical column, the electron beam is focused and has few hundred eV up to 100 KeV of energy. Secondary electrons are detected by a scintillator photomultiplier device and the resulting signal is properly elaborated into a two-dimensional intensity distribution which can be showed and saved as a digital image.[19]

In this Ph.D. thesis, the sample morphology was achieved by a Field Emission Gun – Scanning Electron Microscopy (FEG–SEM, ΣIGMA, ZEISS NTS GmBH, Oberkochen, Germany). Samples were powdered and deposited on carbon tape mounted on an aluminium SEM stub and sputter coated (Polaron E5100, Polaron Equipment, Watford,

Hertfordshire, UK) with 10 nm of gold for electrical conductance. Accelerating voltages in the 3 to 10 keV range were used to observe the samples in the secondary electron imaging mode.

2.5. Transmission electron microscope

Transmission electron microscope (TEM) is another kind of electron microscopy that is used to characterize the materials both from the morphological point of view (grain size and analysis of defects), and from the crystallographic point of view (visualization and measurement of the reticular planes).[22,23] In Figure 2.5 is showed a schematic diagram of a TEM microscope in which are visible its four main parts: electron source, electromagnetic lens system, sample holder, and imaging system.

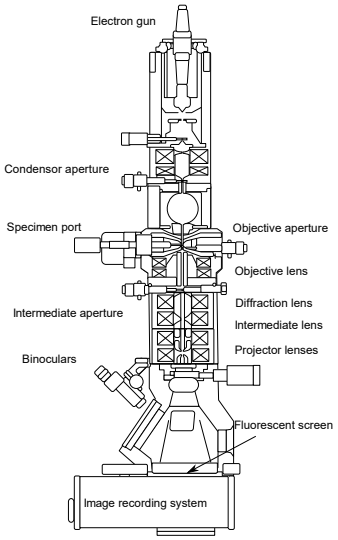

Figure 2.5 - Schematic diagram of a TEM microscope.

Electrons emitted by vacuum heating of a tungsten filament (source) through a thermoelectric effect are focused by using electromagnetic lenses in a very thin beam, and then it crosses the specimen. The electron beam transmitted is highly dependent on the properties of the examined material (e.g., density, composition, etc). It generates a projected “shadow image” of the sample onto a fluorescent screen in the imaging system, in which are showed its different parts in varied darkness according to their density. Finally, the images could be elaborated on a layer of photographic film or detected by a sensor such as a charge-coupled device (CCD) systems, which are a major technology used in digital imaging.[19,22,24]

The instrument used to evaluate the morphology of samples was a Tecnai F20 microscope (Fei Corp., Hillsboro, OR, USA) equipped with a Schottky emitter operating at 120 keV. Sample preparation has consisted of ultrasonically dispersion of dry powders sample in ultrapure water, and then few droplets of the suspension were deposited on a special grid made of copper (200 mesh) and covered with a thin layer of carbon. Once the deposited sample was incubated for several minutes, the excess of solvent was removed with filter paper and dried. Finally, the grids were rapidly transferred to the microscope to analyse the samples.

2.6. Dynamic light scattering

Dynamic light scattering (DLS) is an optical measurement technique used to determine the nanoparticles' size distribution through the quantification of the constant random motion of nanoparticles dispersed in a liquid (e.g., suspensions, emulsions, micelles, etc), called Brownian motion.[25,26] In particular, this constant random motion leads toward a distance variation between nanoparticles depending both on particles dimension and on the time and creates constructive and destructive interferences in the intensity of the scattered monochromatic He-Ne laser light. The collecting optics gather the scattered light at a specific angle and the produced light fluctuations are converted into electrical pulses by a photodiode detector or photomultiplier tube.[27,28] In Figure 2.6 is shown a schematic diagram of the just described DLS instrument.

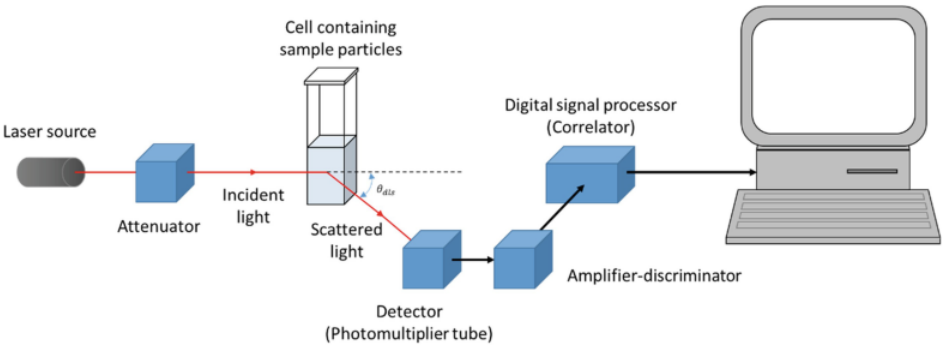

Figure 2.6 – Schematic diagram of a DLS instrument.[26]

The instrument uses algorithms by which is possible to estimate the distribution widths, called polydispersity index (PDI), and it is possible to calculate the hydrodynamic

diameter [d(H)] of a particle by using the Stokes–Einstein equation (Equation 2.2) and the translational diffusion coefficient (D), which defines the Brownian motion speed.

$$d(H) = {kT}/{3 * \pi * \eta * D} \qquad \text{(Equation 2.2)}$$

As it is possible to notice from the Equation 2.2, the hydrodynamic diameter which is the diameter of a perfect spherical particle that would be characterized by the same hydrodynamic friction as the molecule of interest, depends not only on the particles translational diffusion coefficient, but also on solvent viscosity (η), temperature (T) and Boltzmann's constant (k).[25–28]

In general, this analysis is easily affected by solvent viscosity, refractive index, sample temperature, and sample concentration. Moreover, before the analysis, air bubbles and dust particles must be removed by ultrasonication, centrifugation, or filtration.

In this Ph.D. thesis, DLS analyses were performed by using a Zetasizer Nano ZS (Malvern Ltd., UK). Samples were dispersed or diluted in water at pH 7.0 achieving a concentration of 0.5 mg mL^{-1}. The working parameters for samples and solvent are 1.63 as the hydroxyapatite refractive index, and 1.33 as the water refractive index, respectively. Size distribution measures were obtained analysing each sample by using low-volume quartz cuvettes (105.251-QS, Hellma, Germany). In particular, 10 runs of 30s for 4 times were performed for each sample. Results were reported as the Z-average of the hydrodynamic diameter distribution values obtained by the measure previous described.

2.6.1. Electrophoretic light scattering

The electrophoretic light scattering (ELS) is a technique based on DLS that is used to measure the electrostatic potential, called zeta potential (ZP), of a suspension. This parameter could provide information regarding the colloidal stability of a suspension. The evaluation of the zeta potential takes into account the electrical double layer which is the formation of a strongly bounded layer of ions with opposite charge respect the net charge of the particles dispersed in the liquid, and then the growth of a diffuse outer layer of loosely associated ions. The measure of the electrophoretic mobility of the nanoparticles is achieved by using an electrical field passing through the sample and observing the fractions of ions that are present in the diffuse layer and move with the nanoparticles,

and remaining part of ions that remain in the bulk dispersant.[29–31] Indeed, as it is possible to notice from the Figure 2.7, this measure is related to the surface charge of the nanoparticles.

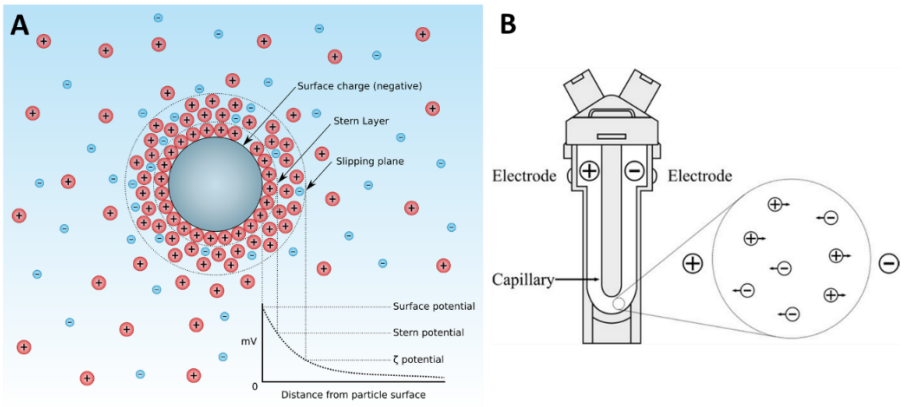

Figure 2.7 - Schematic representation of the electrical double layer (A) and the folded capillary cell used for the zeta potential evaluation (B).[32]

In general, as it is shown in the Table 2.2, the higher is the ZP value, the more colloidally stable is the suspension analyzed.

Table 2.2 - Relation between the ZP values and the stability of a suspension

Zeta potential (mV)	Stability of the sample
From 0 to ± 5	Rapid coagulation or flocculation
From ± 10 to ± 30	Incipient stability
From ± 30 to ± 40	Moderate stability
From ± 40 to ± 60	Good stability
More than ± 60	Excellent stability

A large negative or positive ZP highlights the tendency of the nanoparticles to repel each other and for this reason the probability to flocculate is almost zero. However, if the ZP is near to 0, nanoparticles are induced to aggregate and flocculate due to the lack of a repulsion force between them. Commonly the limit between the instability or the stability of a suspension is fixed at ZP values equal to +30mV or - 30mV.[2,29]

In this Ph.D. thesis, the evaluation of ZP was carried out as the electrophoretic mobility average at 25 °C using a laser Doppler velocimetry and a disposable electrophoretic cell

(DTS1061, Malvern Ltd., Worcestershire, UK) of three separate measurements (maximum 100 runs each).

2.7. High-performance liquid chromatography

High-performance liquid chromatography (HPLC) is an analytical technique commonly used to separate, identify, and quantify each component in a complex mixture. In particular, the separation of sample components, called analytes, takes place by their distribution between the solid stationary phase, which is constituted by sorbents packed inside a column, and a flowing liquid as the mobile phase. HPLC analyses can be performed isocratically, in which the solvent delivered to the column is not changing in composition, or by using a gradient elution. The latter one is commonly used for complex separations, and it is performed by altering the eluents proportion over the time course. This dynamic partitioning process of the analytes leads toward their movement at different velocities along the column and their eventual separation in the chromatogram (Figure 2.8). [33–35]

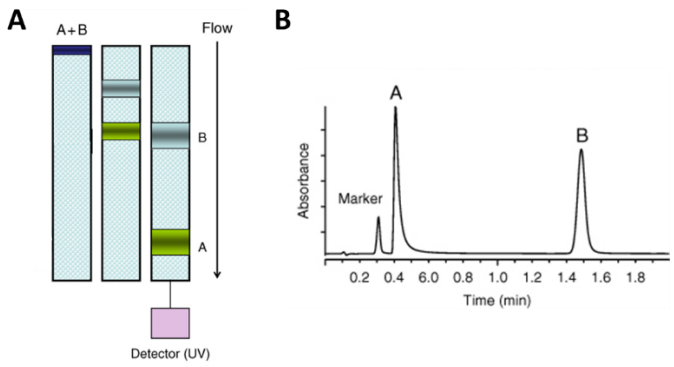

Figure 2.8 - A scheme of the chromatographic process, showing the separation between A and B components (A) and a representation of a chromatogram related to A and B components (B).

Commonly, HPLC instrumentation is composed by six basic components: solvent reservoir, pump, injector, column, detector, and output device (Figure 2.9). The solvent reservoir is composed by all the mobile phase appropriately filtered and degassed, the pump, commonly a reciprocating piston pump, aims to deliver a precise, accurate, reproducible, constant, and pulse-free flow of mobile phase to the column. The injector could be manual or automatic and it is used to introduce the sample into the instrument without depressurizing it. Furthermore, the column is the HPLC part in which the

separation occurs. An HPLC detector should be characterized by high sensitivity, good stability, linearity, short response time, reliability, non-destructiveness, ease of use, and low dead volume. The most used chromatography detectors are UV ones. Finally, after the data collection device which convert the electronic signal produced by the detector, the output device shows the chromatogram from which can be evaluated both qualitative and quantitative information about the analyte.[35]

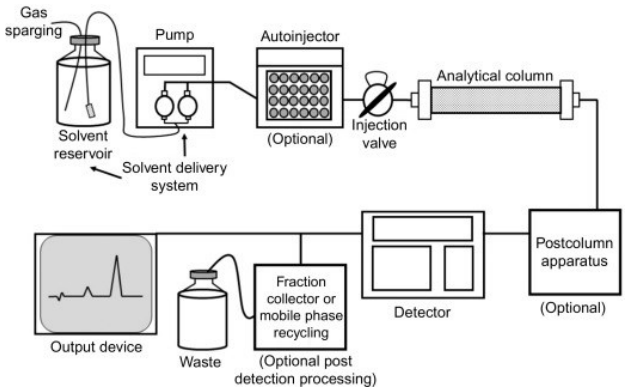

Figure 2.9 – Schematic diagram of a generic HPLC system.[35]

The equipment employed to perform HPLC analyses in this work is a 1260 Infinity II (Agilent Technologies, Varian, Palo Alto, Santa Clara, CA USA) apparatus. The evaluation of each molecule was carried out by using a reversed-phase chromatography (RPC) which is characterized by polar mobile phase and a hydrophobic (nonpolar) stationary phase, made of solid particles coated with covalently bonded hydrophobic groups. Each specific method for the determination and quantification of the analyte which will be described in its corresponding section.

2.8. Thermogravimetric analysis

Thermogravimetry is a technique used to investigate and quantify weight changes of a substance as a function of time (isothermal mode) or temperature.[36–38] The thermogravimetric analysis (TGA) is commonly utilized to better understand several transformations (e.g., absorption, adsorption, desorption, vaporization, sublimation, decomposition, oxidation, and reduction) that happened when the sample is placed in a small electrically heated oven with a thermocouple to accurately measure the temperature.[36–38] Moreover, to prevent oxidation-reduction reaction or other undesired transformation of samples, different gas can be used (e.g., as air, argon, and nitrogen).

The weight loss profile in relation to the temperature is recorded by a microbalance while the sample is subjected to a heating or cooling environment, and it is called thermograms. From thermograms is possible to collect three main information about samples, like: i) its thermal stability, ii) its decomposition temperature, and iii) its composition. Indeed, it is possible to identify an unknown compound present into the sample or evaluate the amount of a specific compound contained in a complex matrix.[36] In Figure 2.10 is reported an example of a thermograms in which is highlighted the initial temperature of degradation (Ti) and the final temperature of degradation (Tf) of the sample.

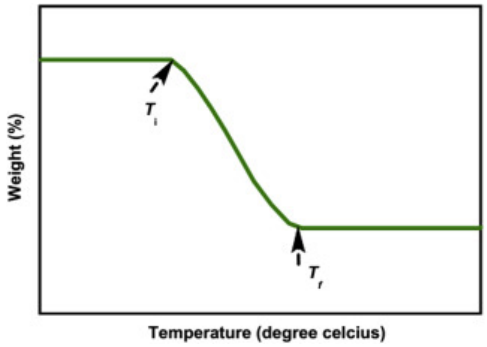

Figure 2.10 – An example of a thermogram in which is shown the initial (Ti) and final temperature (Tf) of a degradation.[36]

The equipment employed to carry out TGA analyses in this work is a STA 449F3 Jupiter (Netzsch GmbH, Selb, Germany) apparatus. Almost 10 mg of each sample was put in an alumina crucible and then heated from room temperature to 1100 ◦C under air flow with a heating rate of 10 ◦C/min.

2.9. X-ray Diffraction

The powder X-ray Diffraction (PXRD) is a non-destructive analytical technique, and it is commonly used for phase identification of crystalline or amorphous materials previously grounded and homogenized. In particular, an X-ray beam is generated by a cathode ray tube, and it is composed by high-energy electromagnetic waves with a wavelength between 10^{-3} and 10^{1} nm, comparable with inter-atomic distances.[39–41] When an X-ray wavelength hits the atoms contained in a sample, the electrons around them start to wobble with the same frequency as the incoming beam. Consequently, the electrons diffuse the incidence radiation in all the directions (Rayleigh scattering) and these generated radiations could interfere destructively or constructively with each other

(Figure 2.11A). A constructive interference occurs when atoms are arranged in a regular pattern (crystalline cell), as described in the Bragg's law showed in the Figure 2.11B.

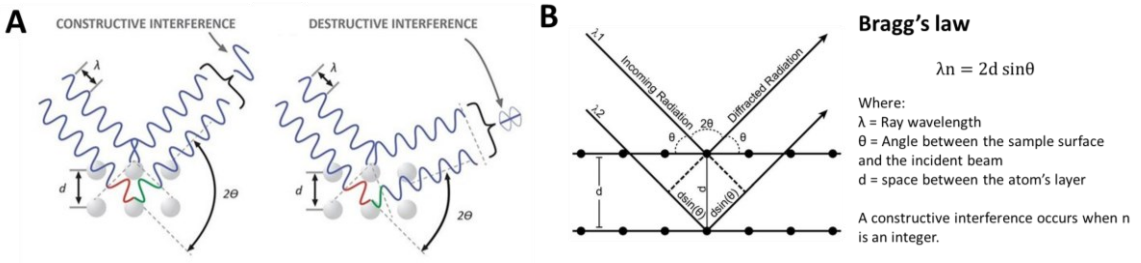

Figure 2.11 - Schematic representation of a constructive or destructive interference (A) and exploitation of the Bragg's law (B).[41,42]

The diffraction analysis consists of a series of peaks which are recognizable as the diffracted intensity of the sample related to the diffraction angle (2θ). A typical series of peaks described by Miller indexes (hkl) with specific positions and relative intensity of the lines, called pattern or diffractogram, is characteristic for each phase or material. In contrast to a crystalline material, amorphous ones generate a broad background signal.[40] The model of diffractometer employed during this thesis was a DS Advance Diffractometer (Bruker, Karlsruhe, Germany) with a Bragg-Brentano geometry (Figure 2.12) in which X-ray source and the detector move on a circle where sample in the centre.

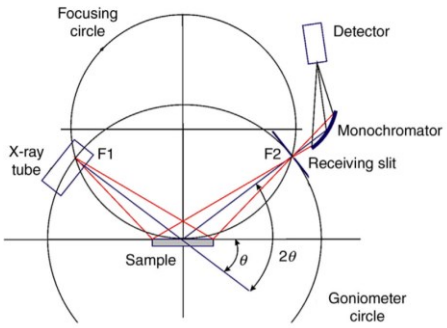

Figure 2.12 - Bragg–Brentano geometry used in most of the powder diffractometers.[39]

The instrument was equipped with a Lynx-eye position-sensitive detector, with CuKα radiation (λ = 1.54178 Å), at 40 kV and 40 mA. XRD patterns were acquired from 10 to 60 degrees (2θ) using a step size of 0.02◦ and a scanning speed of 0.5s. Phase identification was obtained through Rietveld refinement with the software TOPAS5. The weight composition of the phases was refined considering a multiphase system, using tabulated atomic coordinates of hydroxyapatite (ASTM Card file No. 09-0432), and β-TCP (ASTM

Card file No. 09-0169). Finally, the crystallinity degree of the samples was calculated according to Equation 2.3:

$$Cristallinity(\%) = 100 * \frac{C}{A+C} \quad \text{Equation 2.3}$$

where C was the sum of peaks area and A was the area between the peaks and the background in the diffraction pattern. The size of HA crystallites along the c-axis and along the perpendicular to it was calculated by applying Scherrer's formula (Equation 2.4) from the diffraction peaks located at 2θ values of 25.8° and 39.7° corresponding to the (002) and (310) reflections, respectively.

$$\beta = \frac{K\lambda}{D\cos\theta} \quad \text{Equation 2.4}$$

where β is the full width at half-maximum (FWHM) of the diffraction peak, K is a dimensionless shape constant, which has a typical value of about 0.9, varying with the actual shape of the crystallite. D is the crystallite size and θ is the Bragg angle.

2.10. Specific surface area

The specific surface area (SSA) is an intrinsic property of solids, and it is defined as a ratio between the total surface area of a material and the unit of its mass (m^2/g).[43] The SSA can be measured by several methods, but the most commonly used is based on the physical or chemical adsorption of an inert gas (usually nitrogen, N_2) on the sample surface.[44] The procedure also could provide a sample treatment phase under vacuum and subsequently at a temperature of 120 ° C which allows the elimination of residual moisture, in order to make the analysis as accurate as possible. The value of the SSA is calculated by determining the number of gas molecules which form a monolayer adsorption in order to consider all the gas molecules in contact with the surface of the material, on the basis of the theory of Brunauer, Emmet and Teller (BET) and the relative equation (Equation 2.5):[43–46]

$$\frac{1}{W\left(\left(\frac{P_0}{P}\right)-1\right)} = \frac{1}{W_m C} + \frac{C-1}{W_m C}\left(\frac{P}{P_0}\right) \quad \text{(Equation 2.5)}$$

In which W represent the weight of gas adsorbed, while Wm the weight of adsorbate as a monolayer. Moreover, the ratio between P and P0 is correlated to the relative pressure and, finally, the C parameter is the BET constant.

In this thesis the SSA of the powdered samples was measured through N_2 gas adsorption by the BET method using a Surfer instrument (Thermo Fisher Scientific Inc., Waltham, MA, USA).

References:

1. Degli Esposti, L. Tailoring calcium phosphate nanoparticles for medical applications: a fuctional by design approach. (University of Parma, 2019).
2. Campodoni, E. Design and development of bio-hybrid multifunctional materials for regenerative medicine. (University of Parma, 2018).
3. Lilaj, A. Characterization and SPF booster effect of natural calcium phosphate derived from fish industry bio-wastes. (University of Bologna, 2020).
4. Magnani, G. Photo-protective performances and life cycle assessment of a novel SPF booster developed from the circular economy of food by-products: towards more sustainable sunscreen. (2021).
5. Subramanian, A. & Rodriguez-Saona, L. Fourier Transform Infrared (FTIR) Spectroscopy. in *Infrared Spectroscopy for Food Quality Analysis and Control* 145–178 (Elsevier, 2009). doi:10.1016/B978-0-12-374136-3.00007-9.
6. Larkin, P. Instrumentation and Sampling Methods. in *Infrared and Raman Spectroscopy* 27–54 (Elsevier, 2011). doi:10.1016/B978-0-12-386984-5.10003-5.
7. Burgener, J. A. & Makonnen, Y. Nebulization systems. in *Sample Introduction Systems in ICPMS and ICPOES* 57–142 (Elsevier, 2020). doi:10.1016/B978-0-444-59482-2.00002-6.
8. Makonnen, Y. & Beauchemin, D. The inductively coupled plasma as a source for optical emission spectrometry and mass spectrometry. in *Sample Introduction Systems in ICPMS and ICPOES* 1–55 (Elsevier, 2020). doi:10.1016/B978-0-444-59482-2.00001-4.
9. Caruso, F., Mantellato, S., Palacios, M. & Flatt, R. J. ICP-OES method for the characterization of cement pore solutions and their modification by polycarboxylate-based superplasticizers. *Cem. Concr. Res.* **91**, 52–60 (2017).
10. Kafle, B. P. Application of UV–VIS spectrophotometry for chemical analysis. in *Chemical Analysis and Material Characterization by Spectrophotometry* 79–145 (Elsevier, 2020). doi:10.1016/B978-0-12-814866-2.00005-1.
11. Worsfold, P. J. Spectrophotometry | Overview. in *Encyclopedia of Analytical Science* 318–321 (Elsevier, 2005). doi:10.1016/B0-12-369397-7/00714-7.
12. Shard, A. G., Schofield, R. C. & Minelli, C. Ultraviolet–visible spectrophotometry. in

Characterization of Nanoparticles 185–196 (Elsevier, 2020). doi:10.1016/B978-0-12-814182-3.00012-2.

13. Crowley, T. E. Absorption of ultraviolet, visible, and infrared radiation. in *Purification and Characterization of Secondary Metabolites* 33–48 (Elsevier, 2020). doi:10.1016/B978-0-12-813942-4.00004-8.
14. Rocha, F. S., Gomes, A. J., Lunardi, C. N., Kaliaguine, S. & Patience, G. S. Experimental methods in chemical engineering: Ultraviolet visible spectroscopy-UV-Vis. *Can. J. Chem. Eng.* **96**, 2512–2517 (2018).
15. de Assumpção Pereira-da-Silva, M. & Ferri, F. A. Scanning Electron Microscopy. in *Nanocharacterization Techniques* 1–35 (Elsevier, 2017). doi:10.1016/B978-0-323-49778-7.00001-1.
16. Vladár, A. E. & Hodoroaba, V.-D. Characterization of nanoparticles by scanning electron microscopy. in *Characterization of Nanoparticles* 7–27 (Elsevier, 2020). doi:10.1016/B978-0-12-814182-3.00002-X.
17. Han, W., Jiao, H. & Fox, D. Scanning Electron Microscopy. in 35–68 (2018). doi:10.1007/978-981-13-0454-5_2.
18. Omidi, M. *et al.* Characterization of biomaterials. in *Biomaterials for Oral and Dental Tissue Engineering* 97–115 (Elsevier, 2017). doi:10.1016/B978-0-08-100961-1.00007-4.
19. Inkson, B. J. Scanning electron microscopy (SEM) and transmission electron microscopy (TEM) for materials characterization. in *Materials Characterization Using Nondestructive Evaluation (NDE) Methods* 17–43 (Elsevier, 2016). doi:10.1016/B978-0-08-100040-3.00002-X.
20. Abd Mutalib, M., Rahman, M. A., Othman, M. H. D., Ismail, A. F. & Jaafar, J. Scanning Electron Microscopy (SEM) and Energy-Dispersive X-Ray (EDX) Spectroscopy. in *Membrane Characterization* 161–179 (Elsevier, 2017). doi:10.1016/B978-0-444-63776-5.00009-7.
21. Salman Ali, A. Application of Nanomaterials in Environmental Improvement. in *Nanotechnology and the Environment* (IntechOpen, 2020). doi:10.5772/intechopen.91438.
22. Tang, C. Y. & Yang, Z. Transmission Electron Microscopy (TEM). in *Membrane*

Characterization 145–159 (Elsevier, 2017). doi:10.1016/B978-0-444-63776-5.00008-5.

23. Wang, K., Cao, B., Chen, J. & Zhou, W. TEM studies of nanostructures. in *Modeling, Characterization, and Production of Nanomaterials* 115–144 (Elsevier, 2015). doi:10.1016/B978-1-78242-228-0.00004-1.
24. Braidy, N., Béchu, A., Souza Terra, J. C. & Patience, G. S. Experimental methods in chemical engineering: Transmission electron microscopy—TEM. *Can. J. Chem. Eng.* **98**, 628–641 (2020).
25. Kato, H. Size Determination of Nanoparticles by Dynamic Light Scattering. in *Nanomaterials* 535–554 (Wiley-VCH Verlag GmbH & Co. KGaA, 2012). doi:10.1002/9783527646821.ch8.
26. Leong, S. S., Ng, W. M., Lim, J. & Yeap, S. P. Dynamic Light Scattering: Effective Sizing Technique for Characterization of Magnetic Nanoparticles. in *Handbook of Materials Characterization* 77–111 (Springer International Publishing, 2018). doi:10.1007/978-3-319-92955-2_3.
27. Babick, F. Dynamic light scattering (DLS). in *Characterization of Nanoparticles* 137–172 (Elsevier, 2020). doi:10.1016/B978-0-12-814182-3.00010-9.
28. Ramos, A. P. Dynamic Light Scattering Applied to Nanoparticle Characterization. in *Nanocharacterization Techniques* 99–110 (Elsevier, 2017). doi:10.1016/B978-0-323-49778-7.00004-7.
29. Pippa, N., Pippa, N., Pispas, S. & Demetzos, C. Physico-chemical Characterization and Basic Research Principles of Advanced Drug Delivery Nanosystems. in *Intelligent Nanomaterials* 107–125 (John Wiley & Sons, Inc., 2017). doi:10.1002/9781119242628.ch5.
30. Moore, J. & Cerasoli, E. Particle Light Scattering Methods and Applications. in *Encyclopedia of Spectroscopy and Spectrometry* 543–553 (Elsevier, 2017). doi:10.1016/B978-0-12-803224-4.00040-6.
31. Nguyen, M.-H., Aripin, N. F. K., Chen, X. G. & Park, H.-J. Methodologies Used for the Characterization of Nano- and Microcapsules. in *Nano- and Microencapsulation for Foods* 65–94 (John Wiley & Sons, Ltd, 2014). doi:10.1002/9781118292327.ch4.

32. Garcia, A. L. Nano-silica production at low temperatures from the dissolution of olivine: synthesis, tailoring and modelling. *Tech. Univ. Eindhoven* (2014) doi:10.6100/IR774494.

33. Dong, M. *HPLC and UHPLC for Practicing Scientists*. (Wiley, 2019). doi:10.1002/9781119313786.

34. Jandera, P. Comparison of various modes and phase systems for analytical HPLC. in 1–91 (2020). doi:10.1016/B978-0-444-64070-3.00001-1.

35. LaCourse, M. E. & LaCourse, W. R. General instrumentation in HPLC *. in *Liquid Chromatography* 417–429 (Elsevier, 2017). doi:10.1016/B978-0-12-805393-5.00017-8.

36. Loganathan, S., Valapa, R. B., Mishra, R. K., Pugazhenthi, G. & Thomas, S. Thermogravimetric Analysis for Characterization of Nanomaterials. in *Thermal and Rheological Measurement Techniques for Nanomaterials Characterization* 67–108 (Elsevier, 2017). doi:10.1016/B978-0-323-46139-9.00004-9.

37. Bottom, R. Thermogravimetric Analysis. in *Principles and Applications of Thermal Analysis* 87–118 (Blackwell Publishing Ltd). doi:10.1002/9780470697702.ch3.

38. Prime, R. B., Bair, H. E., Vyazovkin, S., Gallagher, P. K. & Riga, A. Thermogravimetric Analysis (TGA). in *Thermal Analysis of Polymers* 241–317 (John Wiley & Sons, Inc.). doi:10.1002/9780470423837.ch3.

39. Lamas, D. G., de Oliveira Neto, M., Kellermann, G. & Craievich, A. F. X-Ray Diffraction and Scattering by Nanomaterials. in *Nanocharacterization Techniques* 111–182 (Elsevier, 2017). doi:10.1016/B978-0-323-49778-7.00005-9.

40. Epp, J. X-ray diffraction (XRD) techniques for materials characterization. in *Materials Characterization Using Nondestructive Evaluation (NDE) Methods* 81–124 (Elsevier, 2016). doi:10.1016/B978-0-08-100040-3.00004-3.

41. Boratto, M. H. Semiconducting and Insulating oxides applied to electronic devices. (Universidade Estadual Paulista “Júlio de Mesquita Filho” - UNESP, 2018).

42. Stan, C., Beavers, C., Kunz, M. & Tamura, N. X-Ray Diffraction under Extreme Conditions at the Advanced Light Source. *Quantum Beam Sci.* **2**, 4 (2018).

43. Gibson, N., Kuchenbecker, P., Rasmussen, K., Hodoroaba, V.-D. & Rauscher, H. Volume-specific surface area by gas adsorption analysis with the BET method. in

Characterization of Nanoparticles 265–294 (Elsevier, 2020). doi:10.1016/B978-0-12-814182-3.00017-1.

44. Ambroz, F., Macdonald, T. J., Martis, V. & Parkin, I. P. Evaluation of the BET Theory for the Characterization of Meso and Microporous MOFs. *Small Methods* **2**, 1800173 (2018).

45. McMillan, W. G. & Teller, E. The Assumptions of the B.E.T. Theory. *J. Phys. Chem.* **55**, 17–20 (1951).

46. Dollimore, D., Spooner, P. & Turner, A. The bet method of analysis of gas adsorption data and its relevance to the calculation of surface areas. *Surf. Technol.* **4**, 121–160 (1976).

3. CaP NPs for drug delivery application

3.1. Introduction

The biomedical material that will be treated in this chapter consists in a CaP NPs loaded with an antimicrobial drug, developed as an inhalable drug delivery formulation for the treatment of cystic fibrosis. Cystic fibrosis (CF) is a genetic disease which, according to the US Cystic Fibrosis Foundation, is affecting today nearly 70,000 patients worldwide and probably 1000 new cases are added every year.[1–4] CF is caused by mutations in the chromosome 7 gene, that encodes the cystic fibrosis transmembrane conductance regulator (CFTR) protein. The CFTR protein is responsible for the regulation of chloride ions secretion and sodium ions reabsorption[5] and its mutation results in impaired chloride ions secretion and hyper-absorption of sodium ions across epithelia,[6] causing a hypersecretion of thick mucus difficult to clear. The over-production of the mucus secreted in the lungs, along with its altered composition and consistency, results in airway obstruction that makes the lungs susceptible to recurrent and persistent bacterial infections and endobronchial chronic inflammation, which are considered the primary cause of bronchiectasis, respiratory failure, and consequent death of patients.[7]

Among all the pathogens that affect the airways of CF patients, *Pseudomonas aeruginosa* (PA) is the most prevalent.[8] PA belongs to the family of Gram-negative organisms[9] and its eradication has become increasingly difficult due to its remarkable capacity to resist to a variety of antibiotics, including aminoglycosides, quinolones and β-lactams.[10] This resistance is a well-documented phenomenon due to several molecular mechanisms such as the restricted outer membrane permeability, the presence of integron, the presence of insertion sequences elements, and the biosynthesis of degrading-enzymes.[11] PA infections usually start as an acute infection that finally becomes chronic. One of the main pathogenicity factors that favours PA colonization and resistance is its ability to develop a biofilm-like mucus layer in the viscous hypoxic media of CF patients' respiratory tract.[12] An antibacterial drug that has been proposed to treat PA is Colistin (Col – Figure 3.1), a cyclic polypeptide antibiotic active against Gram-negative pathogens.[13]

Part of the content of this chapter will be published as "M. Iafisco, F. Carella, et al. Biocompatible antimicrobial colistin loaded calcium phosphate nanoparticles for the counteraction of biofilm formation in cystic fibrosis related infections" and it was published as "C. Velino, F. Carella, et al. Nanomedicine Approaches for the Pulmonary Treatment of Cystic Fibrosis"

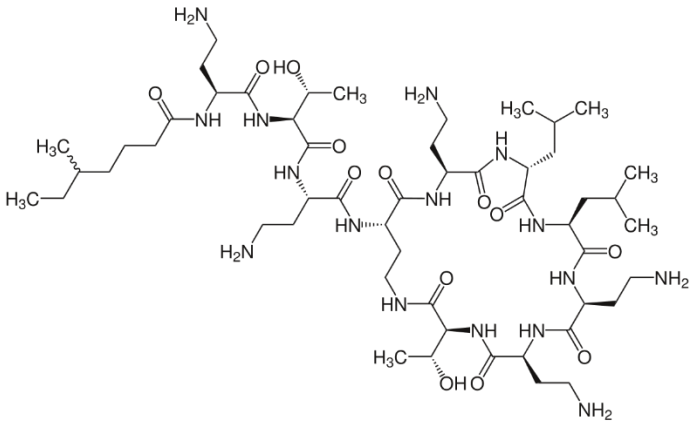

Figure 3.1 – Colistin structure[14]

The bactericidal action of Col is given by its cationic nature which interact with the anionic lipopolysaccharides in the outer membrane of the pathogen, causing an instability within the cell membrane and a subsequent change in permeability which causes bacterial death.[15] Historically, Col was administered intravenously, but reports of nephrotoxicity and neurotoxicity discouraged its use, especially after the appearance of other less toxic antimicrobials, such as tobramycin.[16] The resurgence of Col in recent times has been led by the lack of effective treatment options against multi-drug resistant pathogens and by the development of more efficient and safer Col that can be administered by inhalation as nebulizer or in dry state.[16,17] The drug administration via inhalation routes (oral and nasal) constitutes an effective alternative to treat pulmonary disease. Indeed, it is characterized by several advantages, including rapid onset of action, non-invasive nature, high permeability of the lungs,[18] rapid absorption,[19] and improved patient compliance.

Nowadays, nebulization of antimicrobial drugs such as Col, tobramycin, aztreonam lysine and, more recently, levofloxacin is a cornerstone in the treatment of pulmonary PA infections in CF patients, either in preventing or stabilizing chronic infections, sometimes combined with intravenous therapy.[20,21] Although this therapy has tremendous improved the quality of life of affected patients, several concerns remain regarding the presence of side effects associated to their use in high concentration. Inhaled antibiotics present poor capability of penetrating the sticky mucus to target the enclosed bacteria and to reach peripheral airways by overcoming mucosal plugs at the central bronchi and bronchioles.[20] Thus, under these conditions, inhaled antibiotics may not reach the regions with the highest bacterial loads and therefore show limited efficacy. The poor lung bioavailability of Col is attested by the therapeutic need of high doses up to 160 mg twice a day delivered

by nebulization of a Col solution or up to 125 mg twice a day administered by Col dry inhalation powder formulation.[22] In addition, despite Col is considered one of the most active antimicrobials to combat multidrug-resistance bacteria, recent studies have described the emergence of Col-resistant bacteria in CF patients treated with long-term by inhalation.[23,24]

These facts have stimulated the research on the introduction of new formulations that can improve efficiency and diminish doses of antimicrobial drugs. In that sense, nanotechnology has emerged as an interesting approach for antibiotic delivery to the lungs as they can protect the drug from chemical and enzymatic degradation and gradually release it in the target site, thus minimizing the toxicity and improving the antimicrobial effect.[25,26] In addition, in the case of CF patients, the use of NPs could be a valid approach to overcome the thick mucus layer that is formed within the alveolar region as well as the bacterial biofilm.[1,27,28] Indeed, NPs are able to diffuse through the network of the mucus while larger ones are trapped in the meshes by physical size exclusion effect. To the best of our knowledge solid lipid NPs,[29] nanostructured lipid carriers,[29–31] gold and silver NPs,[32,33] human albumin NPs,[34] polydopamine nanospheres[35] and poly(lactide-co-glycolide) nano-embedded microparticles[36] have been loaded so far with Col and tested *in vitro* and *in vivo* in mice.

An innovative NPs that could be interesting to study for the treatment of this disease are CaP NPs, which represent one of the most promising material in nanomedicine.[37] Indeed, as previously mentioned, CaPs are recognized as endogenous material by immune system, since they exhibit high similarity in terms of physical and chemical properties with the mineral phase of bone and tooth. Among all the properties that characterize CaP NPs, it is worth to mention its pH-sensitive stability that provides rapid dissolution in slightly acidic environments (e.g. pulmonary mucosa), and good stability at physiological pH.[38,39] For this reason, it is possible to state that CaP NPs are promising drug delivery systems. Indeed, their intrinsic stability which can protect loaded bioactive molecules from the possible degradation in biological environment, combines with their acidic pH-triggered dissolution which allow the drug release in the target area.[37] On the other hand, CaP NPs are usually characterized by lower drug payload values respect to other NPs (hollow organic NPs or liposomes), and by higher tendency to form aggregates in aqueous suspensions.[37] However, in literature there are several works that have demonstrated a

CaP NPs stabilization method by using a surface decoration with ionic organic molecules (e.g. citrate ions, amino acids or macromolecules).[40–44]

The aim of the work reported in this first chapter of the thesis consists in the design, preparation, and evaluation *in vitro* of a new therapeutic formulation based on inhalable and biodegradable CaP NPs functionalized with Col. Once achieved the optimized Col functionalization, the final material was physical, and chemical characterized. Moreover, in vitro experiments were also conducted to evaluate its biocompatibility, antimicrobial and antibiofilm efficacy.

3.1.1. Materials

Calcium chloride dihydrate ($CaCl_2 \cdot 2H_2O$, BioXtra, ≥ 99.0% pure), sodium citrate tribasic dihydrate ($Na_3(C_6H_5O_7) \cdot 2H_2O$, ACS reagent, ≥ 99.0% pure, referred as Na_3(Cit)), sodium phosphate dibasic (Na_2HPO_4, ACS reagent, ≥ 99.0% pure), sodium carbonate monohydrate ($Na_2CO_3 \cdot H_2O$, ACS reagent, 99.5% pure), hydrochloric acid (HCl, ACS reagent, ≥ 99.0% pure), acetonitrile (ACN, Sigma Aldrich, ≥ 99.9% pure for HPLC), sodium sulfate (Na_2SO_4, ACS reagent, ≥ 99.0% pure), trifluoroacetic acid (TFA, Sigma Aldrich, ≥ 99.0% pure for HPLC) were supplied by Sigma-Aldrich (St. Luis, MO, USA). Colistin sulfate (purity ≥ 95.0%, referred as Col) was purchased from Vinci Biochem (Vinci (FI), Italy). Alexa Fluor 647-risendronate fluorescence dye (AF647-RIS) was purchased from BioVinc LLC (Pasadena, CA, USA). All the solutions were prepared with ultrapure water (18.2 MΩ × cm, 25°C, Arium© pro, Sartorius, Gottingen, Germany).

3.1.2. Preparation and characterization of NPs

Preparation of CaP NPs

CaP NPs were prepared following a wet precipitation reported by Delgado-Lopez et al.[40] In particular, two solutions: (i) 0.1 M $CaCl_2$ + 0.4 M Na_3(Cit) and (ii) 0.12 M Na_2HPO_4 + 0.1 M Na_2CO_3 were mixed at 25°C. Previously, the pH of the (ii) solution was adjusted to 9.0-9.5 with HCl. The mixture was then introduced in a round-bottom flask, sealed with a stopper, and immersed in a silicone oil bath at 80°C for 24 h under magnetic stirring. Once the precipitation occurs, the particles were repeatedly washed with ultrapure water by centrifugation (7000 RPM, 5 minutes), and the resultant pellet was resuspended in

ultrapure water and stored at 4°C. CaP NP concentration of the final suspension was estimated by weighing the solid residue after freeze-drying 1 mL of suspension at -50 °C under a vacuum of 3 mbar. Afterward, CaP NPs suspension were diluted obtaining a concentration of 8 mg mL^{-1}. Before use, CaP-NPs suspension was dispersed by sonication for 2 min in a sonic bath.

Preparation of fluorescent CaP NPs with AF674-RIS dye

Fluorescent CaP NPs were prepared by tagging them with AF647-RIS fluorescence dye. CaP NPs suspension was diluted with water up to a concentration of 1 mg mL^{-1}, and a 24 nmol mL^{-1} solution of AF647-RIS was added to the suspension with a ratio of 2 nmol per mg of CaP NPs. Subsequently, the suspension was incubated in the dark under horizontal shaking at 37°C for 2 h. An aliquot of the so obtained suspension was centrifuged (10000 RPM, 5 minutes), and the UV-Vis spectrometry analysis of the supernatant (λ_{max}: 648 nm, ε: 240000 M^{-1} cm^{-1}) revealed that >99% of AF647-RIS was bound to CaP-NPs. Thus, after incubation the prepared AF647-CaP-NPs were used without further purification.

NP characterization

Freeze-dried CaP NPs were characterized by PXRD, TEM, FT-IR, and SEM. In this chapter, the samples preparation for SEM analysis was performed diluting the suspension in ultrapure water obtaining a concentration of 0.1 mg mL^{-1}. Subsequently, the achieved suspension was ultrasonically dispersed with a bath sonicator for 10 min. Then, a drop of CaP-NP suspension was deposited on a flat mirror polished silicon wafer mounted on an aluminum stub and left to dry at room temperature. Once the samples were dried, they were sputter coated with 2 nm of Pt/Pd (80:20) alloy to provide electrical conductance. Moreover, to determine their hydrodynamic diameter distribution and ζ-potential, the suspension samples were analysed by DLS at a concentration of 1 mg mL^{-1} and at pH 7.

Study of Col adsorption on CaP NPs

The adsorption study was mainly organized in two steps. Firstly, a kinetic adsorption was conducted to determine the amount of time needed to reach the thermodynamic adsorption equilibrium. Then, setting the time obtained from the kinetic adsorption, the adsorption isotherms was performed to determine the drug amount needed to reach the thermodynamic adsorption equilibrium. Finally, kinetic adsorption curves were fitted using the common models of pseudo first/second-order kinetics. The isothermal

adsorption curves, instead, were fitted using Langmuir, Freundlich and Langmuir-Freundlich common models.

In particular, the kinetic adsorption of Col on CaP NPs was carried out by mixing 2.5 mL of a 2 mg mL^{-1} Col solution in KCl 0.01M aqueous solution and 2.5 mL of 8 mg mL^{-1} CaP-NP suspension. Samples were maintained in a bascule bath at 37°C. At scheduled times ranging from 15 min to 24 h, CaP NPs were separated from the supernatant by centrifugation (10000 rpm, 5min). To determine the amount of Col loaded on CaP NPs, the supernatant was measured by HPLC.

The curves were fitted to the experimental data using a nonlinear least-squares fitting algorithm to obtain the model parameters. These models are defined as "pseudo" first-/second- order because first/second order kinetics were developed to describe the reaction of dissolved solutes in a liquid phase. These models, instead, are focus on adsorbed species bound to a solid phase. In particular, the pseudo first-order model assumes that the adsorption is reversible, and that the rate of drug adsorption on the substrate with time is directly proportional to the difference between the amount of drug adsorbed at equilibrium and the amount of drug already adsorbed.[45] The mathematical expression for the pseudo first-order model is reported in Equation 3.1:

$$Q(t) = Q_{ads,e} * \left[1 - e^{(-k_1 * t)}\right] \qquad \text{(Equation 3.1)}$$

where Q(t) and $Q_{ads,e}$ are the amount of molecule adsorbed per unit weight of the sorbent (mg g^{-1}) at time t and at equilibrium, respectively. The parameter k_1 is the pseudo first-order adsorption rate coefficient (t^{-1}).

On the other hand, the pseudo second-order kinetic model assumption is that the rate-limiting step is chemisorption. The adsorption rate depends on the availability of adsorption sites on the substrate and not on concentration of adsorbate, and that the interaction is not reversible.[46] For the pseudo second-order model, the mathematical expression is reported in Equation 3.2:

$$Q(t) = Q_{ads,e} * \left[1 - \left({}^{1}/_{1 + k_2 t}\right)\right] \qquad \text{(Equation 3.2)}$$

where in this case k_2 is the pseudo second-order adsorption rate coefficient (t^{-1}).

Lastly, the isothermal adsorption of Col on CaP-NPs was carried out putting in contact CaP NPs and Col solution in the same ratio used for the kinetic study. The initial Col

concentration was varied ranging from 0.1 to 2.0 mg mL^{-1} and the contact time was set at 150 min. CaP-NPs were separated from the supernatant by centrifugation and the amount of Col adsorbed was determined by HPLC as reported above.

The curves were fitted to the experimental data using a nonlinear least-squares fitting algorithm to obtain the model parameters. The Langmuir adsorption model considers that (i) solid particles have a limited adsorption capacity, (ii) all the adsorption sites are identical, (iii) each site retains one molecule of the given compound, and (iv) all sites are energetically and sterically independent from the adsorbed quantity.[45] The mathematical expression for the Langmuir model is reported in Equation 3.3:

$$Q = Q_m * \left({}^{(K_L * C_e)} \Big/ _{(1 + K_L * C_e)} \right) \qquad \text{(Equation 3.3)}$$

where Q is the quantity of molecules adsorbed per unit weight of the sorbent (mg g^{-1}), C_e is the equilibrium concentration of adsorbate in solution (mg mL^{-1}), Q_m is the maximum loading capacity (mg g^{-1}), and K_L is the Langmuir affinity constant (mL mg^{-1}).

The Freundlich model describes non-ideal and reversible adsorption, and it is not restricted to the formation of the monolayer.[46] This empirical model can be applied to multilayer adsorption, with a non-uniform distribution of adsorption sites and affinities over a heterogeneous surface. The mathematical expression of the Freundlich model is reported in Equation 3.4:

$$Q = K_F * C_e * e^{\left(\frac{1}{n}\right)} \qquad \text{(Equation 3.4)}$$

where K_F is the Freundlich affinity constant (mL mg^{-1}), C_e is the same as above, and n is the heterogeneity parameter.

The Langmuir-Freundlich model is a combination of the above two models, and it is used for predicting heterogeneous adsorption systems. The mathematical expression of this model is reported in Equation 3.5:

$$Q = Q_m * {}^{(K_{LF} * C_e)^n} \Big/ _{1 + (K_{LF} * C_e)^n} \qquad \text{(Equation 3.5)}$$

where K_{LF} is the Langmuir-Freundlich affinity constant (mL mg^{-1}), and Qm, Ce and n are the same of above. In this model, the value of the coefficient n is particularly important because it can give information about heterogeneous character of the surface, and about the positive or negative cooperativity between adsorbed molecules.

HPLC analysis of Col

The HPLC quantification of the amount of Col in samples was performed adopting the method reported by Wang et al. [35] with some modifications. It was used an Agilent Eclipse Plus C18 column (250 mm × 4.6 mm, 5 µm, Agilent Technologies, Santa Clara, USA), and the mobile phase was a mixture 76:24% v/v of an aqueous solution of 30 mM Na_2SO_4 and ACN with TFA (0.05% v/v). The elution time of Col was 6.3 min. Sample preparation was performed depending on the sample phase. In particular, liquid samples were diluted 1:1 with a solution of HCl 0,1M, while powdered samples were dissolved in a solution of HCl 0,1M to obtain a concentration of 1mg mL^{-1}. Sample was eluted at a flow rate of 1.0 mL min^{-1}, temperature was set at 25°C, and the wavelength for Col detection was fixed at 215 nm. The linearity of the method was assessed in the range from 0.1 mg mL^{-1} to 0.05 mg mL^{-1} of Col standard solutions in HCl 0.1M.

3.1.3. In vitro experiments

Kinetic release of Col from CaP-NPs

Col release from Col-CaP-NPs was performed in Simulated Interstitial Lung Fluid (SILF), prepared according to the protocol reported by D'Angelo et al. (Table 3.1).[36]

Table 3.1 – Composition of Simulated Interstitial Lung Fluid (SILF)

Reagent	**Concentration (g L^{-1})**
NaCl	6.000
KCl	0.300
$NaHPO_4$	0.157
Na_2SO_4	0.071
$CaCl_2$	0.278
$NaH_3C_2O_2$	0.574
$NaHCO_3$	2.608
$Na_3H_5C_6O_7 \cdot H_2O$	0.098
$MgCl_2 \cdot 6H_2O$	0.294

A Col-CaP-NP suspension at the concentration of 1 mg mL^{-1} were mixed with SILF in a volume ratio of 1:1, (10 mL of suspension with 10 mL of SILF), and put under horizontal shaking at 37°C. At different time points ranging from 15 min to 5 h, the inorganic fraction was separated from the supernatant by centrifugation (10000 rpm, 5 min). An aliquot of

2mL of the supernatant was taken for the HPLC quantification of the released Col, and the same volume of fresh SILF was added in the system.

Interaction of CaP-NPs with artificial mucus

The mucoadhesive tendency of Col and Col-CaP-NPs was studied with the method reported by D'Angelo et al.[36] A saturated aqueous solution of mucin (0.8 mg mL^{-1}) was prepared, stirred for 24 h, and centrifuged (6000 rpm, 20 min at 4°C) to recover the mucin-saturated supernatant. Afterward, aliquots of CaP-NPs, or Col-CaP-NPs were diluted to 1 mL with the mucin-saturated solution and thoroughly mixed. Final concentration of the CaP-NPs was 1 mg mL^{-1}. The samples were incubated at 37°C and the turbidity was measured immediately after mixing and after 30 min, and 1 h. Turbidity was measured as the light absorbance at 650 nm using UV-Vis spectrophotometer. The mucin solution was also analyzed as control. In addition, the ζ-potential of CaP-NPs, and Col-CaP-NPs dispersion in mucin was measured. In this case, samples were prepared as above, but the mucin-saturated solution was diluted 1:4 with water before adding the aliquot of CaP-NP suspensions or Col and citrate solutions. After 30 min of incubation at 25°C, the ζ-potential of the suspensions was measured as reported above.

Furthermore, to determine the ability of CaP-NPs to permeate mucus, diffusion through artificial mucus was investigated by the Institute of Chemical Sciences and Technologies "G. Natta" (SCITEC-CNR) team. They utilized ThinCert® insert (PET membrane, 6 mm diameter, Greiner Bio-One, Alphen a/d Rijn, The Netherlands) with a membrane pore size of 0.4 µm, using fluorescently labeled AF647-CaP-NPs prepared as reported above. Artificial mucus (AM) was prepared as reported by Kirchner et al.,[47] adapting the quantity of each reagent for a total volume of 200 mL. Mucus samples were kept in frozen state until use. After thawing, samples were immediately used. As barrier, 200 µL of AM were homogeneously distributed onto each ThinCert® membrane. The thickness of the mucus barrier was estimated to be around 2 mm. The donor sample consisted of 75 µL of AM and 75 µL of AF647-CaP-NP suspension (1 mg mL^{-1}) or 75 µL of 8mM citrate buffer to obtain a blank to subtract the eventual AM signal. Donor components were previously mixed with mucus to reduce viscosity differences between donor and barrier. As acceptor, 550 µL of an 8 mM citrate buffer were placed in each well. The well plate was stored in a shaker at 37°C under gentle shaking. An aliquot of 100 µL were withdrawn

from the acceptor compartment at predetermined time points (2, 4, 6, and 8 h) and replaced by the same volume of preheated citrate-buffer. AF647-CaP-NP fluorescence was detected in 96 multiwell black plates in a GloMax® Multi Detection System (Promega S.r.l, Milan, Italy) mounting a red filter (λEM 660-720 nm).

Cytotoxicity study

The cytotoxicity study was conducted by the IRCCS Humanitas Research Hospital team. In particular, A549 pulmonary cells were grown in Dulbecco's Modified Eagle's Medium (DMEM) (Lonza, Basel, CH) supplemented with 10% FBS (Sigma-Aldrich, St. Luis, MO, USA), 1% of penicillin-streptomycin (Pen-Strep 10000 U/mi, Lonza, CH), 1% of L-glutamine 1 (200 mM, Lonza, CH) and incubated at 37°C with 5% CO_2. At full confluence, cells were split 1:5. The effect of Col-CaP NPs on A549 cell viability was analyzed using RealTime-Glo™ MT Cell Viability Assay kit (Promega S.r.l, Milan, Italy) according to the manufacturer's instructions. Briefly, 8x103 cells/well were seeded in white-walled 96-well plates. 24 h after plating, A549 cells were treated with different concentrations of CaP-NPs or Col-CaP-NPs as indicated in the text. Col, citrate buffer and DMSO 10% were used ad controls. To continuously monitor the viability of treated A549 cells in real time, RealTime-Glo reagents were added at the same time as CaP-NPs.

Luminescence intensity, as measure of viable cells, was detected at the desired time points up to 24h using a microplate reader GloMax® Discover Microplate Reader (Promega S.r.l, Milan, Italy). Three biological and technical replicates were carried out. Viability, cytotoxicity, and caspase-3/7 activities were measured after 24 h of CaP-NP treatment using the ApoTox-Glo triplex Assay (Promega S.r.l, Milan, Italy) according to the manufacturer's instructions. A549 cells were seeded at a density of 8x103 cells/well in black-walled 96-well plates. 24 h after plating, different doses of CaP-NPs or Col-CaP-NPs were administered as indicated in the text. Col, citrate buffer and DMSO 10% were used ad controls. Cell viability fluorescence was measured at 400Ex/505Em, cytotoxicity fluorescence at 485Ex/520Em, while apoptosis was determined with the bioluminescence measurement using a microplate reader, GloMax® Discover Microplate Reader (Promega S.r.l, Milan, Italy). Three biological and technical replicates were carried out.

Interaction of CaP-NPs with A549 pulmonary cells

The permeation of CaP-NPs in A549 cells was observed by the Institute of Chemical Sciences and Technologies "G. Natta" (SCITEC-CNR) team with an inverted Nikon A1-MP confocal microscope (Nikon Europe BV, Amsterdam, NL) performing the images at 37°C - 5% CO_2 (on-stage incubator, OKOLAB, Naples, Italy). Cells were seeded in a µ-slide 8 wells chamber (Ibidi, Gräfelfing, Germany), and grown for one day in DMEM medium. The day of the observation, two groups of cells were inoculated with 50 µl/well of a AF647-CaP-NPs suspension (1 mg mL^{-1}); one group left to interact with cells for 20 min and the second for 40 min after while cells were gently washed twice with PBS to remove cell debris and non-internalized CaP-NPs. Fluorescence images (excitation: 402 nm for the blue channel and 640 nm for red channel) were collected in two separated channels (emission filter: 450/50 nm for the blue channel, 595 nm for the red channel) using a 20x Plan apo objective with a 0.75 numerical aperture.1024 x 1024-pixel at 12-bit images were collected at 30 min (first group) and 1 h (second group) after inoculum.

3.1.4. Microbiological experiments

The microbiological experiments were conducted by the Department of Basic Biotechnological Sciences, Intensivological and Perioperative Clinics (Università Cattolica del Sacro Cuore) team.

Bacterial Strain, Media and Culture Conditions

RP73, a PA clinical strain isolated from a CF patient suffering from chronic lung infection,[48] was tested for purity on Brain Heart Infusion (BHI) plates and grown for biofilm formation in 1:2 dilution BHI broth with 0.25% glucose (BHI-G).

Minimum inhibitory concentration determination

Minimum inhibitory concentration (MIC) was evaluated using standard broth microdilution following EUCAST recommendations.[49] A bacteria suspension (0.5 MacFarland) was prepared, diluted in Muller-Hinton broth, and incubated in the susceptibility panel containing free Col and Col-CaP-NPs at different Col concentrations ranging from 0.125 to 64 mg L^{-1}. Samples of CaP NPs with the same quantity of NPs of Col-CaP-NPs samples were also tested. After 24 h of incubation at 37°C, the MIC was

defined as the lowest concentration of the compound that totally inhibited the bacterial growth.

Biofilm Conditions and Chemicals

RP73 PA strain was cultured in BHI and grown at 37°C overnight, harvested by centrifugation (3000 ×g, 10 min), resuspended in sterile PBS, and adjusted to a density of 109 colony-forming-units (CFU) mL^{-1} in BHI-G media by measuring the absorbance at 600 nm. A 24 wells plates with 13 mm diameter glass coverslips (Thermanox NUNC, Naperville, IL, USA) was seeded with 500 mL of bacterial suspension and grown 5 days at 37°C for biofilm formation.

Biofilm Demolition Assay

Once the biofilms were formed, after 5 days of incubation, the culture medium was removed, and the samples washed with PBS to remove non-adherent cells. The biofilm was then treated with Col, and Col-CaP-NPs at a Col concentration of 50 μg mL^{-1} for 24 h at 37 °C. A sample of CaP NPs with the same quantity of NPs of Col-CaP-NPs sample was also tested. The demolition activity was measured by CFU valuation assay and observed by SEM (Supra 25-Zeiss, Carl Zeiss AG, Oberkochen, Germany). Fixed and dried biofilms were mounted onto an aluminum stab using double-sided carbon tape and coated with a gold/palladium film (80:20) by using a high-resolution sputter coater (SCD-040, Balzers Union Ltd, Balzers, Lichtenstein).

CFU valuation assay

After compounds incubation and accurately washed, each well of adherent cells were filled with 0.5 mL of PBS and the biofilm was detached from the surfaces by water bath sonication (BactoSonic, Bandelin, Berlin, Germany) for 45 min at 100% power. Serial dilution 10^{-3}, 10^{-5} and 10^{-7} were spread on MacConkey agar plates (Oxoid Ltd, Basingstoke, UK) and incubated at 37°C overnight. Microbial counts were expressed as CFU mL^{-1}. Untreated biofilm was grown as positive control. Results were statistically analyzed by GraphPad Prism (version 5.0, GraphPad Software Inc., San Diego, CA, USA). Statistically significant differences between two groups were assessed by a two-tailed unpaired t-test (p-value < 0.05).

3.2. Results and discussion

3.2.1. CaP-NPs characterization

The production of CaP NPs characterized by a significantly negatively charged surface suitable for its interaction with the positively charged Col, was performed by a citrate-based thermal decomplexing method. Moreover, the preparation of CaP NPs has required the addition of carbonate ions to achieve a small size distribution of the final product. In agreement with the previously published data in Delgado-López et al. article,[40] the PXRD pattern (Figure 3.2A) reveals that CaP-NPs are composed of pure HA phase (#009-0432) having a poor degree of crystallinity. TEM micrograph of the sample (Figure 3.2B) indicates that the particles are elongated platelets with dimensions along the major axis of about 50-100 nm. The selected area diffraction (SAED) pattern (inset of Figure 3.2B) shows diffusive borders in agreement with the low crystallinity degree.

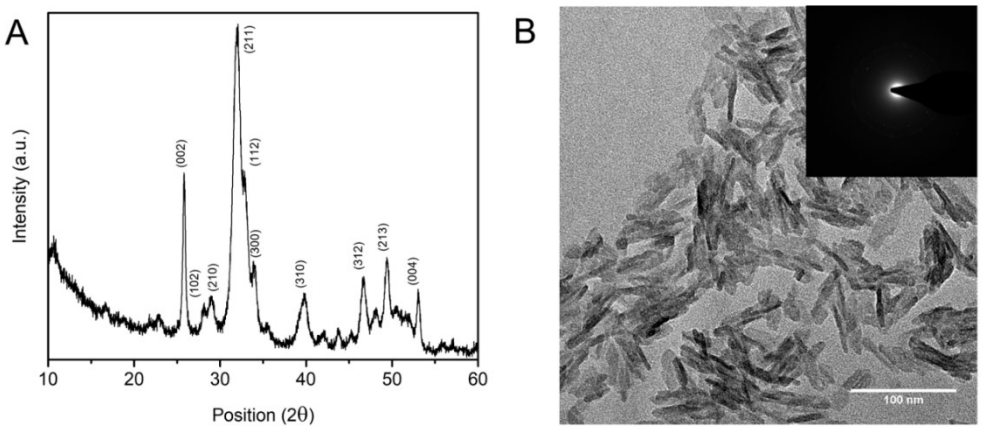

Figure 3.2 - (A) PXRD pattern and (B) TEM micrograph of CaP NPs. Inset of B: SAED pattern

3.2.2. Col-CaP-NP characterization

The Col-CaP-NPs characterization was initially conducted in two steps. Firstly, it was performed the kinetic adsorption of Col on CaP NPs, as reported in paragraph 3.1.3, and then the isothermal adsorption was also executed (Figure 3.3). Both the experiments have been fitted to the most commonly used models (3.1.3 paragraph).

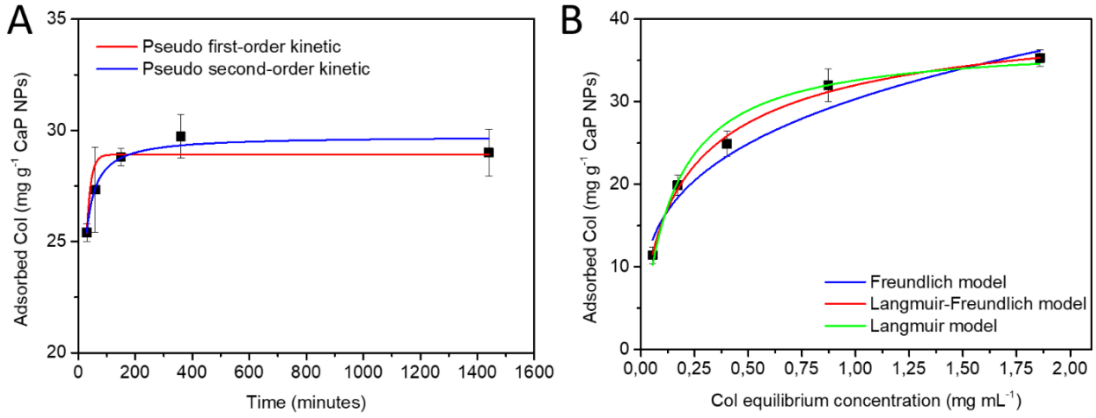

Figure 3.3 -(A) Kinetic and (B) isotherm adsorption of Col on CaP-NPs. Separate points are the experimental data (mean values and standard deviation for n=6); lines indicate fits of kinetic and isotherm data

As reported in Figure 3.3A, the kinetic adsorption of Col on CaP NPs shows that the drug adsorbed amount increases as a function of time with a first rapid rise followed by a progressive stabilization (or plateau) up to almost 30 mg of Col per g of CaP-NPs. The plateau was reached after 150 min, therefore this value was selected as the optimized contact time for the following isothermal adsorption study. The kinetic data have been fitted to pseudo first-order and pseudo second-order (Figure 3.3A), and the relative parameters are listed in Table 3.2.

Table 3.2 – Kinetic adsorption parameters calculated from the curve fitting of experimental data according to the pseudo first-order and pseudo second-order models

Model	Adjusted R^2	$Q_{ads,e}$ (mg Col/g CaP-NPs)	k_1/k_2 (min^{-1})
Pseudo first-order	0.9665	28.9 ± 0.2	0.070 ± 0.003
Pseudo second-order	0.9839	29.7 ± 0.2	0.20 ± 0.01

Table 3.2 highlights that pseudo second-order model gives a better R^2 coefficient (0.984) than the pseudo first-order (R^2 = 0.966). This slight R^2 coefficient difference suggests that the pseudo second-order model better describes the Col-CaP-NPs system. In particular, it indicates that the adsorption of the drug is not totally reversible and involves an interaction between Col and the surface of CaP NPs.[50] Indeed, it is probable that the electrostatic interactions between the positively charged amine groups of Col (at physiological pH) with the negatively charged carboxylate anions (i.e., citrate) of the surface of CaP NPs can be the main interaction that drive the Col adsorption. On the other hand, it is worth to mention that both models do not give an excellent fitting and both curves are comprised within the experimental error. This is probably due to the

complexity of the system, indeed non-integer reaction orders were reported for other complex and heterogeneous systems.[51]

Moreover, in Figure 3.3B is reported the adsorption isotherm curve conducted at 37 °C. It is characterized by a moderately steep increase of the adsorbed amount, followed by a progressive evolution toward stabilization up to about 35 mg of Col per g of CaP-NPs. This trend is comparable to monolayer coverage of adsorbed molecules on NPs. The curve was fitted with three different models, namely Langmuir, Freundlich and Langmuir-Freundlich, and the best fitting results are reported in Table 3.3.

Table 3.3 - Adsorption isotherm parameters calculated from the curve fitting of experimental data according to the Langmuir, Freundlich and Langmuir–Freundlich models.

Model	**Adjusted R^2**	Q_m **(mg Col/g CaP-NPs)**	K_L / K_F / K_{LF} **(mL mg^{-1})**	***n***
Langmuir	0.9798	37 ± 1	7 ± 1	-
Freundlich	0.9621	-	30 ± 1	3.50 ± 0.40
Langmuir-Freundlich	0.9951	44 ± 4	4 ± 1	0.70 ± 0.09

Although fitting with the Langmuir isotherm model gave an acceptable R^2 coefficient (0.980), an even better fitting was found with the Langmuir-Freundlich model (R^2 = 0.995). The Freundlich model, instead, gave an even lower correlation coefficient respect to the Langmuir model (R^2 = 0.962). The value of the exponent n, in the Langmuir-Freundlich model, was lower than 1 suggesting that a negative cooperativity between the adsorbed molecules may occurred. For this reason, it could be hypothesised that adsorbed Col molecules hinder the further adsorption of Col. The relative value of Q_m, which is related to the maximum loading capacity, reached almost 43.7 mg of Col per g of CaP NPs, corresponding to a drug payload of ca. 4 wt. %.

The adsorption of Col on CaP NPs was compared to adsorption reported in literature of several antibiotics such as chlorhexidine, ciprofloxacin, cethylpiridinium chloride (CPC), and tetracycline on CaP NPs.[51–54] In all these cases, the best fitting was achieved with the Langmuir-Freundlich model, except for cethylpiridinium chloride where only Langmuir model was used. The model parameters obtained from these fittings are reported in Table 3.4.

Table 3.4 - Isotherm adsorption parameters taken from literature of several antibiotics onto CaP NPs according to the Langmuir and Langmuir–Freundlich models

Drug	Langmuir-Freundlich Q_m (mg g^{-1})	Langmuir-Freundlich *n*	Langmuir-Freundlich K_{LF} (mL mg^{-1})
Colistin (this work)	44.0 ± 4.0	0.70 ± 0.09	4 ± 1
Chlorexidine[a]	43.1 ± 4.0	6.60 ± 1.50	28 ± 7
Ciprofloxacin[b]	2.9 ± 0.1	0.98 ± 0.07	602 ± 249
Tetracycline[c]	36.4 ± 1.1	1.08 ± 0.06	6.7 ± 1.4
	Langmuir Q_m (mg g^{-1})	**-**	**Langmuir K_L (mL mg^{-1})**
CPC (spherical shaped hydroxyapatite NPs)[d]	43	-	4118
CPC (long rod shaped hydroxyapatite NPs)[d]	28	-	8030

[a] from Soriano de Souza et al.[53]; [b] from Benedini et al.[52]; [c] from Cazalbou et al.[51]; [d] from Okada et al.[54]

It can be observed that Q_m value of Col is similar to the values reported for chlorhexidine and cethylpiridinium chloride (only on spherical HA NPs with high surface area), while is higher than tetracycline and ciprofloxacin. It is interesting to note that only Col has a n value lower than 1 that indicates negative cooperativity. Tetracycline and ciprofloxacin, instead, not show cooperativity, and finally the higher value of n for chlorhexidine suggest a strong positive cooperativity. These data suggest that the cooperativity during adsorption is more related to the drug chemical structure than on CaP NP properties. Moreover, the maximal amount of adsorbed drug is mainly controlled by CaP NP available surface area and surface features, and not only by the nature of the interaction between the drug and CaP NPs. Furthermore, sizes, polydispersity indexes, and surface charges of CaP NPs and Col-CaP-NPs at different Col payload were measured at concentration of 1 mg mL^{-1} and pH of 7 (Table 3.5).

Table 3.5 - Colistin payload, hydrodynamic diameter, polydispersity index and ζ-potential of Col-CaP-NPs dispersed in ultrapure water (pH 7) after the functionalization with colistin.

Sample / Initial Col concentration (mg mL^{-1})	Colistin payload (wt. %)	Hydrodynamic diameter (nm)	Polydispersity index	ζ-potential (mV)
CaP-NPs	-	95 ± 5	0.26 ± 0.04	-39.0 ± 2.0
Col-CaP-NPs / 0.10	1.14 ± 0.10	3527 ± 368	0.23 ± 0.03	-7.8 ± 0.2
Col-CaP-NPs / 0.25	1.99 ± 0.12	3696 ± 445	0.11 ± 0.07	-5.1 ± 0.1

Col-CaP-NPs / 0.50	2.49 ± 0.15	3273 ± 500	0.11 ± 0.07	-4.6 ± 0.1
Col-CaP-NPs / 1.00	2.90 ± 0.20	3874 ± 404	0.13 ± 0.06	-3.7 ± 0.1
Col-CaP-NPs / 2.00	3.53 ± 0.10	3895 ± 385	0.20 ± 0.10	-2.8 ± 0.1

In comparison to CaP NPs, samples conjugated with Col are aggregated, with a measured mean hydrodynamic radius of about 3-4 µm. Moreover, the surface charge of CaP NPs moves from the very negative value (-33 ± 1 mV) of unloaded NPs towards neutrality as a function of Col payload. This shift confirms the electrostatic interaction between negatively charged citrate groups on CaP NP surface with positively charged Col. This generates an aggregation phenomenon between Col-CaP-NPs that results in the formation of particles with micrometric hydrodynamic diameters. In view of their application, a new layer of citrate ions was added to the NPs to reduce Col-CaP-NPs aggregation. In detail, similarly to the method reported by Sandhofer et al.,[41] after Col adsorption and washing of unabsorbed drug, Col-CaP-NPs were suspended in a citrate buffer solution at pH 8 at 8 mM concentration. Size and surface charge of the samples enriched with citrate are reported in Table 3.6.

Table 3.6 - Hydrodynamic diameter, polydispersity index and ζ-potential of Col-CaP-NPs dispersed in a citrate solution 8mM (pH 8) after the functionalization with colistin

Sample	Initial colistin concentration (mg mL^{-1})	Hydrodynamic diameter (nm)	Polydispersity index	ζ-potential (mV)
Col-CaP-NPs	0.10	205 ± 1	0.23 ± 0.01	-40 ± 2
Col-CaP-NPs	0.25	201 ± 2	0.22 ± 0.01	-38 ± 1
Col-CaP-NPs	0.50	219 ± 2	0.27 ± 0.02	-37 ± 2
Col-CaP-NPs	1.00	213 ± 1	0.26 ± 0.03	-37 ± 1
Col-CaP-NPs	2.00	230 ± 3	0.28 ± 0.04	-35 ± 2

The results show that the further treatment of Col-CaP-NPs with citrate leads to a good dispersion of the aggregates, as suggested by the mean hydrodynamic diameter lowering down up to 201 nm. The ζ-potential moves back to negative values between -35 and -40 mV. The surface charge became less negative in the samples with higher Col payload, as Col was not removed by the citrate treatment and counteracted the negative charge due to citrate. Considering the results obtained and reported in the previous Table 3.5 and 3.6, the Col optimized adsorption on CaP NPs was set at 37 °C for 150 min by using a

concentration of Col of 1 mg mL^{-1}. In these conditions the average payload of Col was 29 ± 2 mg of Col per g of CaP NPs, which corresponds to ca. 3 wt.% of drug loading. Therefore, the size and surface charge parameters of CaP NPs and Col-CaP NPs, prepared with the optimized method of adsorption, used for the in vitro studies are reported in Table 3.7.

Table 3.7 - Size and surface charge parameters of CaP-NPs and Col-CaP-NPs in citrate 8 mM buffer

	CaP-NPs	**Col-CaP-NPs**
Col loading (mg Col/g CaP)	-	29 ± 2
Hydrodynamic diameter (nm)	95 ± 5	213 ± 1
Polydispersity Index (PDI)	0.26 ± 0.04	0.26 ± 0.03
ζ-Potential (mV)	-33 ± 2	-37 ± 4

The final formulation of Col-CaP-NPs has a hydrodynamic diameter that is higher than CaP NPs due to the presence of Col. However, based on the studies of Cone et al., Sanders et al., and Ungaro et al. such size is considered still suitable for crossing the mucus barrier (250 – 300 nm of size is thought to be the maximal threshold value).[55–57] On the other hand, the ζ-potential is almost the same for both samples due to the presence of citrate ions stabilizing the suspension.

Subsequently, CaP NPs and Col-CaP-NPs were analysed by FT-IR spectroscopy and FEG-SEM microscopy (Figure 3.4).

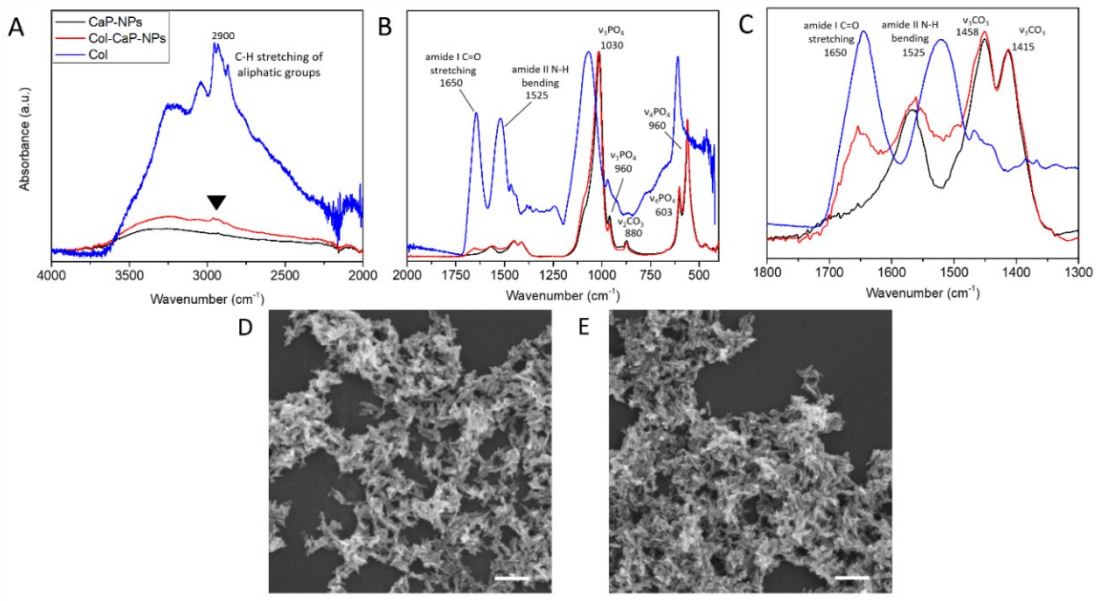

Figure 3.4 - FT-IR spectra of powdered Col, CaP-NPs, and Col-CaP-NPs in the (A) 4000-2000 cm^{-1} and (B) 2000-500 cm^{-1} spectral range and (C) magnification in the 1800-1300 cm^{-1} spectral range. FEG-SEM micrographs of (D) CaP NPs, and (E) Col-CaP-NPs. Magnification: 150000 X. Scale bar: 200 nm

The FT-IR spectra, reported in Figure 3.4A-C, reveal that in Col-CaP-NPs the signals of Col at 1650 and 1525 cm^{-1} attributed to amide I C=O stretching and amide II N-H bending vibrations, respectively[58] are present as new peaks or shoulders of CaP carboxylate bands at 1400-1600 cm^{-1}. In addition, a weak group of peaks at 2900 cm^{-1} due to C-H stretching of aliphatic groups of Col can be observed, confirming the presence of Col in Col-CaP-NPs. The FEG-SEM micrographs of CaP-NPs and Col-CaP-NPs, showed in Figure 3.4D-E, shows that both samples are constituted by elongated NPs with size of about 100 nm. This indicates that Col functionalization did not change the NPs morphology.

Subsequently, it was studied the variation of the ζ-potential of the optimized Col-CaP-NPs in function of pH (Figure 3.5) to better understand the stability of the suspension.

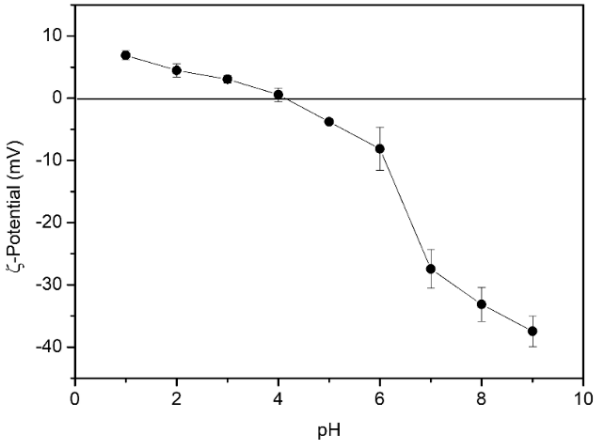

Figure 3.5 - ζ-potential values of Col-CaP-NPs suspension in function of pH of the medium

In particular, high ζ-potential values (either negative or positive) generate electrostatically stabilized suspensions while low ζ-potentials are typical of poorly stable suspensions with coagulation or flocculation phenomena. As reported in Figure 3.5, Col-CaP-NPs ζ-potential is stable at ca. -35 mV from pH 11 to pH 7, while from pH 6 to pH 4 the ζ-potential falls to neutrality. At pH values lower than 4, ζ-potential values become positive because of CaP NP degradation and the consequent detection of detached positively charged Col in solution. These data also show the possibility of using Col-CaP-NPs as pH-triggered drug delivery system thanks to its stability at physiological pH paired with a controlled degradation at low pH (< 6), which prompts the drug release.

Afterwards, the release of Col from Col-CaP-NPs was tested in SILF and the curve is reported in Figure 3.6.

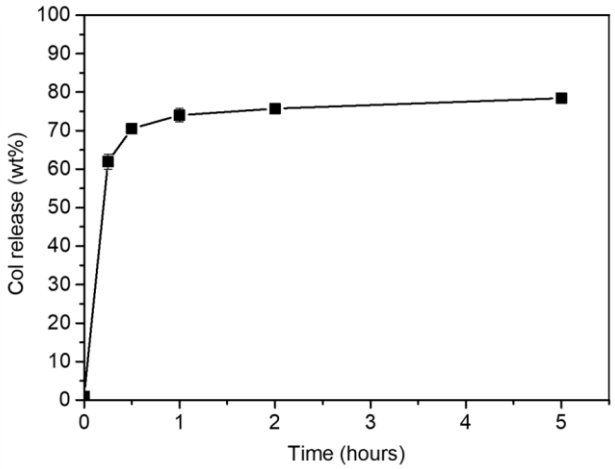

Figure 3.6 - Kinetic release curve of Col from Col-CaP-NPs in SILF

Col undergoes a burst release in the first hours, then gradually tapers off to a plateau. After 5 h, approximately the 70% of the loaded amount of Col has been released. A similar release profile of Col was observed in Col-loaded nano-liposomes.[31,59] In detail, in several formulations based on liposomes ca. 40–60 % of loaded Col was released within the first 2 hours, as for Col-CaP-NPs.[31,59,60]

3.2.3. Interaction of CaP NPs and Col-CaP-NPs with artificial mucus

The efficacy of NPs to permeate mucus depends on their size and on their interactions with components of mucus.[7] Indeed, it is important to avoid adherence between NPs and the lipophilic or negatively charged parts of the loosely packed mucin matrix (i.e., muco-adhesion). The adhesion mechanism of NPs to mucus are predominantly based on electrostatic interactions, even if hydrophobic or hydrogen-bond interactions can occur.[61] Positively charged NPs are more likely to adhere to the mucus layer retarding its diffusion due to their electrostatic interaction with the negatively charged mucin. However, negatively charged, or neutral NPs can also be problematic as they can be repelled from the mucus by the hydrophobic domains on the mucins. Here, the interaction of CaP-NPs with mucin and the ability to cross a layer of artificial mucus was assessed. Muco-adhesion was studied by measuring the turbidity (absorbance at 650 nm) of a dispersion of CaP-NPs and Col-CaP-NPs in mucin (Table 3.8), the main component of airways mucus, as reported before.[36]

Table 3.8 - Turbidity of samples of mucin enriched with CaP NPs and Col-CaP-NP

Sample	Time (min)	Abs (650 nm)
Mucin only	0	0.012 ± 0.002
	30	0.010 ± 0.003
	60	0.015 ± 0.004
Mucin + CaP-NPs (1 mg mL^{-1})	0	0.057 ± 0.002
	30	0.038 ± 0.003
	60	0.025 ± 0.001
Mucin + Col-CaP-NPs (1 mg mL^{-1})	0	0.029 ± 0.001
	30	0.015 ± 0.004
	60	0.010 ± 0.002

In table 3.8, it can be observed that after 1 h of incubation there was no difference in turbidity between mucin alone and mucin with CaP-NPs or Col-CaP-NPs. Indeed, it is possible to notice that in all cases the absorbance at 650 nm remained below 0.06, that is a value that indicate the absence of muco-adhesion.[36] This means that both CaP NPs and Col-CaP-NPs did not interact with mucin. Furthermore, this was confirmed by ζ-potential measurements (Table 3.9).

Table 3.9 - ζ-potential of samples of mucin enriched with CaP-NPs and Col-CaP-NPs (pH 7)

Sample	ζ-potential (mV)
Mucin only	-24 ± 1
Mucin + CaP-NPs (1 mg mL^{-1})	-29 ± 2
Mucin + Col-CaP-NPs (1 mg mL^{-1})	-26 ± 1

Table 3.9 shows that the reference mucin dispersion has a negative ζ-potential (-24 ± 1 mV) that was not significantly perturbed by the presence of negatively charged CaP NPs (-29 ± 2 mV) or Col-CaP-NPs (-26 ± 1 mV). Therefore, it is possible to state that the negative charge of Col-CaP-NPs does not generate electrostatic attraction with mucin that could lead to adhesion and NPs trapping in mucus.

Afterwards, the ability to cross a layer of AM was tested in vitro by employing fluorescent AF647-CaP-NPs (Figure 3.7).

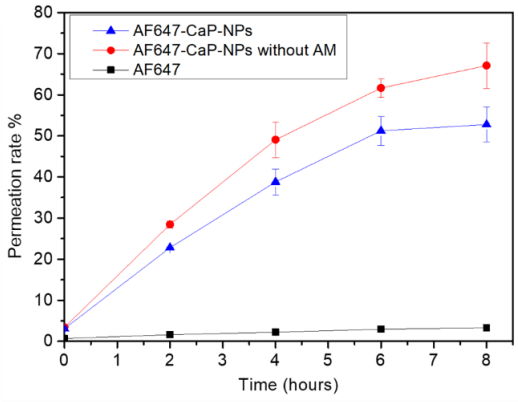

Figure 3.7 - Permeation rate of AF647-CaP-NPs through AM. The permeation rate of free AF647 dye through AM and AF647-CaP-NPs in absence of AM are also displayed as comparison

In Figure 3.7 are reported the percentages of CaP-NPs permeation through an AM barrier within 8 h. In particular, the percentages showed are referred to the nominal amounts of the AF647 dye and the AF647-CaP-NPs used in the experiment. Through this analysis it was possible to verify the ability of CaP-NPs to cross the AM barrier, confirming the lack of interaction with mucin and with other molecules usually found in natural mucus (DNA, phospholipids, etc).

3.2.4. In vitro test of NPs

Cytotoxicity tests

The effects of CaP NPs towards pulmonary cells were investigated to develop a formulation which can be administered by inhalation. A549 pulmonary cells were treated with incremental doses of CaP NPs and Col-CaP-NPs (from 0 to 125 µg mL^{-1}) and their viability were analysed using a bioluminescent assay (Figure 3.8).

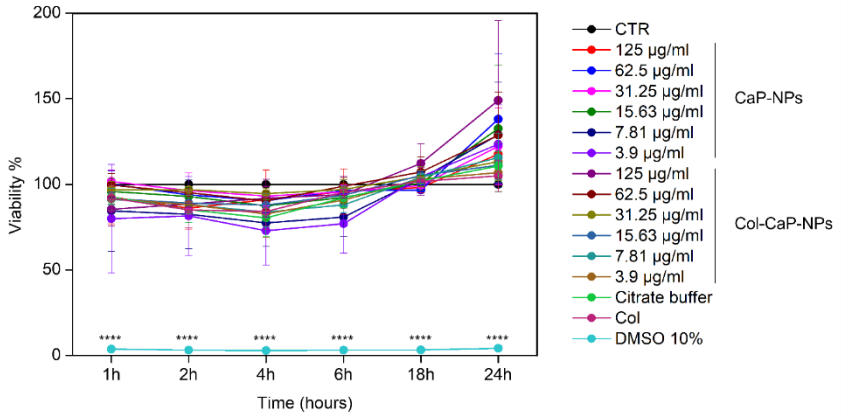

Figure 3.8 - Temporal monitoring of cell viability of A549 pulmonary cells after treatment with increasing doses of Col-CaP-NPs during 24 h. Empty CaP-NPs, free Col and citrate buffer were used as negative controls. DMSO 10% was used as toxic control. All data is represented as the mean value of 3 runs.

As shown in Figure 3.8, A549 cells largely tolerated an acute administration of Col-CaP-NPs showing more than 90% viability up to 125 µg mL^{-1} of Col-CaP-NPs at 24 h post-administration. Moreover, no change in cell viability was also found by treating A549 cells with CaP-NPs, citrate buffer and free Col, used as controls. On the other hand, as expected, a cytotoxic effect was detected administering only DMSO 10%, with detrimental effects starting a few hours post administration. Subsequently, A549 cells were exposed to incremental doses of Col-CaP-NPs in order to also evaluate the biocompatibility of the developed material. For this reason, an analysis of viability, cytotoxicity, and caspase 3/7 activity was performed at 24 h post-treatment (Figure 3.9).

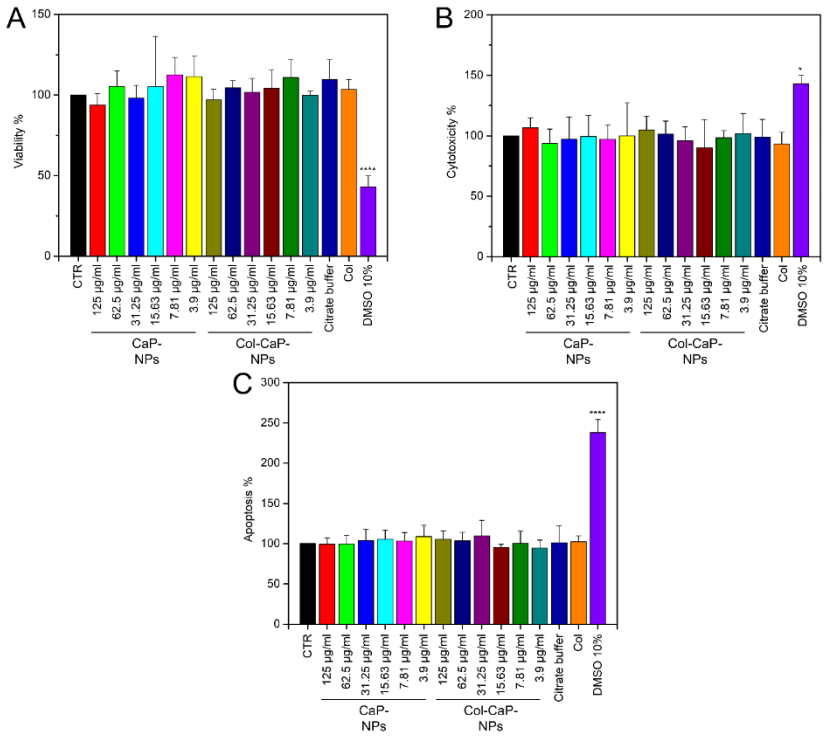

Figure 3.9 - Correlation of viability (A), cytotoxic (B) and apoptotic (C) levels' detection via the activated caspase 3/7 assay in A549 cells treated with increasing concentrations of Col-CaP-NPs for 24 h. Empty CaP-NPs, free Col and citrate buffer were used as negative controls. DMSO 10% was used as toxic control. (n=3). All data is represented as the mean value of 3 runs.

From Figure 3.9 is possible to confirm prior data. Indeed, A549 cells well tolerated the administration of Col-CaP-NPs without showing any effect in terms of cytotoxicity or sign of apoptosis up to 125 µg mL^{-1} unlike the positive control DMSO 10%. Overall, the toxicity tests performed on Col-CaP-NPs show relevant biocompatibility comparable to other previously reported unloaded CaP NPs.[38,62] Finally, to evaluate the interaction with A549 cells and verify the possible internalization of CaP-NPs in model lung cells, confocal

images were collected at two different time points (30 min and 1h) after the treatment with AF647-CaP-NPs (Figure 3.10).

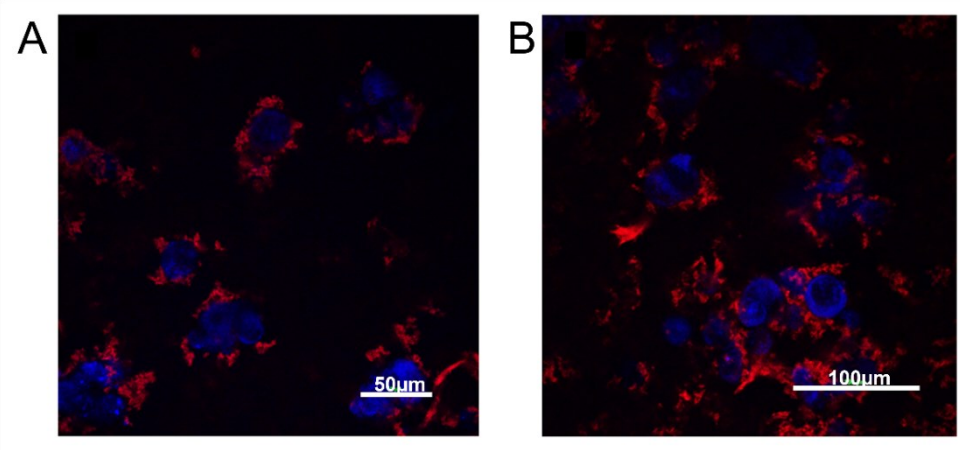

Figure 3.10 - Confocal Laser Scanning images of A549 cells treated with 50 µg of AF647-CaP-NPs. Images collected after (A) 30 min and (B) 1 h upon AF647-CaP-NPs administration.

Figure 3.10 reports images of A549 cells treated with AF647-CaP-NPs obtained by using Confocal Laser Scanning. In particular, red channel (excitation at 640 nm) evidences AF647-CaP-NPs internalized within A549 cells, while blue channel (excitation at 402 nm) evidences H33342 staining of nuclei. This indicates that CaP-NPs are internalized in a discrete amount in cells even after 40 min upon treatment. From these images is possible to assert that CaP-NPs do not induce cytotoxicity effects even if they are internalized inside cells.

3.2.5. Antimicrobial susceptibility test.

Determination of MICs

The MIC values of the samples against PA RP73[48] (a clinical strain isolated from a CF patient suffering from chronic lung infection) are summarized in Table 3.10.

Table 3.10 - MICs values calculated according to the EUCAST broth microdilution protocol of Col, Col-CaP-NPs and CaP-NPs against PA RP73

Samples	Col	Col-CaP-NPs	CaP-NPs
MIC (µg mL^{-1})	0.5	0.5	>50

As it is possible to notice from Table 3.10, no difference was observed between the values obtained with free Col or Col-CaP-NPs. It should be noted that the CaP NPs did not show

any bacteriostatic or bactericidal effect indicating they did not contribute to Col-CaP-NP activity.

Antibiofilm activity evaluation of NPs on PA RP73

The mature biofilm of PA RP73 was treated with Col and Col-CaP-NPs, in order to evaluate the antibiofilm properties of free and conveyed Col. Subsequently, the CFU mL^{-1} remaining adhered to the surface were counted and the SEM images were analysed to evaluate the morphological modification of the bacterial biofilm (Figure 3.11).

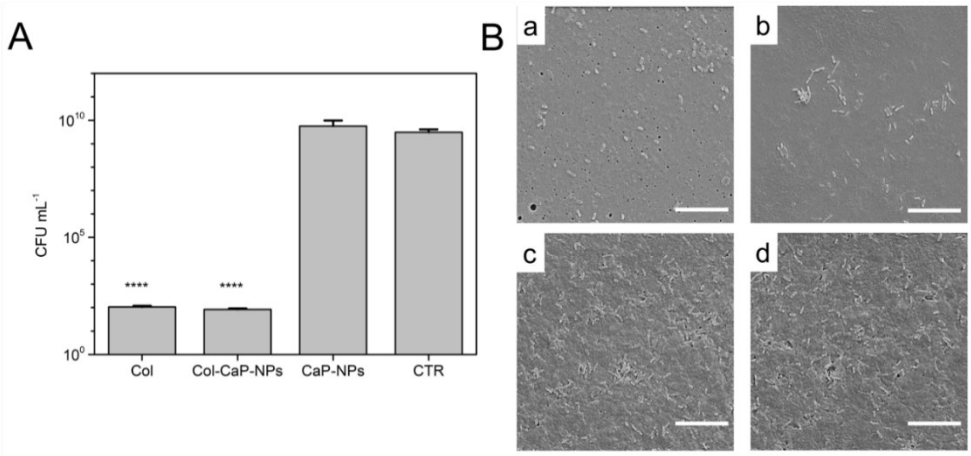

Figure 3.11 - (A) CFU mL^{-1} obtained treating the RP73 PA biofilm with the different compounds; CTR: untreated biofilm. The graph shows the average and standard error of 3 replicates. (B) SEM images of the RP73 PA biofilm after treatment with (a) free Col, (b) Col-CaP-NPs and (c) CaP-NPs; (d) Untreated biofilm. Magnification: 6000 X. Scale bar: 10 µM

Data reported in Figure 3.11A show a significant reduction in CFU mL^{-1} obtained from RP73 PA biofilm treated with both Col and Col-CaP-NPs (at the same Col concentration) compared to untreated biofilm or treated with CaP NPs only. Furthermore, in Figure 3.11B SEM images from PA RP73 biofilm show how, in accordance with the data obtained on the CFU mL^{-1} count, Col and Col-CaP-NP treatments heavily affect the biofilm structure. The demolition of the PA RP73 biofilm treated with the active compounds appears evident from the great reduction of microbial cells that clearly lose their three-dimensional organization. On the other hand, the untreated biofilm or treated with CaP NPs only appears highly organized, with numerous cells strongly adhering to the surface and immersed in the extracellular matrix.

3.3. Conclusion

The study reported in this chapter provides the proof of concept for an innovative inhalable CaP NP based drug delivery system potentially able to counteract PA infection in CF. Our results have demonstrated that CaP NPs can be functionalized with antimicrobial Col with a payload up to 30 mg of Col per g of CaP NPs. In particular, the functionalization could occur thanks to the electrostatic interaction between the positively charged amine groups of Col and the negatively charged surface of CaP NPs. Once functionalized, Col-CaP-NPs dispersed in citrate solution (8 mM) maintained a size (215 nm) suitable for crossing the mucus barrier. In addition, it was verified that the system CaP NPs based do not interact with mucin and can penetrate a layer of artificial mucus. Furthermore, in vitro tests on pulmonary cells have proved that CaP NPs are not cytotoxic as cells largely tolerate their acute administration, showing an increase in mortality rate only at high doses (> 125 μg mL^{-1}). Concerning microbiological experiments performed on PA clinical strain isolated from a CF patient, it was observed that Col adsorbed on CaP-NPs retains its therapeutic effect and presents antimicrobial and antibiofilm efficacy similar to free Col. These previous reported properties might allow drug entry into biofilms, altering cells organization at the infection site.

In conclusion, despite other key investigations such as *in vivo* tests in murine models of CF infection are needed, the promising results of this work pave the way to further formulation optimization studies. On the other hand, CaP NPs are certainly considered one of the novel promising nanomaterials in the treatment of CF to overcame antibiotics resistance.

References:

1. R. K. Patel, P. Cystic Fibrosis in Human - A Review. *Curr. Trends Biotechnol. Pharm.* **14**, 448–457 (2020).
2. Savla, R. & Minko, T. Nanotechnology approaches for inhalation treatment of fibrosis. *J. Drug Target.* **21**, 914–925 (2013).
3. da Silva, A. L., Cruz, F. F., Rocco, P. R. M. & Morales, M. M. New perspectives in nanotherapeutics for chronic respiratory diseases. *Biophys. Rev.* **9**, 793–803 (2017).
4. Haque, A. K. M. A. *et al.* Chemically modified hCFTR mRNAs recuperate lung function in a mouse model of cystic fibrosis. *Sci. Rep.* **8**, 16776 (2018).
5. Ibrahim, B. M., Tsifansky, M. D., Yang, Y. & Yeo, Y. Challenges and advances in the development of inhalable drug formulations for cystic fibrosis lung disease. *Expert Opin. Drug Deliv.* **8**, 451–466 (2011).
6. Cristallini, C. *et al.* Biodegradable microparticles designed to efficiently reach and act on cystic fibrosis mucus barrier. *Mater. Sci. Eng. C* **95**, 19–28 (2019).
7. Velino, C. *et al.* Nanomedicine Approaches for the Pulmonary Treatment of Cystic Fibrosis. *Front. Bioeng. Biotechnol.* **7**, (2019).
8. Malhotra, S., Hayes, D. & Wozniak, D. J. Cystic Fibrosis and Pseudomonas aeruginosa: the Host-Microbe Interface. *Clin. Microbiol. Rev.* **32**, (2019).
9. Alikhani, Z., Salouti, M. & Ardestani, M. S. Synthesis and immunological evaluation of a nanovaccine based on PLGA nanoparticles and alginate antigen against infections caused by Pseudomonas aeruginosa. *Biomed. Phys. Eng. Express* **4**, 045016 (2018).
10. Pang, Z., Raudonis, R., Glick, B. R., Lin, T.-J. & Cheng, Z. Antibiotic resistance in Pseudomonas aeruginosa: mechanisms and alternative therapeutic strategies. *Biotechnol. Adv.* **37**, 177–192 (2019).
11. C Reygaert, W. An overview of the antimicrobial resistance mechanisms of bacteria. *AIMS Microbiol.* **4**, 482–501 (2018).
12. Moradali, M. F., Ghods, S. & Rehm, B. H. A. Pseudomonas aeruginosa Lifestyle: A Paradigm for Adaptation, Survival, and Persistence. *Front. Cell. Infect. Microbiol.* **7**, (2017).
13. Nation, R. L. & Li, J. Colistin in the 21st century. *Curr. Opin. Infect. Dis.* **22**, 535–543

(2009).

14. Leyo. https://commons.wikimedia.org/w/index.php?curid=10599216.
15. Ayoub Moubareck, C. Polymyxins and Bacterial Membranes: A Review of Antibacterial Activity and Mechanisms of Resistance. *Membranes (Basel).* **10**, 181 (2020).
16. Lim, L. M. *et al.* Resurgence of Colistin: A Review of Resistance, Toxicity, Pharmacodynamics, and Dosing. *Pharmacotherapy* **30**, 1279–1291 (2010).
17. Conole, D. & Keating, G. M. Colistimethate Sodium Dry Powder for Inhalation: A Review of Its Use in the Treatment of Chronic Pseudomonas aeruginosa Infection in Patients with Cystic Fibrosis. *Drugs* **74**, 377–387 (2014).
18. Sung, J. C., Pulliam, B. L. & Edwards, D. A. Nanoparticles for drug delivery to the lungs. *Trends Biotechnol.* **25**, 563–570 (2007).
19. Paranjpe, M. & Müller-Goymann, C. Nanoparticle-Mediated Pulmonary Drug Delivery: A Review. *Int. J. Mol. Sci.* **15**, 5852–5873 (2014).
20. Klinger-Strobel, M. *et al.* Aspects of pulmonary drug delivery strategies for infections in cystic fibrosis – where do we stand? *Expert Opin. Drug Deliv.* **12**, 1351–1374 (2015).
21. Taccetti, G. *et al.* Cystic Fibrosis: Recent Insights into Inhaled Antibiotic Treatment and Future Perspectives. *Antibiotics* **10**, 338 (2021).
22. Yahav, D., Farbman, L., Leibovici, L. & Paul, M. Colistin: new lessons on an old antibiotic. *Clin. Microbiol. Infect.* **18**, 18–29 (2012).
23. Montemari, A. L. *et al.* Colistin-resistant microorganisms and cystic fibrosis: microbiological surveillance in an Italian Children's Hospital. *Microbiol. Medica* **34**, (2019).
24. Bialvaei, A. Z. & Samadi Kafil, H. Colistin, mechanisms and prevalence of resistance. *Curr. Med. Res. Opin.* **31**, 707–721 (2015).
25. Pontes, J. F. & Grenha, A. Multifunctional Nanocarriers for Lung Drug Delivery. *Nanomaterials* **10**, 183 (2020).
26. Ong, V., Mei, V., Cao, L., Lee, K. & Chung, E. J. Nanomedicine for Cystic Fibrosis. *SLAS Technol. Transl. Life Sci. Innov.* **24**, 169–180 (2019).
27. Gbian, D. L. & Omri, A. Current and novel therapeutic strategies for the management of cystic fibrosis. *Expert Opin. Drug Deliv.* **18**, 535–552 (2021).

28. d'Angelo, I. *et al.* Improving the efficacy of inhaled drugs in cystic fibrosis: Challenges and emerging drug delivery strategies. *Adv. Drug Deliv. Rev.* **75**, 92–111 (2014).
29. Sans-Serramitjana, E. *et al.* Killing effect of nanoencapsulated colistin sulfate on Pseudomonas aeruginosa from cystic fibrosis patients. *J. Cyst. Fibros.* **15**, 611–618 (2016).
30. Vairo, C. *et al.* In vitro and in vivo antimicrobial activity of sodium colistimethate and amikacin-loaded nanostructured lipid carriers (NLC). *Nanomedicine Nanotechnology, Biol. Med.* **29**, 102259 (2020).
31. Pastor, M. *et al.* Sodium colistimethate loaded lipid nanocarriers for the treatment of Pseudomonas aeruginosa infections associated with cystic fibrosis. *Int. J. Pharm.* **477**, 485–494 (2014).
32. Miller, S. *et al.* Colistin-Functionalized Nanoparticles for the Rapid Capture of Acinetobacter baumannii. *J. Biomed. Nanotechnol.* **12**, 1806–1819 (2016).
33. Mei, L. *et al.* Bioconjugated nanoparticles for attachment and penetration into pathogenic bacteria. *Biomaterials* **34**, 10328–10337 (2013).
34. Scutera, S. *et al.* Enhanced Antimicrobial and Antibiofilm Effect of New Colistin-Loaded Human Albumin Nanoparticles. *Antibiotics* **10**, 57 (2021).
35. Ran, H.-H. *et al.* Colistin-Loaded Polydopamine Nanospheres Uniformly Decorated with Silver Nanodots: A Nanohybrid Platform with Improved Antibacterial and Antibiofilm Performance. *ACS Appl. Bio Mater.* **3**, 2438–2448 (2020).
36. d'Angelo, I. *et al.* Overcoming barriers in Pseudomonas aeruginosa lung infections: Engineered nanoparticles for local delivery of a cationic antimicrobial peptide. *Colloids Surfaces B Biointerfaces* **135**, 717–725 (2015).
37. Degli Esposti, L., Carella, F., Adamiano, A., Tampieri, A. & Iafisco, M. Calcium phosphate-based nanosystems for advanced targeted nanomedicine. *Drug Dev. Ind. Pharm.* **44**, 1223–1238 (2018).
38. Rodríguez-Ruiz, I. *et al.* pH-Responsive Delivery of Doxorubicin from Citrate–Apatite Nanocrystals with Tailored Carbonate Content. *Langmuir* **29**, 8213–8221 (2013).
39. Epple, M. Review of potential health risks associated with nanoscopic calcium phosphate. *Acta Biomater.* **77**, 1–14 (2018).

40. Delgado-López, J. M. *et al.* Crystallization of bioinspired citrate-functionalized nanoapatite with tailored carbonate content. *Acta Biomater.* **8**, 3491–3499 (2012).
41. Sandhöfer, B. *et al.* Synthesis and Preliminary in Vivo Evaluation of Well-Dispersed Biomimetic Nanocrystalline Apatites Labeled with Positron Emission Tomographic Imaging Agents. *ACS Appl. Mater. Interfaces* **7**, 10623–10633 (2015).
42. Uskoković, V. & Uskoković, D. P. Nanosized hydroxyapatite and other calcium phosphates: Chemistry of formation and application as drug and gene delivery agents. *J. Biomed. Mater. Res. Part B Appl. Biomater.* **96B**, 152–191 (2011).
43. Hu, Y.-Y., Rawal, A. & Schmidt-Rohr, K. Strongly bound citrate stabilizes the apatite nanocrystals in bone. *Proc. Natl. Acad. Sci.* **107**, 22425–22429 (2010).
44. Klesing, J., Wiehe, A., Gitter, B., Gräfe, S. & Epple, M. Positively charged calcium phosphate/polymer nanoparticles for photodynamic therapy. *J. Mater. Sci. Mater. Med.* **21**, 887–892 (2010).
45. Lin, J. & Wang, L. Comparison between linear and non-linear forms of pseudo-first-order and pseudo-second-order adsorption kinetic models for the removal of methylene blue by activated carbon. *Front. Environ. Sci. Eng. China* **3**, 320–324 (2009).
46. Liu, Y. & Liu, Y.-J. Biosorption isotherms, kinetics and thermodynamics. *Sep. Purif. Technol.* **61**, 229–242 (2008).
47. Kirchner, S. *et al.* Use of Artificial Sputum Medium to Test Antibiotic Efficacy Against Pseudomonas aeruginosa in Conditions More Relevant to the Cystic Fibrosis Lung. *J. Vis. Exp.* (2012) doi:10.3791/3857.
48. Jeukens, J. *et al.* Complete Genome Sequence of Persistent Cystic Fibrosis Isolate Pseudomonas aeruginosa Strain RP73. *Genome Announc.* **1**, (2013).
49. European Committee on Antimicrobial Susceptibility Testing. ISO 20776-1: 2019: Susceptibility testing of infectious agents and evaluation of performance of antimicrobial susceptibility test devices Part 1: Broth microdilution reference method for testing the in vitro activity of antimicrobial agents against rapidl. *Int. Organ. Stand.* (2019).
50. Sen Gupta, S. & Bhattacharyya, K. G. Kinetics of adsorption of metal ions on inorganic materials: A review. *Adv. Colloid Interface Sci.* **162**, 39–58 (2011).
51. Cazalbou, S., Bertrand, G. & Drouet, C. Tetracycline-Loaded Biomimetic Apatite: An

Adsorption Study. *J. Phys. Chem. B* **119**, 3014–3024 (2015).

52. Benedini, L., Placente, D., Ruso, J. & Messina, P. Adsorption/desorption study of antibiotic and anti-inflammatory drugs onto bioactive hydroxyapatite nano-rods. *Mater. Sci. Eng. C* **99**, 180–190 (2019).
53. Souza, C. A. S. de *et al.* Adsorption of chlorhexidine on synthetic hydroxyapatite and in vitro biological activity. *Colloids Surfaces B Biointerfaces* **87**, 310–318 (2011).
54. OKADA, M., HIRAMATSU, D., OKIHARA, T. & MATSUMOTO, T. Adsorption and desorption behaviors of cetylpyridinium chloride on hydroxyapatite nanoparticles with different morphologies. *Dent. Mater. J.* **35**, 651–658 (2016).
55. Cone, R. A. Barrier properties of mucus. *Adv. Drug Deliv. Rev.* **61**, 75–85 (2009).
56. Ungaro, F. *et al.* Dry powders based on PLGA nanoparticles for pulmonary delivery of antibiotics: Modulation of encapsulation efficiency, release rate and lung deposition pattern by hydrophilic polymers. *J. Control. Release* **157**, 149–159 (2012).
57. Sanders, N. N. *et al.* Cystic Fibrosis Sputum: A Barrier to the Transport of Nanospheres. *Am. J. Respir. Crit. Care Med.* **162**, 1905–1911 (2000).
58. Freudenthal, O. *et al.* Nanoscale investigation of the interaction of colistin with model phospholipid membranes by Langmuir technique, and combined infrared and force spectroscopies. *Biochim. Biophys. Acta - Biomembr.* **1858**, 2592–2602 (2016).
59. Li, Y. *et al.* Preparation and characterisation of the colistin-entrapped liposome driven by electrostatic interaction for intravenous administration. *J. Microencapsul.* **33**, 427–437 (2016).
60. Ichim, D. L. *et al.* Synthesis and Characterization of Colistin Loaded Nanoparticles Used to Combat Multi-drug Resistant Microorganisms. *Rev. Chim.* **70**, 3734–3737 (2019).
61. Aljayyoussi, G., Abdulkareem, M., Griffiths, P. & Gumbleton, M. Pharmaceutical nanoparticles and the mucin biopolymer barrier. *Bioimpacts* **2**, 173–174 (2012).
62. Di Mauro, V. *et al.* Bioinspired negatively charged calcium phosphate nanocarriers for cardiac delivery of MicroRNAs. *Nanomedicine* **11**, 891–906 (2016).

4. CaP scaffolds from natural sources for bone regeneration application

4.1. Introduction

The second biomedical material that will be treated in this thesis consists in a 3D porous scaffold developed for the hard tissue engineering or bone regeneration.

The tissue engineering was defined by Furth et al. as the combination between materials and cell transplantation in order to develop substitute tissues and/or promote endogenous regeneration.[1] In particular, bone tissue is characterized by a remarkable regenerative potential. On the other hand, the healing process is impossible to standardize for each type of bone because of their highly dynamicity and their capability to respond to different mechanical stimuli.[2–5] For these reasons, it is necessary to design, develop and provide substitute biomaterials which can reproduce the osteogenic properties of bone grafts. Meanwhile, these biomaterials could bypass the well-known disadvantages associated with common prostheses, such as limited availability and requirement for secondary surgery. A challenging feature that biomaterials should have, consists in maintenance of its shape stability during the healing/regeneration process.[2,5] In this way it is possible to promote the formation of bone volume, without losing the bridging effect between bone margins. The biomaterials which have shown these characteristics and that could be used in bone tissue regeneration are (i) injectable materials that resemble the bone extracellular matrix, (ii) the use of scaffolds that mimic the bone mechanical support, or (iii) a combination the two previous approaches.[2,4,5]

Among these materials, the development of porous scaffold will be treated in this chapter. It is worth to mention that these scaffolds should be not only biocompatible, structurally similar to bone, resorbable, osteoconductive or osteoinductive, but it also must be characterized by an optimized porosity.[6–8] Indeed, the porosity is involved in the scaffold capability to support cell adhesion, migration and proliferation, and oxygen flows.[7,9,10] The macroporous size distribution to achieve optimal cellular growth is still subject to intense debate, but it is knew that an increase in pore size can enhance the permeability and the new bone ingrowth. On the other hand, the soft tissue ingrowth

Part of the content of this chapter has been published in Marine Drugs 2020, 18 (6), 309 as “Scialla S., Carella F., et al. Mussel Shell-Derived Macroporous 3D Scaffold: Characterization and Optimization Study of a Bioceramic from the Circular Economy”

could be more influenced by the presence of small pores.[7] Several evidence have shown that macroporosity with a diameter between 100 and 500 µm favour cell proliferation, osteointegration and angiogenesis.[7,8,11] Moreover, the presence of small and interconnected pores (0.1 – 1.0 µm) seems to promote the chondrogenesis.[8,12]

Among methods that are used to manufacture 3D bioceramic scaffolds,[13–16] the direct foaming technique is considered particularly promising. With this preparation method, it is possible to obtain a porous 3D scaffold with specific pore size and structure, without using any sacrificial template.[17] The pore formation is achieved through the incorporation of a gas (usually air) in a ceramic suspension/slurry. Furthermore, the suspension is poured, dried, and sintered.[18] The total porosity volume (from 40 to 97%) and the pore size (from 10µm to 1mm) are linked with the amount of gas incorporated into the slurry and the stability of the slurry itself before drying, respectively.[7] These characteristics can be tailored using appropriate surfactant(s) and/or foaming agent(s).

A class of materials that could be ideal for the preparation of 3D porous scaffolds for bone tissue engineering are CaP because of their chemical similarity to the bone mineral phase. This minimizes the chances of post-operative rejection of the implanted material.[19] Among others, a possible method for the preparation of HA consists in the reaction between $CaCO_3$ and a phosphorus source. $CaCO_3$ represents the main component of shells, which are one of the most abundant by-products produced by fish industries. As previously described, in literature there are few works in which these raw materials are employed to prepare HA-based materials.[20–23] On the other hand, these works are commonly limited to the synthesis of HA powder, and none of them report the preparation of 3D structures. The review written by Diaz-Rodriguez et al. is one of the few works that reports the 3D structures based on CaP from natural source. In particular, Diaz-Rodriguez states that the use of natural source as animal discards or fishing by-products, to prepare CaP has gained increased attention.[6] Indeed, there is a growing interest in the development of bioceramic structures which can provide a good porosity and an optimal balance between stability and resorbability in order to ensure bone regeneration.

For these reasons, a low economic and environmental impact process to produce 3D macroporous scaffold for biomedical application was performed and reported in this

chapter. Mussel shells were chosen as a natural $CaCO_3$ source and, therefore, as a precursor of HA powder. HA powder was employed to prepare porous scaffolds using an already reported direct foaming method.[24] Finally, both powders and 3D structures were characterized, and the mechanical properties of the scaffolds were also investigated.

4.2. Materials and methods

4.3. Chemicals

Mussel shells (from Mytilus edulis) were furnished by a local fishing company (Lepore Mare SpA, Fasano (BR), Italy). Ammonium phosphate dibasic ($(NH_4)_2HPO_4$, ≥98%), phosphoric acid (H_3PO_4 85% w/w), and ammonium hydroxide (NH_4OH 30% v/v) used for the synthesis of HA were purchased from Sigma–Aldrich (Milan, Italy). Dolapix CA (Zschimmer and Schwartz, Lahnstein, Germany), Olimpicon A (Olimpia Tensioattivi, Cavenago Brianza (MB), Italy), W53 (Zschimmer and Schwartz, Lahnstein, Germany) were used for the scaffold preparation. Finally, ultrapure water (18.2 MΩ/cm) was used to prepare solutions or suspensions.

4.3.1. Calcium oxide (CaO) extraction

The extraction of CaO from mussel shells, which are considered as $CaCO_3$ source, was performed by heating the samples in a muffle furnace (mod. ZA (Prederi Vittorio & Figli, Milan, Italy). Before they were transformed into CaO, waste mussel shells were manually cleaned with hot water, dried overnight at 80°C, and then mechanically crushed. Thermal treatments were executed by fixing a heating rate of 5 °C/min and a swell time of 1 h, but some parameters such as temperature (700 or 1000 °C) and atmosphere (air or in N_2), were changed. In Table 4.1 were reported every sample obtained from the thermal treatment that have been performed combining different temperature and atmosphere, during this thesis:

Table 4.1 – Thermal treatment performed at different temperature and atmosphere to produce CaO from mussel shells

Sample name	Atmosphere	Temperature (°C)
S_A_700	Air	700
S_A_1000	Air	1000

S_N_700	N_2	700
S_N_1000	N_2	1000

Eventually, powders obtained were manually milled, and mechanically sieved (Retsch GmbH, Haan, Germany) under 125 µm mesh size.

4.3.2. Synthesis of HA

The synthesis of HA was performed through a neutralization reaction between CaO powders obtained by thermal treated in air atmosphere (S_A_700 and S_A_1000), and two different phosphorus sources ($(NH_4)_2HPO_4$[25] or H_3PO_4[26]) accordingly to the reactions showed in Equations (4.1) and (4.2), respectively:

$$10\ Ca(OH)_2 + 6(NH_4)_2HPO_4 \rightarrow Ca_{10}(PO_4)_6\ (OH)_2 + 6H_2O + 12NH_4OH \quad \text{(Equation 4.1)}$$

$$10\ Ca(OH)_2 + 6H_3PO_4 \rightarrow Ca_{10}(PO_4)_6\ (OH)_2 + 18H_2O \quad \text{(Equation 4.2)}$$

In detail, 2 g of CaO based powder was dispersed in 35 mL of ultrapure water, causing the complete transformation of CaO into calcium hydroxide ($Ca(OH)_2$) (1 M). Subsequently, 35 mL of $(NH_4)_2HPO_4$ or H_3PO_4 aqueous solution (0.6 M) was slowly dropped and, in the case of the latter source of phosphorous, the pH of the reaction was adjusted to 9.0 by adding NaOH. Finally, the temperature and the incubation time were set at 80 °C and 16 h, respectively. The obtained powders were then filtered, washed several times with ultrapure water by centrifugation at 4000 rpm for 15 min and freeze-dried overnight. The preparation of HA powders was completely described and reported in the Table 4.2.

Table 4.2 – List of HA powders obtained through a neutralization synthesis between $Ca(OH)_2$ and two different sources of phosphorous.

Sample name	Ca containing reagent	P containing reagent
HA_1	S_A_700	$(NH_4)_2HPO_4$
HA_2	S_A_700	H_3PO_4
HA_3	S_A_1000	$(NH_4)_2HPO_4$
HA_4	S_A_1000	H_3PO_4

Furthermore, the reaction for the preparation of HA_1 was carried out increasing the volume to obtain more powder. In particular, 420g of S_A_700 were suspended in 7.5L of ultrapure water, then 7.5L of $(NH_4)_2HPO_4$ solution (0.6M) was added dropwise. The

synthesis conditions and the purification of the material was conducted as previous described. The obtained HA powder was called HA_5.

4.3.3. Preparation of the 3D Scaffolds

The production of macroporous scaffolds, accordingly with a reported foaming process,[27] has foreseen a thermal pre-treatment of the CaP powdered sample that was used for this process. The HA_5 was, thus, calcined at 1000°C for 1 h and sieved under 150 µm, obtaining the sample HA_6. As a reference sample, scaffolds based on commercial HA powders (Sigma–Aldrich, Milan, Italy) were also prepared. Briefly, both powders (HA_6 and commercial HA) were dispersed in water with Dolapix CA, according to the weight ratio HA:H_2O:Dolapix = 73:23:4. Then, 2 wt.% of Olimpicon A and 0.7 wt.% of W53 were added as foaming agents. Finally, the foamed suspensions were poured into laboratory filter paper (weight 60 g m^{-2}, thickness 0,13 mm) moulds, dried at 25 °C for 24 h, and sintered at 1250°C for 1 h. The schematic representation of the process is reported in Figure 4.1.

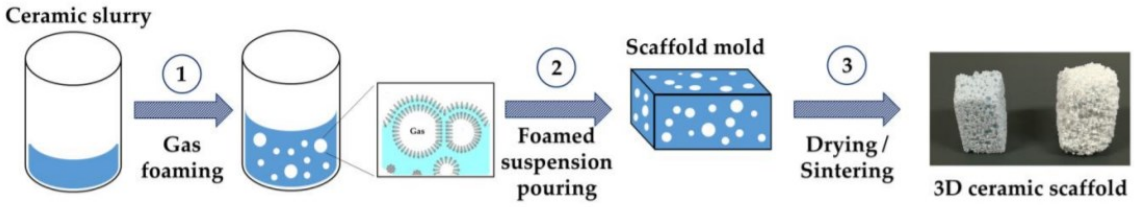

Figure 4.1 - Schematic representation of the direct foaming method to prepare a 3D ceramic scaffold.

4.3.4. Mechanical properties

Initially, the total porosity volume, which is related to the amount of gas bubbles incorporated during the foaming process, was evaluated. The scaffold porosity is a property that affects the bioactivity of the material and its mechanical performances.[7] In this thesis, the porosity of the structure was evaluated following the Equation 4.3:

$$\Phi = 1 - {}^{\delta_c}/_{\delta_s} \qquad \text{(Equation 4.3)}$$

In which δc/δs represents the relative density of the scaffolds. It is determined by the ratio between the density of the material calculated as weight-on-volume ratio (δc) and

the theoretical density of the phase, determined considering the composition calculated by XRD data (δs). Moreover, the strength of obtained scaffolds was determined by the compressive test. The tensile stress is not used due to the intrinsic micron-size defects that can be easily extended, affecting the measurement. A compressive test involves a system of converging forces which tends to reduce its size. Ideally, the forces are homogeneously distributed on the whole surface of the sample sections. Therefore, the average value of the compressive stress (σ) can be obtained by dividing the force (F) with the cross-sectional area (A).[28]

In this thesis, the compressive strength was determined by testing 10 parallelepiped specimens (base = 9 × 9 mm, height = 18 mm). The tests were performed in displacement control at 0.5 mm min^{-1} with a universal testing machine (Zwick/Roell Z050, Ulm, Germany). Young's modulus was calculated as the slope of the stress–strain curves in the elastic region. The strain energy or toughness, defined as the energy required to fracture the specimen, was also calculated by measuring the area underneath the compressive stress–strain curve.

4.4. Results and discussion

4.4.1. Preparation and characterization of CaO Samples

Initially, the characterization of raw mussel shells was conducted by XRD, TGA and ICP-OES. XRD pattern of these materials is shown in Figure 4.2a, in which the peaks were indexed as calcium carbonate ($CaCO_3$) polymorphic phases (calcite and aragonite). The relative quantification of these phases was carried out by Rietveld refinement that evinced their amount as 70 wt.% and 30 wt.%, respectively. The Figure 4.2 display also the TGA curve of raw mussel shells (b) which confirm the presence of $CaCO_3$. Indeed, the curve highlights two main weight losses, the first (4%) in the range 250–600°C attributed to the removal of organic matter and adsorbed water, and the second (42%) in the range 670–900°C attributed to the decarbonization of $CaCO_3$.[27,29]

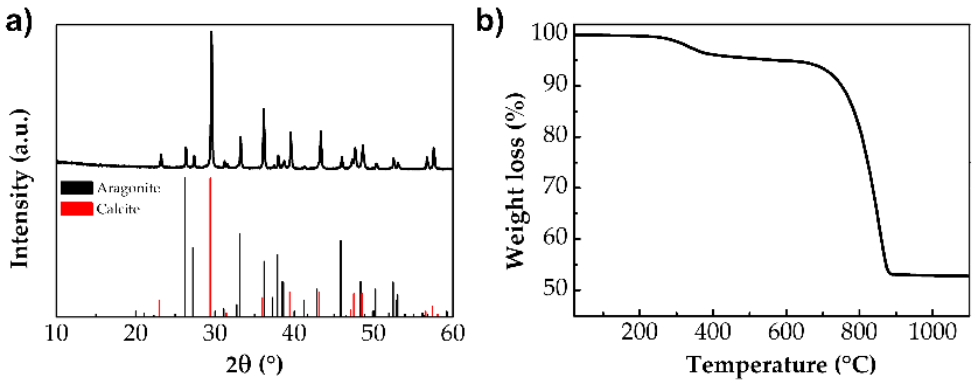

Figure 4.2 - (a) XRD pattern and (b) TGA curve of raw mussel shells. In panel (a) the reference pattern of calcite (#05-0586) and aragonite (#041-1475) are also showed.

Furthermore, a multi-elemental analysis of the material was conducted by ICP-OES. In Table 4.3 are revealed and quantified the most abundant elements detected (Ca, Mg, P, Na, Se, and Sr), while the other 15 elements were below their detection limit. In particular, the limit of detection (LOD) in the sample of As, B, Be, P, Pb, Se was 1 ppm, while LOD of Al, Ba, Ca, Cd, Co, Cu, Cr, Fe, Mg, Mn, Na, Ni, Sr, V, Zn was 0,05ppm

Table 4.3 – Elemental composition of the raw mussel shells.

Ca (wt.%)	Mg (wt.%)	Na (wt.%)	P (wt.%)	Se (wt.%)	Sr (wt.%)
34,6 ± 0,7	0,11 ± 0,01	0,55 ± 0,04	0,46 ± 0,04	0,16 ± 0,21	0,09 ± 0,01

Two different temperatures (700 or 1000 °C) were chosen for the thermal transformation of mussel shells in CaO. The lowest value selected represents the minimum temperature essential to ensure the complete removal of the organic fractions from the shell which is generally up to 5 wt.%.[27] On the other hand, the highest temperature was considered to achieve the complete decomposition of carbonates.[29] Moreover, the comparison between the effect of gaseous atmosphere (N_2 or air) on composition and SSA of the samples, was performed. The powdered samples obtained from these combinations of thermal treatment and gaseous atmosphere are so-called S_A_700, S_A_1000, S_N_700 and S_N_1000. XRD patterns of these four CaO samples and CaO (#37-1497), $CaCO_3$ (#05-0586) and $Ca(OH)_2$ (#04-0733) standards are shown in Figure 4.3.

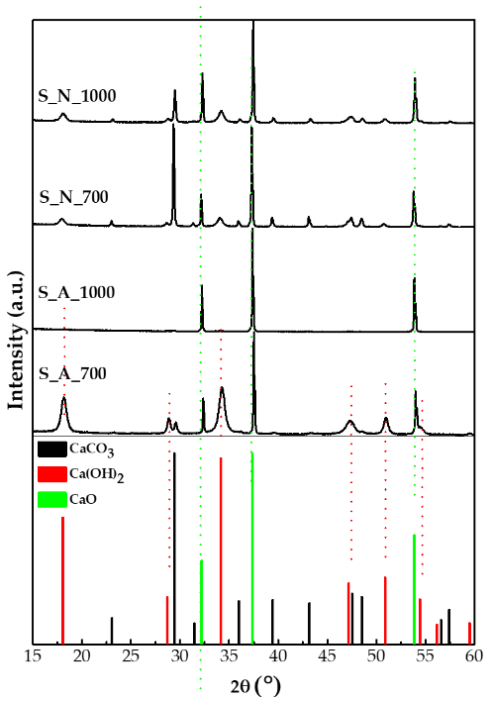

Figure 4.3 –XRD patterns of the CaO samples and CaO, $CaCO_3$ and $Ca(OH)_2$ reference patterns.

The XRD pattern of S_A_700 showed sharp and intense peaks at 37.35° and 53.85° which are related to (200) and (220) planes, respectively. These peaks belong to CaO as a result of the decarboxylation of $CaCO_3$ happened during the thermal treatment. Moreover, a small amount of $CaCO_3$ was still detectable in the diffraction pattern (29.41°, (104)), indicating the non-complete carbonate decomposition. Finally, larger and less defined peaks at 18.06° and 34.14°, belonging to (001) and (101) planes of $Ca(OH)_2$, respectively, are ascribable to the reaction between CaO and the atmospheric moisture. The XRD pattern of S_A_1000, instead, shows the CaO phase as the only phase present.

Regarding XRD pattern of samples thermal treated under N_2 atmosphere (S_N_700 and S_N_1000), the peaks attributed to CaO and $CaCO_3$ showed similar intensities. This indicates that the decarboxylation takes place at a lower extent in an inert atmosphere in comparison to the treatment in air. $Ca(OH)_2$ traces were also detected in both samples, but at a lower proportion than the ones treated in air. Finally, in S_N_1000 sample, a decrease in the $CaCO_3$ peaks took place, indicating a more enhanced and incomplete decarboxylation. The phase composition evaluated through Rietveld refinement and the quantification of the SSA are reported in Table 4.4.

Table 4.4 - CaO samples derived from the mussel shells prepared with different treatments. Corresponding phase composition (wt.%) and surface area ($m^2 g^{-1}$) are reported.

Sample name	Phase Composition (wt.%)			SSA ($m^2 g^{-1}$)
	CaO	$Ca(OH)_2$	$CaCO_3$	
S_A_700	19,0 ± 0,3	70,1 ± 0,4	10,9 ± 0,4	5,6
S_A_1000	100	-	-	3,1
S_N_700	32,0 ± 0,3	17,8 ± 0,4	50,2 ± 0,4	2,5
S_N_1000	43,9 ± 0,3	27,6 ± 0,3	28,6 ± 0,4	6,6

These variation in the composition of the samples prepared by using N_2 or air atmospheres can be explained considering the different mechanisms and shells' decomposition kinetics. Indeed, it is reported in literature that the organic carbon is converted into inorganic graphitic-like carbon in an inert atmosphere.[30] Moreover, the atmosphere gas could affect the capability of the carbon dioxide to diffuse through the porous structure of the mussel shells.[31] Such diffusion is higher in air than in N_2 and could lead to an increase in decarboxylation extent.

Regarding the values of the SSA also reported in Table 4.4, it is possible to observe that the SSA slightly decreased by increasing temperature for the samples treated in air. On the other hand, an opposite trend was observed for the ones treated with N_2. Comparing the samples prepared in air with those prepared in N_2, the inert atmosphere showed to be less suitable for the conversion process of $CaCO_3$ in CaO, as led to powders with a relatively high content of $CaCO_3$. For this reason, the treatment in N_2 was not considered further in this study. Moreover, it is also worth noting that environmental and economic sustainability always has to be considered when working with by-product valorisation in a circular economy approach.[32] In this context, the use of air was also preferred with the aim of developing the simplest process, with the lowest cost and impact on the environment. Furthermore, similarly to the raw mussel shells, a multi-elemental analysis of the CaO material was conducted by ICP-OES and the most abundant elements detected are reported in Table 4.5.

Table 4.5 – Elemental composition of the raw mussel shells.

Sample	Ca (wt.%)	Mg (wt.%)	Na (wt.%)	P (wt.%)	Se (wt.%)	Sr (wt.%)
S_A_700	42,8 ± 1,9	0,09 ± 0,01	0,29 ± 0,03	0,04 ± 0,03	0,71 ± 0,23	0,10 ± 0,01

S_A_1000	48,3 ± 0,4	0,10 ± 0,01	0,16 ± 0,01	0,05 ± 0,01	0,59 ± 0,34	0,11 ± 0,01
S_N_700	40,7 ± 3,7	0,14 ± 0,01	0,39 ± 0,10	0,17 ± 0,06	0,49 ± 0,15	0,11 ± 0,01
S_N_1000	44,0 ± 0,9	0,12 ± 0,01	0,20 ± 0,03	0,02 ± 0,01	0,37 ± 0,22	0,11 ± 0,01

The other 15 elements, which are not showed in the Table 4.5, were below their detection limit. The LOD of each element in the sample are previous described. In agreement with the phase composition, S_A_1000 had a slightly higher content of Ca respect to the other samples. In addition, to evaluate the morphology of the CaO powders SEM analyses were performed and the images are reported in Figure 4.4.

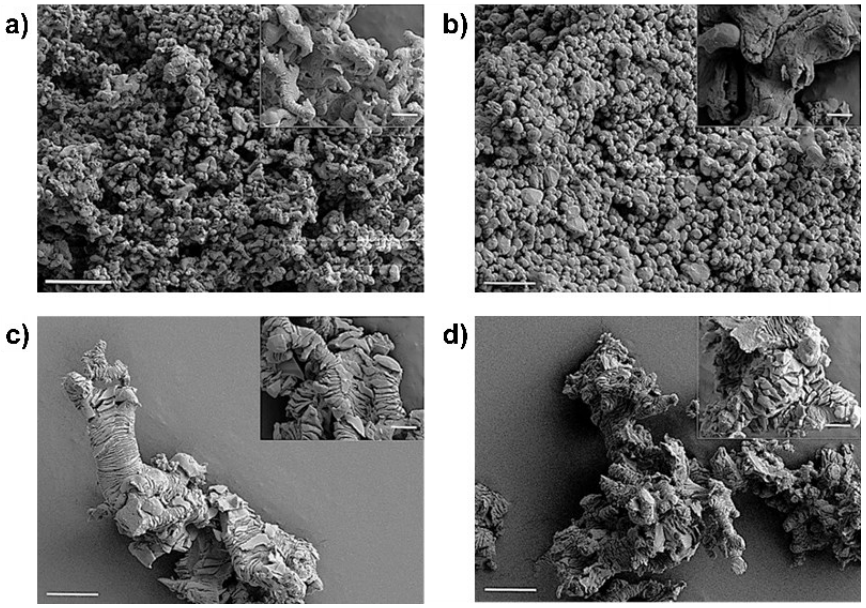

Figure 4.4 - SEM images of CaO samples: (a) S_A_700, (b) S_A_1000, (c) S_N_700, (d) S_N_1000 [main images: magnification 5kX, scale bar 10 µm; insert: magnification 25 kX, scale bar 1 µm]

S_A_700 (Figure 4.4a) shows rounded shaped structures and aggregates with dimensions up to micron scale, while treating the sample at higher temperatures (S_A_1000, Figure 4.4b), structures become larger. On the other hand, the Figure 4.4c,d display SEM images of samples treated in N_2, which show different morphology. In particular, the surface of both samples, highlight smaller lamellae-like features with some cracks between them (visible at higher magnification).

4.4.2. Preparation and Characterization of HA Samples

CaO based samples (S_A_700 and S_A_1000) were used to prepare HA with two different protocols (Section 5.3.3), obtaining HA_1, HA_2, HA_3 and HA_4. These materials were

firstly characterized by XRD and TEM (Figure 4.5), then, ICP and BET analyses were also conducted.

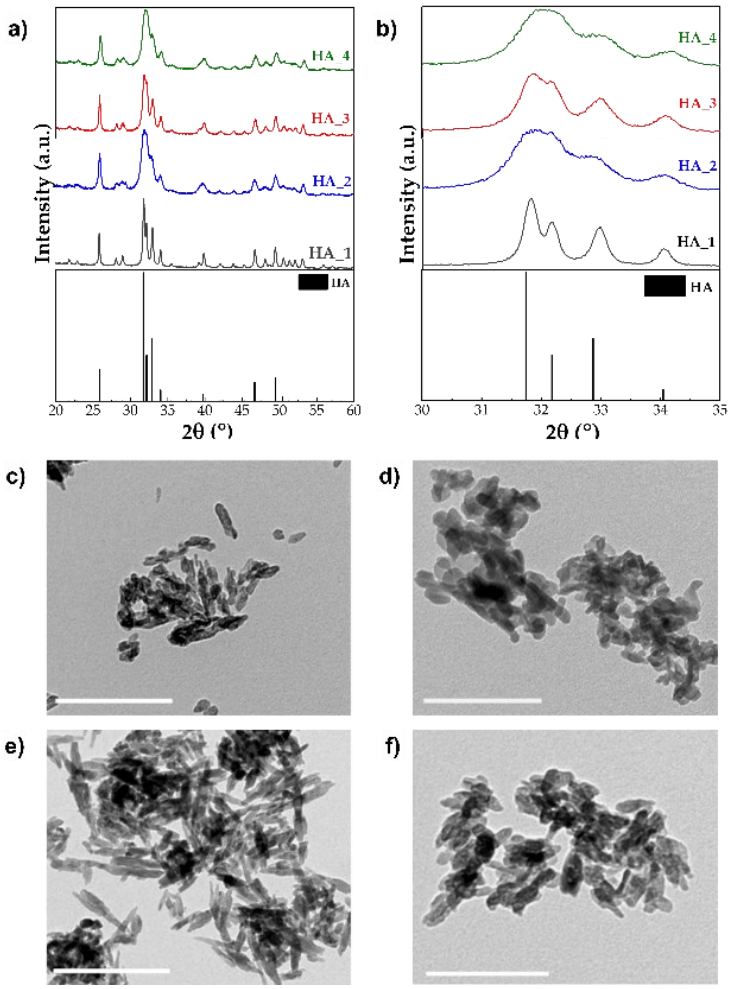

Figure 4.5 - (a) XRD pattern of HA samples and HA standard (#09-0432) and (b) its enlargement of the 30–35° (2θ) range; (c–f) TEM micrographs of HA_1, HA_2, HA_3, and HA_4, respectively. [Scale bar 200 nm]

XRD pattern shows that HA is present as the single crystalline phase in all synthesis, except for HA_2 in which there are traces of calcite (1 wt.%) as residual unreacted starting material. More specifically, in XRD pattern of HA_1 and HA_3 (powders obtained with $(NH_4)_2HPO_4$ as phosphorous source) the signals at 31.7 and 32.2° were clearly distinct and separate, indicating a higher crystallinity than the other two materials. Indeed, in HA_2 and HA_4 (powders obtained with H_3PO_4 as phosphorous source) XRD pattern the two peaks were overlapped into a single broad one indicating a very low crystallinity degree. The main difference between HA powders can be observed in their crystallinity. Indeed, samples prepared with $(NH_4)_2HPO_4$ were more crystalline than those prepared with H_3PO_4. This can be explained considering the different reaction of HA formation (see

Equations (4.1) and (4.2)). In particular, the pH value measured when HA nucleation occurs in the reaction with $(NH_4)_2HPO_4$ (pH = 9) is higher than the one measured in the reaction that involves H_3PO_4. In the latter neutralization reaction, the initial pH is equal to 9, but slowly decreases to 7 during the H_3PO_4 dropping. For this reason, the nucleation occurs at neutral or slightly acid condition obtaining a less crystalline HA than that obtained at basic pH. Moreover, Scherrer's equation (Equation 4.4) was used to estimate the average size of crystal domains along *c*-axis ($D_{(002)}$) and *a–b* plane (orthogonal to the *c*-axis, $D_{(310)}$).

$$D_{[hkl]} = \frac{0{,}9\lambda}{cos\theta\sqrt{(\Delta_r^2)-(\Delta_0^2)}} \qquad \text{(Equation 4.4)}$$

In Scherrer's equation θ represents the diffraction angle for the plane (hkl), Δ_r and Δ_0 are the widths in radians of the reflection (hkl) at half height for the synthesized and pure inorganic hydroxyapatite (standard reference material, calcium hydroxyapatite, National Institute of Standards and Technology), respectively, and λ = 1.5405 Å. In particular, the calculation was carried out using the width at half height for the respective reflections (002) and non-overlapped (310) and the results are reported in Table 4.6.

Table 4.6 - Crystal domains' average size along c-axis ($D_{(002)}$) and a–b plane ($D_{(310)}$) of HA samples

Sample name	$D_{(002)}$ (nm)	$D_{(310)}$ (nm)	$D_{(002)}/D_{(310)}$
HA_1	108,7 ± 1,5	55,2 ± 0,6	2,0
HA_2	33,8 ± 0,5	11,9 ± 0,1	2,8
HA_3	70,3 ± 0,6	21,0 ± 0,2	3,4
HA_4	30,2 ± 0,5	12,0 ± 0,2	2,5

The outcomes show that $D_{(002)}$ and $D_{(310)}$ of HA_1 and HA_3 were both higher than the corresponding crystal domains of HA_2 and HA_4. These data also revealed that all the crystals were elongated along the *c*-axis with HA_3 having the maximum aspect ratio, estimated as $D_{(002)}/D_{(310)}$. Finally, the morphological characteristics of the materials was observed with TEM images showed in Figure 4.5 showing correspondence with the crystal domains' size previous discussed. In particular, HA_3 (Figure 4.5e) is constituted by needle-like nanoparticles with an elongated shape of about 100 nm. On the other hand, HA_1, HA_2, and HA_4 (Figure 4.5c-f, respectively), are constituted by plate

nanoparticles. The crystal domains' size results are in correlation with the values of SSA reported in Table 4.7. Indeed, HA_1 show a higher crystal domains' size, but a low value of SSA. On the other hand, smaller crystal domains' size led to an increase of SSA value, especially for samples HA_2 and HA_4 (about 90–100 $m^2 g^{-1}$).

Table 4.7 – Ca/P molar ratio and SSA ($m^2 g^{-1}$) of HA samples prepared from calcined mussel shells.

Sample name	Specific surface area ($m^2 g^{-1}$)	Ca/P ratio (mol mol^{-1})
HA_1	49,6	1,88 ± 0,01
HA_2	100,9	1,73 ± 0,01
HA_3	83,5	1,84 ± 0,01
HA_4	93,1	1,73 ± 0,01

Moreover, Table 4.7 shows the Ca/P ratio calculated by ICP-OES analysis of the samples. In all powders, this parameter was slightly higher than the stoichiometric one (i.e., 1.67). In particular, it was around 1.73 for the powders prepared with H_3PO_4 and 1.88 for those with $(NH_4)_2HPO_4$.

The tailoring characteristics of HA samples by selecting the appropriate mussel shells' derived materials and/or the reaction conditions, lead to powders which can be used for different application. For example, HA_4 is characterized by high SSA that more suitable in environmental remediation or drug delivery application.[33,34] On the other hand, to make 3D scaffolds as requested in this chapter of the thesis, the interactions between the particles must be taken into account. Therefore, for some protocols, the use of powders with high SSA may not lead to good results.[35] Among all the HA samples obtained, sample HA_1 was chosen as the most suitable, having the lowest SSA comparable to HA-based materials that were previously used for preparing 3D scaffolds by direct foaming technique.[24]

Therefore, to increase the yield of HA_1 its synthesis conditions were scaled up by 100 times, as described in Section 5.3.3, obtaining sample HA_5. The relative phase quantification carried out by Rietveld refinement on HA_5 XRD patter revealed that the powder was entirely constituted by HA with a very low content of calcite (< 0,5 wt.%). Moreover, the increase of SSA value of HA_5 (63,8 $m^2 g^{-1}$) respect to the one obtained from the HA_1 analysis (49,6 $m^2 g^{-1}$) was coherent with the decreasing trend observed

for the crystal domains' size ($D_{(002)}$ and $D_{(310)}$) , showed in Table 4.8. Indeed, as the material becomes nanostructured, the surface area is increasing.

Table 4.8 - Comparation between crystal domains' size of HA_1 and HA_5

Sample name	$D_{(002)}$ (nm)	$D_{(310)}$ (nm)	$D_{(002)}/D_{(310)}$
HA_1	108,7 ± 1,5	55,2 ± 0,6	2,0
HA_5	80,7 ± 0,7	30,6 ± 0,1	2,6

The SEM image of sample HA_5, reported in Figure 4.6b, shows the presence of rounded granules, smaller than 100 nm. The sample is morphologically similar to HA_1 (Figure 4.6a), confirming that the HA main characteristics are retained even upon the scaling-up process.

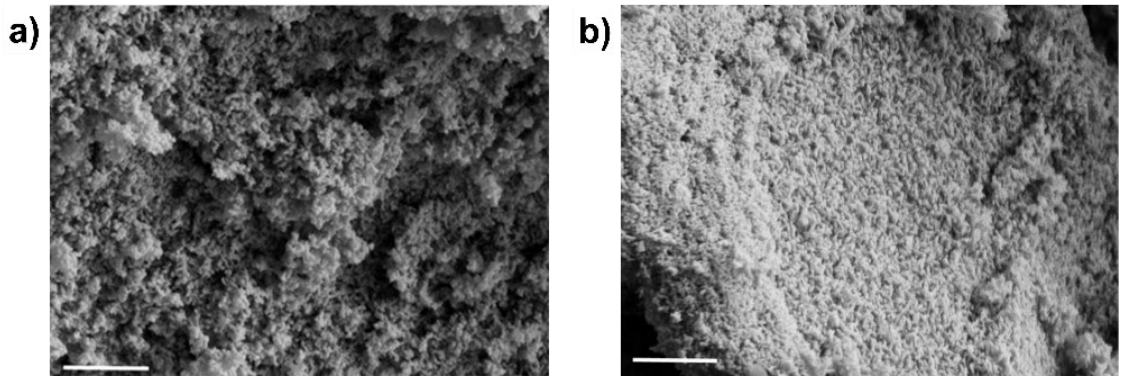

Figure 4.6 - SEM images of HA_1 (a) and HA_5 (b) [scale bar 1 µm]

4.4.3. Preparation and Characterization of the 3D Scaffolds

The methodology employed for the macroporous 3D scaffolds preparation was based on a patented process with a crucial modification.[36] In particular, the use of high-energy planetary ball milling allowed to shorten the process time significantly.[24] Previously, the calcination at 1000°C for 1h on both HA_5 sample (hereafter labelled as HA_6) and commercial HA powder used as a reference was performed. This process was done in order to further lower SSA and to prevent the formation of agglomerates in the ceramic suspension (slurry).[24] The obtained materials (HA_6 and commercial HA) showed comparable SSA equal to 4,5 $m^2 g^{-1}$and 5,1 $m^2 g^{-1}$, respectively. The lower surface area of HA_6 than HA_5 was due to the coalescence of the primary particles after thermal

activation. Furthermore, XRD pattern (Figure 4.7) reported a little difference in composition between the two materials.

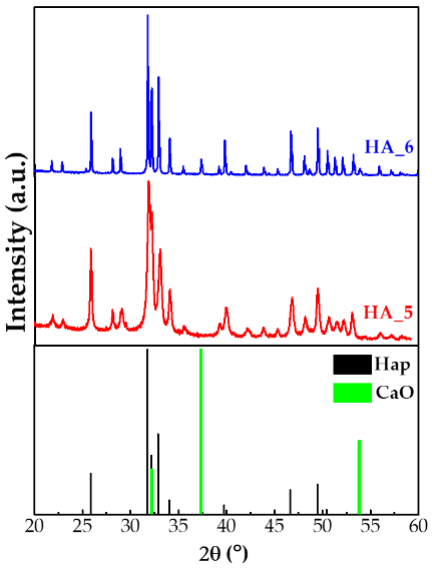

Figure 4.7 - XRD patterns of HA_5, HA_6 samples, HA (#09-0432) and CaO (#37-1497) standards.

Commercial HA is entirely formed by HA, while HA_6 highlights about 4.0 wt.% of CaO phase in the powder. The formation of this phase is probably due to the removal of the calcium ions excess from the crystal lattice. Indeed, Ca/P molar ratio of HA_5 (1.83 ± 0.01) is higher than the stoichiometric one (1.67) due to a surplus of Ca^{2+} ions in its structure and its non-stoichiometric nature. HA thermal decomposition to form CaO after high-temperature treatments was previously reported in the literature.[37,38] Furthermore, HA_6 XRD pattern (Figure 4.7) shows a considerable increase in crystallinity highlighted by the presence of intense and highly resolved diffraction peaks. These data clearly indicate that the HA obtained from natural source (HA_6) could be an interesting material similar to the synthetic one in order to achieve scaffolds for biomedical purposes.

Additionally, to assess the powders stability in contact with the dispersant agent used for the scaffold preparation (Dolapix), the distribution of the particle size was measured before and after the calcination with DLS (Figure 4.8).

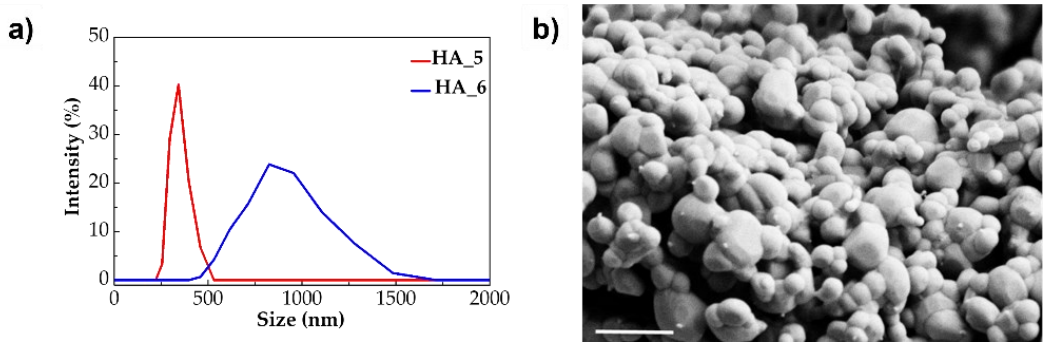

Figure 4.8 – (a) Size distribution of HA_5 and HA_6 samples suspended in Dolapix 4 wt.%, and (b) SEM image of HA_6 [scale bar 1 µm]

In Figure 4.8a is possible to notice that HA_5 has a particle size distribution in the range from 200 to 500 nm, while HA_6 shows a broader particle distribution ranging from 500 and 1500 nm, also confirmed by SEM images (Figure 4.8b). Moreover, ξ-potential values were −40 ± 5 mV and −30 ± 03 mV for HA_5 and HA_6, respectively. These results highlighted a significant stability for both HA suspensions analysed.[39,40]

Afterwards the preparation of the powdered materials, the scaffolds were produced via direct foaming and successively sintering. In particular, the foamed suspensions were poured into laboratory filter paper moulds and kept motionless at 25°C for 24h. These conditions ensure a slow drying process in order to prevent the generation of cracks or flaws in the scaffold.

Initially, the crystal phase composition of the two obtained scaffolds was investigated by XRD. The scaffolds composition has proven to be very similar to the crystal phase composition of precursor powders. Subsequently, the two systems were morphologically analysed with SEM microscopy in order to evaluate the porosity of the scaffold (Figure 4.9).

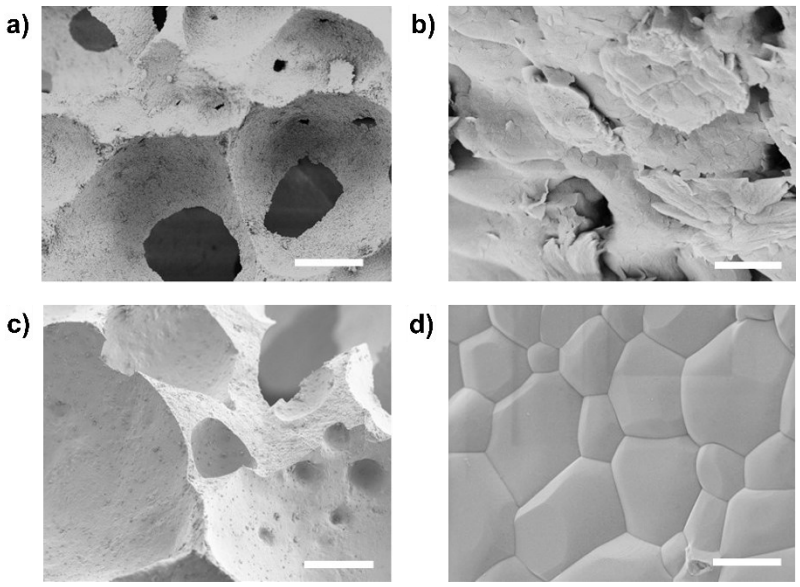

Figure 4.9 - SEM images of scaffolds prepared with HA_6 (a,b) and commercial HA (c,d). [Scale bar: (a,c) 100 µm; (b,d) 1 µm]

SEM images reported in Figure 4.9 showed that the main difference between the two scaffolds consist in the higher degree of consolidation of the commercial HA scaffold respect the HA_6 scaffold. On the other hand, SEM images of both samples highlight a highly porous structure (estimated in the range 87 – 89%) with an open and interconnected micro- and macro-porosity in the range of 50 – 300 µm. This characteristic ensures the scaffolds to be suitable to support not only infiltration, migration, and proliferation of cells, but also a good perfusion of physiological fluids.[41]

Furthermore, the mechanical performances of porous structures were evaluated through the quantification of the compressive strength of the scaffolds (Figure 4.10).

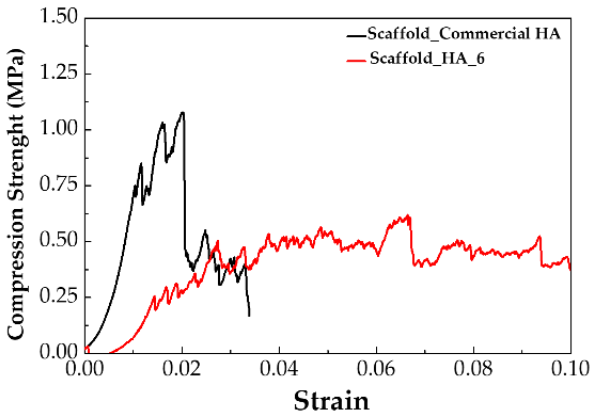

Figure 4.10 – Evaluation of the compressive strength in dependance with the strain for both scaffolds.

Commonly, the mechanical performances are related to the porosity of the materials. Hadagalli et al. reported the preparation via foaming of porous structures of marine origin (cuttlefish bones), which were characterized by a maximum porosity of almost 50%.[42] In this thesis, the porosity reached was higher (almost 90%) than the one observed by Hadagalli et al., and the compressive strength values were in agreement with the previously reported strength-porosity curves.[24]

Figure 4.10 shows a significant decrease in compressive strength of the HA_6 scaffold in comparison to the control one. On the other hand, HA_6 scaffold exhibited a significantly higher strain toughness (work of fracture, Table 4.9), intended as the mechanical deformation energy per unit of volume before fracture.

Table 4.9 - Mechanical properties of HA_6 scaffold and commercial HA scaffold

Sample name	Porosity (%)	Compressive Strength (MPa)	Young's Modulus (MPa)	Work of fracture (mJ m^{-3})
Scaffold HA_6	87,8 ± 0,1	0,5 ± 0,1	36,0 ± 12,0	34,0 ± 7,0
Scaffold Commercial HA	85,4 ± 0,7	1,1 ± 0,3	68,0 ± 26,0	16,0 ± 6,0

A possible explanation could consist in their different morphologies observed by SEM microscope. Indeed, HA_6 scaffold was more porous than commercial HA scaffold, which was more consolidated. It should be noted that the stress propagation is mainly dominated by small solid areas, which form walls and edges of the pores. In this condition, the stress is only concentrated in such small regions, and it will lead to plastic or brittle deformation even while the applied force during testing was still in the elastic range. For this reason, it is reasonable to assume that the significant increase in strain toughness for HA_6 sample, can be ascribable to the intergranular micro-porosity. Indeed, this may cause more micro-fractures under the same strain and finally an increased strain energy consumption. Moreover, the friction between broken fragments of cell walls dissipated extra energy.[43] Likewise, the higher maximum compressive strength value exhibited by the control sample can be ascribable to the stronger necking areas between the grains, possibly requiring more energy to break the struts than for the HA_6 sample.

4.5. Conclusion

HA nanoparticles were successfully prepared from mussel shells (Mytilus edulis), which are one of the most abundant by-products produced by fish industries. Subsequently, this powder was used to prepare a macroporous 3D scaffold by direct foaming technique. The natural CaPs-based scaffold was characterized by an open interconnected porosity (87 – 89%) with pore size between 50 and 300 µm, and good mechanical properties (compressive strength of 0,51 MPa). All the physical and mechanical requisites were achieved in order to produce a scaffold suitable to be used as bone substitute. Further studies regarding the *in vitro* and *in vivo* behaviour of this kind of scaffolds and their preparation with other production methods, such as 3D printing, will be performed.

To sum up, the results obtained in this part of the thesis demonstrate that mussel shell by-products can constitute a sustainable source for the development of high added value systems for biomedical applications.

References:

1. Furth, M. E. & Atala, A. Tissue Engineering. in *Principles of Tissue Engineering* 83–123 (Elsevier, 2014). doi:10.1016/B978-0-12-398358-9.00006-9.
2. Rodrigues, M. T. *et al.* Bioinspired materials and tissue engineering approaches applied to the regeneration of musculoskeletal tissues. in *Engineering Strategies for Regenerative Medicine* 73–105 (Elsevier, 2020). doi:10.1016/B978-0-12-816221-7.00003-3.
3. Santin, M. Bone tissue engineering. in *Bone Repair Biomaterials* 378–422 (Elsevier, 2009). doi:10.1533/9781845696610.3.378.
4. Akter, F. & Ibanez, J. Bone and Cartilage Tissue Engineering. in *Tissue Engineering Made Easy* 77–97 (Elsevier, 2016). doi:10.1016/B978-0-12-805361-4.00008-4.
5. Canadas, R. F., Pina, S., Marques, A. P., Oliveira, J. M. & Reis, R. L. Cartilage and Bone Regeneration—How Close Are We to Bedside? in *Translating Regenerative Medicine to the Clinic* 89–106 (Elsevier, 2016). doi:10.1016/B978-0-12-800548-4.00007-3.
6. Diaz-Rodriguez, P., López-Álvarez, M., Serra, J., González, P. & Landín, M. Current Stage of Marine Ceramic Grafts for 3D Bone Tissue Regeneration. *Mar. Drugs* **17**, 471 (2019).
7. Tavoni, M., Dapporto, M., Tampieri, A. & Sprio, S. Bioactive Calcium Phosphate-Based Composites for Bone Regeneration. *J. Compos. Sci.* **5**, 227 (2021).
8. Turnbull, G. *et al.* 3D bioactive composite scaffolds for bone tissue engineering. *Bioact. Mater.* **3**, 278–314 (2018).
9. Karageorgiou, V. & Kaplan, D. Porosity of 3D biomaterial scaffolds and osteogenesis. *Biomaterials* **26**, 5474–5491 (2005).
10. Milazzo, M. *et al.* Additive Manufacturing Approaches for Hydroxyapatite-Reinforced Composites. *Adv. Funct. Mater.* **29**, 1903055 (2019).
11. Novotna, L. *et al.* Biphasic calcium phosphate scaffolds with controlled pore size distribution prepared by in-situ foaming. *Mater. Sci. Eng. C* **95**, 363–370 (2019).
12. Li, X. *et al.* Fabrication and Properties of Ca-P Bioceramic Spherical Granules with Interconnected Porous Structure. *ACS Biomater. Sci. Eng.* **3**, 1557–1566 (2017).
13. Colombo, P., Vakifahmetoglu, C. & Costacurta, S. Fabrication of ceramic

components with hierarchical porosity. *J. Mater. Sci.* **45**, 5425–5455 (2010).

14. Ma, H., Feng, C., Chang, J. & Wu, C. 3D-printed bioceramic scaffolds: From bone tissue engineering to tumor therapy. *Acta Biomater.* **79**, 37–59 (2018).
15. He, J., Shao, H. & Lin, T. Effect of magnesium silicate on 3D gel-printing of hydroxyapatite ceramic composite scaffold. *Int. J. Appl. Ceram. Technol.* **16**, 494–502 (2019).
16. Kanwar, S. & Vijayavenkataraman, S. Design of 3D printed scaffolds for bone tissue engineering: A review. *Bioprinting* **24**, e00167 (2021).
17. Babaie, E. & Bhaduri, S. B. Fabrication Aspects of Porous Biomaterials in Orthopedic Applications: A Review. *ACS Biomater. Sci. Eng.* **4**, 1–39 (2018).
18. Studart, A. R., Gonzenbach, U. T., Tervoort, E. & Gauckler, L. J. Processing Routes to Macroporous Ceramics: A Review. *J. Am. Ceram. Soc.* **89**, 1771–1789 (2006).
19. Gómez-Morales, J., Iafisco, M., Delgado-López, J. M., Sarda, S. & Drouet, C. Progress on the preparation of nanocrystalline apatites and surface characterization: Overview of fundamental and applied aspects. *Prog. Cryst. Growth Charact. Mater.* **59**, 1–46 (2013).
20. Kumar, G. S. *et al.* One step method to synthesize flower-like hydroxyapatite architecture using mussel shell bio-waste as a calcium source. *Ceram. Int.* **43**, 3457–3461 (2017).
21. Miculescu, F. *et al.* Facile synthesis and characterization of hydroxyapatite particles for high value nanocomposites and biomaterials. *Vacuum* **146**, 614–622 (2017).
22. Pal, A. *et al.* Mechanochemical synthesis of nanocrystalline hydroxyapatite from Mercenaria clam shells and phosphoric acid. *Biomed. Phys. Eng. Express* **3**, 015010 (2017).
23. Shavandi, A., Bekhit, A. E.-D. A., Ali, A. & Sun, Z. Synthesis of nano-hydroxyapatite (nHA) from waste mussel shells using a rapid microwave method. *Mater. Chem. Phys.* **149**–**150**, 607–616 (2015).
24. Dapporto, M., Sprio, S., Fabbi, C., Figallo, E. & Tampieri, A. A novel route for the synthesis of macroporous bioceramics for bone regeneration. *J. Eur. Ceram. Soc.* **36**, 2383–2388 (2016).
25. Walsh, P. J. *et al.* Low-pressure synthesis and characterisation of hydroxyapatite

derived from mineralise red algae. *Chem. Eng. J.* **137**, 173–179 (2008).

26. Santhosh, S. & Balasivanandha Prabu, S. Thermal stability of nano hydroxyapatite synthesized from sea shells through wet chemical synthesis. *Mater. Lett.* **97**, 121–124 (2013).
27. Hou, Y. *et al.* Marine shells: Potential opportunities for extraction of functional and health-promoting materials. *Crit. Rev. Environ. Sci. Technol.* **46**, 1047–1116 (2016).
28. Dapporto, M. Development of new bioactive and porous apatitic scaffolds for the regeneration of load-bearing bones. (University of Bologna, 2016).
29. Kwon, H.-B. *et al.* Recycling waste oyster shells for eutrophication control. *Resour. Conserv. Recycl.* **41**, 75–82 (2004).
30. Piccirillo, C. *et al.* Biphasic apatite-carbon materials derived from pyrolysed fish bones for effective adsorption of persistent pollutants and heavy metals. *J. Environ. Chem. Eng.* **5**, 4884–4894 (2017).
31. Soisuwan, S., Phommachant, J., Wisaijorn, W. & Praserthdam, P. The Characteristics of Green Calcium Oxide Derived from Aquatic Materials. *Procedia Chem.* **9**, 53–61 (2014).
32. Chen, W., Oldfield, T. L., Patsios, S. I. & Holden, N. M. Hybrid life cycle assessment of agro-industrial wastewater valorisation. *Water Res.* **170**, 115275 (2020).
33. Xia, X. *et al.* A facile synthesis of hydroxyapatite for effective removal strontium ion. *J. Hazard. Mater.* **368**, 326–335 (2019).
34. Iafisco, M. & Margiotta, N. Silica xerogels and hydroxyapatite nanocrystals for the local delivery of platinum–bisphosphonate complexes in the treatment of bone tumors: A mini-review. *J. Inorg. Biochem.* **117**, 237–247 (2012).
35. Bastan, F. E., Erdogan, G. & Ustel, F. Role of strontium substitution in spray drying of hydroxyapatite: A comparative study on physical properties. *Int. J. Appl. Ceram. Technol.* **17**, 1155–1166 (2020).
36. Belpassi, A., Dolcini, L. & Martinetti, R. A Process for the Production of Porous Calcium Phosphate Articles for Bone Regeneration and as a Support for Cells and the Porous Articles Themselves. (2002).
37. Tan, C. Y., Singh, R., Teh, Y. C., Tan, Y. M. & Yap, B. K. The Effects of Calcium-to-Phosphorus Ratio on the Densification and Mechanical Properties of

Hydroxyapatite Ceramic. *Int. J. Appl. Ceram. Technol.* **12**, 223–227 (2015).

38. Li, W. X., Gao, M., Song, Y. & Wang, F. P. Thermal stability and mechanical properties of zirconia–hydroxyapatite composites. *Mater. Res. Innov.* **18**, S4-487-S4-489 (2014).
39. Fahami, A., Beall, G. W. & Betancourt, T. Synthesis, bioactivity and zeta potential investigations of chlorine and fluorine substituted hydroxyapatite. *Mater. Sci. Eng. C* **59**, 78–85 (2016).
40. Predoi, D. *et al.* Evaluation of Antibacterial Activity of Zinc-Doped Hydroxyapatite Colloids and Dispersion Stability Using Ultrasounds. *Nanomaterials* **9**, 515 (2019).
41. Karageorgiou, V. & Kaplan, D. Porosity of 3D biomaterial scaffolds and osteogenesis. *Biomaterials* **26**, 5474–5491 (2005).
42. Hadagalli, K., Panda, A. K., Mandal, S. & Basu, B. Faster Biomineralization and Tailored Mechanical Properties of Marine-Resource-Derived Hydroxyapatite Scaffolds with Tunable Interconnected Porous Architecture. *ACS Appl. Bio Mater.* **2**, 2171–2184 (2019).
43. He, L.-H., Standard, O. C., Huang, T. T. Y., Latella, B. A. & Swain, M. V. Mechanical behaviour of porous hydroxyapatite. *Acta Biomater.* **4**, 577–586 (2008).

5. CaPs for cosmetic applications

5.1. Introduction

In this chapter the preparation of CaP obtained from fish bones for cosmetic applications as a novel and safe ingredient in sunscreen formulation was reported. Sunscreens are used to protect our skin from diseases caused by strong or prolonged sun ultraviolet radiation (UVR) exposure such as sunburn, erythema, photoaging, wrinkles, altered pigmentation, or even skin cancer.[1–4] The active ingredients contained in these formulations, called UV-filters, are able to reflect, absorb, and scatter both UVA (320-400 nm) and UVB (290-320 nm) in order to provide protection against both types of radiation, as written by Pirotta in the book of Tovar-Sanchèz *et al*.[5] Indeed, common commercial sunscreen formulations usually contain several UV-filters in order to ensure a whole UV range protection. UV-filters are categorized in two classes: (i) organic or chemical filters, capable to absorb UVR and (ii) inorganic or physical filters, which can absorb, reflect, or scatter the incident UVR. Both kinds of UV filters can cause problems for health and environment, which are widely reported in literature.[3,4,6–9] In particular, organic filters can penetrate into the skin and in the bloodstream, causing photo-allergies, phototoxic reactions which may produce reactive oxygen species (ROS), and skin irritations.[10] Moreover, several studies reported the contamination of UV filters in almost all water sources around the world, and their removal by using common wastewater treatments is very difficult.[7,11] Sunscreen pollution in marine environment brings serious consequences in coastal ecosystem. Indeed, it was estimated that 14,000 tons of UV filters are released in coral reefs area each year, leading to the coral death or coral bleaching phenomena. This occurs because UV-filters kill coral organism by photo oxidation with production of reactive species, by endocrine disruption, and by DNA damage.[12]

Commonly, physical, or inorganic UV-filters are considered as a safer alternative to organic filters, but they still present come criticalities.

The use of micro-sized inorganic UV-filters lead to the whitening effect, that is caused by the high refractive index of inorganic UV-filters which decreases the aesthetic value of

Part of the content of this chapter has been published as A.Lilaj "Characterization and SPF booster effect of natural calcium phosphate derived from fish industry bio-wastes", G.Magnani "Photo-protective performances and Life Cycle Assessment of a novel SPF booster developed from the circular economy of food by-products: towards more sustainable sunscreen", and F.Carella, L. Degli Esposti et al. "The Use of Calcium Phosphates in Cosmetics, State of the Art and Future Perspectives"; and will be published as A.Adamiano, F.Carella et al. "Calcium phosphates from fishery by-products as sun protection factor booster; a circular economy approach for the cosmetic industry".

sunscreens due to the unnatural white colour acquired by the skin after application.[13,14] On the other hand, these UV-filters in NPs form might cause their penetration into the skin causing skin allergies or irritation.[15,16] The only two commonly used inorganic UV-filters that accepted in micro-sized form by the Food and Drug Administration (FDA) are titanium dioxide (TiO_2) and zinc oxide (ZnO). In literature are reported several studies about the dangerousness of these filters in nano-sized form due to their photocatalytic properties. Indeed, under sunlight irradiation the photocatalytic process generates free radicals or other reactive species that could cause skin damage or long-term illnesses, and this can occur even if these NPs are coated by an inert oxide layer.[17–24]

To overcome the necessity to replace these UV-filters and avoid percutaneous absorption or unhealthy effect, CaPs have been proposed as safe inorganic sunscreen ingredient that could provide a broad protection over UVA and UVB, non-toxicity, no photocatalytic effects, and environmental safety. For these reasons, the interest in CaPs as sunscreen ingredients that can replace ZnO or TiO_2 has gained interest, as shown by the production of research articles and patents.[25–42] Indeed, it was found that HA shows not only non-toxicity and biocompatibility properties, but also screening capability, high dermal tolerance, and a lower whitening effect than other inorganic sunscreen agents. However, the main problem of CaPs for sunscreen application consists in their intrinsic UV absorption limit, which is related to CaP electronic structure. CaP has optical absorption only in the range from 200 to 340 nm with a strong band below 247 nm and it depends on the thermal treatment carried on it,[43] but by introducing foreign elements into CaP crystal structure as dopants it is possible to modify their absorption limit. The addition of transition elements into HA structure is allowed by a cation exchange reaction with the calcium ions on the surface of the material. In literature, there are many articles that describe the differences between absorption spectrum of doped and undoped CaPs, allowing the material to absorb in the range from UVB to UVA. As an example, the addition of Fe^{3+}, Cr^{3+}, Mn^{2+}, Zn^{2+}, or Ag^{+} could improve the optical properties of the CaPs, showing an higher UV absorption over the whole UV range.[27,34,35,41,42,44,45] In some cases, the addition of a foreign element could induce the generation of a coloured film of sunscreen, which could be resolved by optimizing the formulation and providing a good dispersion of the ingredient on the skin, giving a transparent appearance when

applied.[29,30] Despite the large number of publications about CaP doped, in most of them non-doped CaP were usually studied in comparison to doped ones. For these reasons, the aim of this chapter consisted in the production and characterization of novel CaP-based booster ingredients both undoped and doped for sunscreen formulations. This work was divided in three main parts: i) the preparation of a natural CaP derived from fish bones from industry waste following a circular economy approach (CaP-N); ii) the determination of the best interaction between CaP-N and commercial UV-filters; and iii) the optimization of the booster effect of CaP-N by using the doping process. The physical and chemical properties of the obtained powders were explored through different methods of characterization and the SPF booster performances were determined by the SPF in vitro analysis. Finally, to evaluate the variations made by the presence of CaP-N in the formulations, an accelerated stability study was carried out on marketable creams prepared with and without CaP-N.

5.2. Materials and methods

5.2.1. Materials

Salmon bones (Salmo salar) were furnished by a local company (FarPro, Emilia-Romagna, Italy) that prepare ingredients for both pet-food and aquaculture. Phosphoric acid (Sigma Aldrich, ACS reagent, ≥85 wt.% pure in H_2O), calcium hydroxide (Sigma Aldrich, ACS reagent, ≥ 95.0% pure), manganese (II) chloride ($MnCl_2$, Sigma Aldrich, 98% pure) and zinc chloride ($ZnCl_2$, Sigma Aldrich, ≥ 98%) were supplied by Sigma-Aldrich (St. Luis, MO, USA). All the solutions were prepared with ultrapure water (18.2 MΩ × cm, 25°C, Arium© pro, Sartorius, Gottingen, Germany). Glycerine ($C_3H_8O_3$, BioXtra, ≥ 99%), ethylenediaminetetraacetic acid tetrasodium salt hydrate - sodium EDTA ($C_{10}H_{14}N_2Na_4O_9$, Sigma Aldrich, ≥ 95%), xanthan gum ($C_{35}H_{49}O_{29}$, Sigma Aldrich), emulgade® 165 (mixture of glyceryl stearate and PEG-100 stearate, BASF), cetearyl Alcohol ($CH_3(CH_2)_nOH$, BASF), dicaprylyl carbonate ($C_{17}H_{34}O_3$, BASF), myritol® 331 (mixture of decanoyl/octanoyl glyceride, BASF), dioctyl carbonate ($C_{17}H_{34}O_3$, BASF), cetyl stearyl alcohol ($CH_3(CH_2)_nOH$, BASF), and poly(dimethylsiloxane) ($(C_2H_6OSi)_n$, Dow) were used for the preparation of emulsions. Finally, the UV-filters octocrylene ($C_{24}H_{27}NO_2$), octinoxate ($C_{18}H_{26}O_3$), and padimate-O ($C_{17}H_{27}NO_2$) were purchased by BASF.

5.2.2. Optimization of a novel sunscreen ingredient from fish industry by-products

Initially, a CaP powder was developed from natural sources (CaP-N). Moreover, it was also produced a synthetic HA as a reference, which is already in use for cosmetic applications.

Preparation of CaP-N

The fish by-products were obtained from the separation of the meat from the bones, followed by a drying treatment at 105°C over-night to reduce the water content. Subsequently, fish by-products were treated by calcination to burn the organic residues, obtaining CaP-N sample. The calcination was performed in an electric furnace using a thermal ramp of 100°C/h followed by a one-hour isotherm at 800 °C. After cooling, the CaP-N was firstly grinded with a high-energy ball mill for 30 minutes and then sieved using a stainless-steel sieve to obtain particles with a diameter lower than 150 µm. Afterwards, the particle diameter was further reduced with a micronizer, which exploits the friction between the particles to reduce their size obtaining a more uniform powder. The final CaP-N particles were characterized by a narrow diameter distribution lower than 50 µm.

Preparation of HA as a reference

HA was synthesized by a wet precipitation method. Briefly, 300mL of a H_3PO_4 solution (0.6 M) was added dropwise into 400 mL of a basic suspension of $Ca(OH)_2$ (0.75 M) and the mixture was kept at 40°C under continuous stirring. Once the neutralization reaction was completed (pH 6.0 ± 0.5), the solution was maintained at 40°C for 3h under continuous stirring and then left to age for 24h at room temperature without further stirring. Finally, the supernatant was removed by centrifugation and the obtained HA was cleaned with ultrapure water, and then freeze-dried. The obtained powder was processed in the same way previous described for CaP-N.

CaP-N and HA characterization

CaP-N was analyzed by XRD, ICP-OES, FEG-SEM and UV-Vis spectrophotometer to identify the phases in the samples, to quantify the elements in the materials, to evaluate their morphology, and to collect the reflectance spectra of powdered samples, respectively.

Furthermore, the particle size distribution of the samples was determined by using a Sedigraph5100 III plus (Micromeritics, USA). The instrument uses an X-ray which pass thought the sample and moves vertically, evaluating the particles from the largest and heaviest ones up to the smaller and best dispersed ones. The fundamental parameters that enable the instrument to calculate the sedimentation rate of the solid dispersed in a liquid, providing the particle size distribution of the powder, are temperature, density and viscosity of the liquid, and density of the powder. The sample preparation consisted in the dispersion of 3.5 g in approximately 80 mL of hexametaphosphate (Calgon) and a subsequent disaggregation by ultrasound probe with 50% amplitude for 3 min.

Photocatalytic test of CaP-based materials

Rhodamine B (RhB) was chosen to evaluate and compare the photocatalytic performance of CaP-N and HA. Furthermore, these materials have been compared to two common UV-filters: TiO_2 and ZnO. 0,030 g of each powder was added in 50 mL of RhB solution with a concentration of 5 mg L^{-1}. The mixed solution was stirred for 30 minutes in dark to achieve adsorption-desorption equilibrium. Then, the solution was irradiated with UV light using a 300 W lamp with an intensity of the radiation equal almost to 44 W m^{-2}. After several time point (from 0 to 2h, each 15 minutes), a 4mL aliquot was removed and centrifuged (10.000 rpm for 1 minute) in order to avoid particles scattering during UV-Vis analysis. Subsequently, the absorption of the supernatant at 554 nm was evaluated. The results were compared with the blank test performed as control in the same working conditions. Eventually, the photocatalytic activity was quantified as the photodegradation rate constant of catalyst, k_{app} (min^{-1}), which was calculated according to Equation 5.1.

$$\ln {}^{C_0}/_{C} = k_{app} t \qquad \text{(Equation 5.1)}$$

where Co is RhB concentration at time zero and C is RhB concentration at time t. The photodegradation of RhB in presence of a catalyst can be considered as a pseudo-first order reaction.

5.2.3. Optimization of the interaction between UV-filters and CaP-N

The booster effect of CaP-N was evaluated preparing basic oil in water emulsion (O/W) with two different concentrations of organic filter (10 %, 20 %) and CaP-N (5 %, 9 %). This

formulation was replicated for each UV-filter tested: octocrylene (OCE), octinoxate (OCN), and padimate O (PAD), and they are reported in Table 5.1.

Table 5.1 - Samples for formulas optimization with relative UV-filters % and CaP-N%.

Sample	% OCE	% OCN	% PAD	% CaP-N
10% OCE	10	-	-	0
15% OCE	10	-	-	5
19% OCE	10	-	-	9
20% OCE	20	-	-	0
25% OCE	20	-	-	5
29% OCE	20	-	-	9
10% OCN	-	10	-	0
15% OCN	-	10	-	5
19% OCN	-	10	-	9
20% OCN	-	20	-	0
25% OCN	-	20	-	5
29% OCN	-	20	-	9
10% PAD	-	-	10	0
15% PAD	-	-	10	5
19% PAD	-	-	10	9
20% PAD	-	-	20	0
25% PAD	-	-	20	5
29% PAD	-	-	20	9

More in detail, OCE is a UVB filter with an aromatic structure characterized by a λ_{max} around 303 nm and a modest ε of about 12600. OCN, instead, is a UVB filter characterized by an electron-releasing group (OCH_3) and an electron-accepting group, and it has a λ_{max} of 311 nm and a quite high ε (23000). The last UVB filter is the PAD which is a Para-amino benzoic acid (PABA) with some modifications in its the amino and carboxy groups. The variations were necessary due to the possible implication of PABA in irritation cases or due to their potential carcinogenic nature. PAD has a λ_{max} of 311 nm and ε of 27000. It is worth to note that to investigate the booster effect of CaP-N and to identify a trend, the

concentrations of UV filters used were even above the norm. Indeed, to achieve high SPFs remaining within these limits it is necessary to combine several filters.

The preparation of the hot/hot O/W emulsion involved three phases. The aqueous phase A contained a humectant (Glycerin), a chelating agent used as preservative (EDTA) and a natural polymer used as gelling agent (Xanthan gum). The oily phase B contained a non-ionic emulsifier (Emulgade 165), an emollient and rheological modifier (Lanette O), a fast-spreading emollient (Cetiol CC), a medium spreading emollient (Myritol 331), a polymer with texturizing anti-foam and barrier properties (Silicone 200-350), and UV-filters. Finally, the last phase C was composed by the SPF booster. Briefly, phase A was prepared by adding water, glycerin and EDTA, and heating the mix to 75°C while stirring with an overhead propeller (LD Overhead Stirrer - Velp Scientifica model 2). Once the temperature was reached, the xanthan gum was added under continues agitation. In the meanwhile, phase B was prepared separately. All the ingredients were added in the same beaker, and they have been heated to the same temperature as phase A (75°C). Then, the oily phase B was added to the aqueous phase A under vigorous stirring with the overhead propeller. Finally, the CaP booster (phase C) was added to the mixture without stopping the stirring until the emulsion was formed. Later, the emulsion was completed putting it under a homogenizer (Helidolph Diax 600) for 3 minutes. The composition of the obtained sunscreen formulations was reported in the Table 5.2.

Table 5.2 – General composition of the sunscreens produced.

PHASE	INGREDIENT	10%	15%	19%	20%	25%	29%
A	Water (g)	34,20	32,30	30,78	30,40	28,50	26,98
	Glycerin (g)	1,50	1,42	1,35	1,33	1,25	1,18
	EDTA (g)	0,05	0,05	0,05	0,04	0,04	0,04
	Xanthan gum (g)	0,10	0,09	0,09	0,09	0,08	0,08
B	Emulgade 165 (g)	2,75	2,60	2,48	2,44	2,29	2,17
	Lanette O (g)	0,90	0,85	0,81	0,80	0,75	0,71
	Cetiol CC (g)	2,50	2,36	2,25	2,22	2,08	1,97
	Mytirol 331 (g)	2,50	2,36	2,25	2,22	2,08	1,97
	Silicone 200-350 (g)	0,50	0,47	0,45	0,44	0,42	0,39
	UV filter* (g)	5	5	5	10	10	10

C	SPF booster (g)	0	2,5	4,5	0	2,5	4,5
	Total (g)	50,00	50,00	50,00	50,00	50,00	50,00

* UV filters were OCE, OCN and PAD.

5.2.4. SPF in vitro measurements

The SPF evaluation was performed following the COLIPA 2009 guidelines "In vitro method for the determination of the UVA protection factor and critical wavelength values of sunscreen products" prepared by the COLIPA in vitro UV Protection Method Task Force, which consist in the determination of the UV transmittance of a thin film of sunscreen sample spread on a roughened substrate. The instrumentation used were the UV-Vis spectrophotometer for the determination of the transmittance and polymethylmethacrylate (PMMA) plates Helioplate produced by Helioscreen Labs as roughened substrate. In particular, an aliquot of each sunscreen cream was applied as a number of small droplets with an application rate of 1.3 mg cm^{-2} on the PMMA plates. Then, the sunscreen product was spread without pressure over the whole surface in less than 30 seconds, using light strokes with a fingertip "pre-saturated" with the same tested cream. After almost 20-30 seconds, the sunscreen was applied with more pressure in order to be well absorbed on the surface of the PMMA plates. All treated samples were left in a dark environment at RT for at least 15 minutes to facilitate the formation of a standard stabilized product film. Eventually, the transmittance spectra were acquired in the wavelength range within 290 and 400 nm with a step of 1.0 nm. The analysis was carried out in triplicate and for each PMMA plate and four measurements were performed rotating it on the four sides, accounting for a total of 12 acquisitions per sample.

The SPF *in vitro* was so calculated using the Equation 5.2.

$$SPF = \int_{290nm}^{400nm} E(\lambda) * I(\lambda) * d\lambda \Big/ \int_{290nm}^{400nm} E(\lambda) * I(\lambda) * 10^{-A_0(\lambda)} * d\lambda \qquad \text{(Equation 5.2)}$$

Where E(λ) is the erythema action spectrum (CIE 1987) at a specific wavelength, I(λ) is the spectral irradiance of the UV source (SSR for SPF testing) per wavelength (Wm^{-2} nm), $A_0(\lambda)$ is the monochromatic absorbance measurement per plate at wavelength λ, and d(λ) which is the wavelength step previously set (1 nm).

Linearity assessment

Before analyzing the samples, to check the spectrophotometer performances two PMMA standard plates were analyzed. Initially, it was measured the absorbance of the first plate called 'Slide A'. Then, the second standard plate nominated 'Slide B' was measured in the same conditions. Finally, PMMA plates were overlapped on each other and their absorbance, which should be double compared to the single ones, was measured (Figure 5.1).

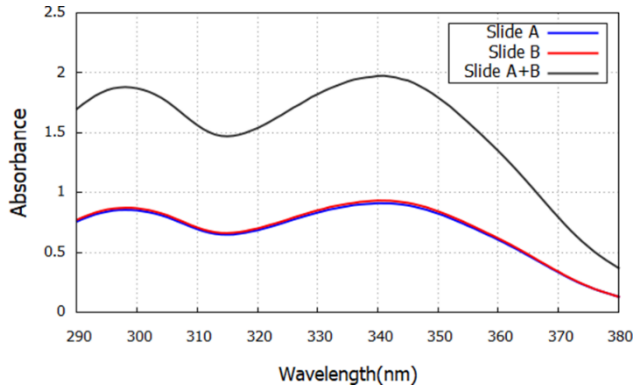

Figure 5.1 - Absorption spectra of PMMA calibration plate used for the spectrophotometer linearity assessment

5.2.5. Optimization of the booster effect of the CaP material

CaP-N doping with zinc or manganese chloride

CaP-N was then subjected to doping in order to improve its booster effect. Briefly, 2.0g of CaP-N was put in contact with 200mL of a solution of $ZnCl_2$ or $MnCl_2$ under stirring at 60°C for 5 hours. At the end of the process, the powder was separated by centrifugation (10.000 rpm for 3 min) and cleaned with ultrapure water for three times. Finally, the sample was dried in a ventilated oven at 40 °C. The concentration of the doping solutions used in this process (10 wt.%, 100 wt.%, and 200 wt.%) were calculated depending on the calcium moles present in the material. The final materials obtained are reported in Table 5.3.

Table 5.3 – Materials obtained after doping and their abbreviations

Materials	Abbreviations
Natural Calcium Phosphate doped Zn 10%	CaPZn10-N
Natural Calcium Phosphate doped Zn 100%	CaPZn100-N
Natural Calcium Phosphate doped Zn 200%	CaPZn200-N

Natural Calcium Phosphate doped Mn 10%	CaPMn10-N
Natural Calcium Phosphate doped Mn 100%	CaPMn100-N
Natural Calcium Phosphate doped Mn 200%	CaPMn200-N

CaP-N doped characterization

The materials were characterized by XRD, ICP-OES, FEG-SEM and UV-Vis spectrophotometer to identify the phases in the samples, to quantify the elements in the materials, to evaluate their variation in morphology, and to collect the reflectance spectra of powdered samples, respectively. Each analysis was compared to the CaP-N one, used as control, to better identify any variation between the samples.

5.2.6. Stability test

Preparation of marketable formulations with CaP-N

The development of sunscreen emulsions based on non-doped CaP-N were carried out to evaluate the effect of CaP-N on the stability of complex and marketable formulas. Sunscreens with different expected SPF values (5, 10, 15 and 25) were produced by Kalichem SRL using a combination of several UV-filters supplied by BASF, Merck and DSM Nutritional Products Europe LTD. Furthermore, it was assumed that CaP-N was comparable to ZnO, and for this reason it was calculated the correct amount of material to reach an SPF 5 points higher than those without it. The preparation procedure the O/W emulsion was similar to the one already explained before. In detail, the oily phase A was brought to the temperature of 72 ± 2 ° C while the aqueous phase B was brought to 75 ± 2 ° C. Once the indicated temperatures were reached, one third of the phase B was slowly poured out in the phase A under mixing and then the remaining part was quickly added during the homogenization. After keeping stirring for about 10 min, the product was cooled in a water bath, under constant agitation until it was reached the temperature of 40°C. Finally, phase C and D were added, and a final homogenization was carried out. In summary, four formulations with and without booster have been developed, for a total of eight formulations, shown in the Table 5.4.

Table 5.4 - Marketable formulations with and without CaP-N for the stability test. Data refers to ingredients wt.% in the formulation. Preservative, parfum and pH regulator were added as needed.

Phase	Ingredient	SPF 10	SPF 5	SPF 15	SPF 10	SPF 25	SPF 15	SPF 30	SPF 25
A	Eusolex HMS	2	2	3	3	4	4	10	10
	Parsol 1789	0,5	0,5	1	1	2	2	2,5	2,5
	Tinosorb OMC	1	1	3	3	4	4		
	Eusolex OCR							1,4	1,4
	Olivoil glutammate emulsifier	10	10	10	10	10	10	10	10
	Octyl palmitate	5,5	5,5	3	3				
	Ceticol C	8	8	8	8	5	5	3,1	3,1
	Cetiol B					3	3	4	4
	Cetyl alcohol	4	4	3	3	3	3		
B	Water	30	65,5	30	65,5	22,5	42,5	11	31
	Glycerin	3,5	3,5	3,5	3,5	3,5	3,5	3,5	3,5
C	Eusolex 232					2	2	3	3
	Water					20	20	30	30
	NaOH 30%					1	1	1,5	1,5
D	**CaP-N booster**	**9**	**0**	**9**	**0**	**6**	**0**	**6**	**0**
	Water	26,5	0	26,5	0	14	0	14	0

Parameters of the stability test

The accelerated stability test was conducted keeping the samples for 3 months in a thermostat (40 °C) or at RT. At scheduled time intervals (t0, 1 day, 1 week, 1 month, 3 months), the chemical and physical properties of each sample was determined. In particular, the parameters chosen to evaluate the stability and thus the degradation of the samples were: odor, color, appearance, pH and functional alteration. Finally, the observation conducted were compared also considering the temperature at which they were stored.

5.3. Results and discussion

5.3.1. Optimization of a novel sunscreen ingredient from fish industry by-products

Initially, the characterization of the CaP-based materials obtained from fish bones or by synthesis, was performed to evaluate the differences between them.

The identification of the phases contained in the samples was performed by XRD. Figure 5.2 reports the XRD patterns of CaP-N and HA particles.

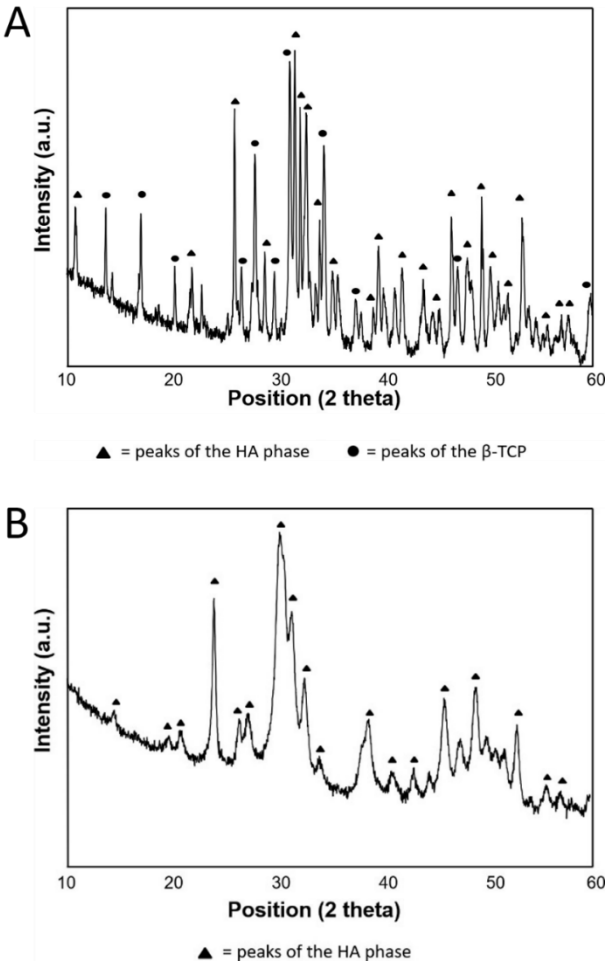

Figure 5.2 – XRD pattern of (A) CaP-N powder prepared from natural source and (B) synthetic HA.

From Figure 5.2 it was possible to observe two main differences between the samples, which were their phase composition and their crystallinity. In detail, synthetic HA obtained from a wet precipitation method was entirely made of poorly crystalline HA (98.5 ± 2.0 wt.%). On the other hand, CaP-N was composed of HA and β-TCP at relatively similar concentrations (41.6 ± 1.0 wt.% and 58.4 ± 1.1 wt.%, respectively), having both a higher crystallinity degree than HA due to the thermal treatment of fish bone at 800 °C. Indeed, it is known that the main mineral component of fish bone consists of non-

stoichiometric HA with a variety of foreign ions (CO_3^{2-}, Na^+, Mg^{2+} etc.) into its structure. The presence of these "impurities" in the lattice determines a certain degree of disorder, which favours the transformation from HA into β-TCP when thermally treated at temperatures above 700 °C. These results agreed with previous studies reported.[46–48] Furthermore, the determination of the elemental composition of CaP-N and HA powders by ICP-OES (Table 5.5) was conducted.

Table 5.5 - Elemental composition of CaP-N and synthetic HA carried out from ICP analysis.

Samples	Ca (wt.%)	P (wt.%)	Ca/P
CaP-N	33.2 ± 0.1	18.6 ± 0.1	1.38 ± 0.01
HA	36.5 ± 0.2	17.0 ± 0.1	1.66 ± 0.02

The Ca/P ratio of HA was close to the stoichiometric one (1.67), while CaP-N ratio was different due to both its biphasic composition (β -TCP as a Ca/P ratio of 1.50) and the common presence of foreign ions (CO_3^{2-}, Na^+, Mg^{2+} etc.) into the structure of CaP prepared from natural sources.

Afterwards, the particle morphology of samples was analyzed by FEG-SEM microscopy and the collected micrographs of CaP-N and HA are shown in Figure 5.3.

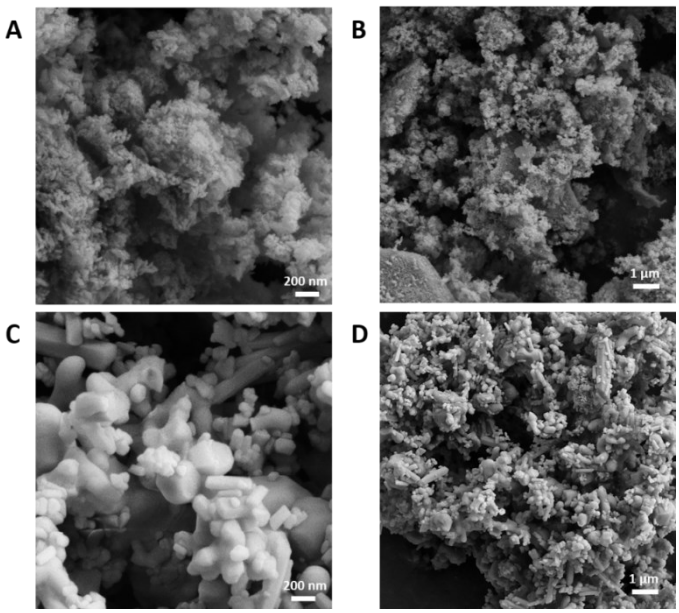

Figure 5.3 – SEM images of synthetic HA (A and B) in comparison with CaP-N (C and D) sample at 100k and 25k magnification, respectively.

Figure 5.3A-B clearly showed the typical apatitic nanostructure consisting of nano-crystals needle-like.[49,50] On the other hand, the morphology of CaP-N (Figure 5.3C-D) was characterized by elongated, rod-like shape submicrometric crystals due to both the thermal treatment of the process from which this material was obtained and its biphasic composition. Indeed, it is worth to notice that in CaP-N hexagonal crystals probable ascribable to HA phase were visible.

Subsequently, the photocatalytic activity of HA and CaP-N compared to the commonly used inorganic UV-filters (TiO_2 and ZnO) was tested using the RhB dye test (Figure 5.4). In this experiment the degradation of RhB was promoted by the following radical species generated because of UV irradiation:

Catalyst + UV → $h^+ + e^-$ $e^- + O_2 \rightarrow O_2^{\bullet -}$ $h^+ + OH^- \rightarrow {}^{\bullet}OH$

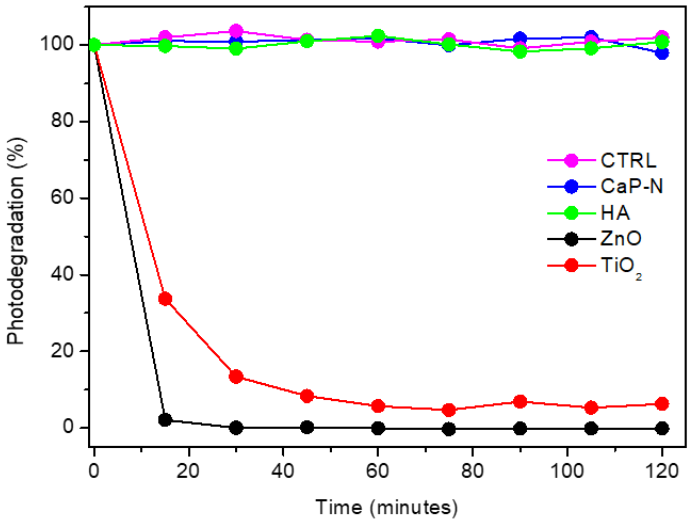

Figure 5.4 - Photocatalytic activity of CaP-N and HA in comparison with commonly used inorganic UV filters (ZnO and TiO2). The degradation rate was plotted against time expressed in minutes. Results compared with RhB as CTRL performed in the same working conditions.

Figure 5.4 clearly highlighted a rapid decrease in the absorption intensities of RhB until its complete degradation over the time in presence of both ZnO and TiO_2. This result is consistent with several works which have reported the photocatalytic activity of nano-ZnO and nano-TiO_2.[51,52] Moreover, a study[53] reported that hierarchal combination of TiO_2 micro-particles with ZnO nanoparticles resulted in a lower photodegradation of the sunscreen in presence of UV light with respect to the singular TiO_2 and ZnO counterparts. On the other hand, CaP-N and HA showed the same intensity of the absorbance of RhB over the time, indicating that both samples could be considered photostable and safe to

use in sunscreens or other cosmetic formulations. These results suggested that a composite made of the photostable micro-size CaP-N instead of the TiO_2 micro-particles, could potentially display the same result in terms of photodegradability. However, this could avoid the inorganic nano-filters amount used nowadays and decrease the possible penetration of the NPs into the human skin.

Eventually, to increase the comparability between HA and CaP obtained from fish bones and to enable an easier incorporation and dispersion of the material into the emulsion, it was necessary to find a method to reduce the particles' size. Two methods were tested: (i) sieving at 20 µm and (ii) micronization. The powders obtained through these two techniques were characterized using Sedigraph, compared to synthetic HA, and the results were presented in Figure 5.5.

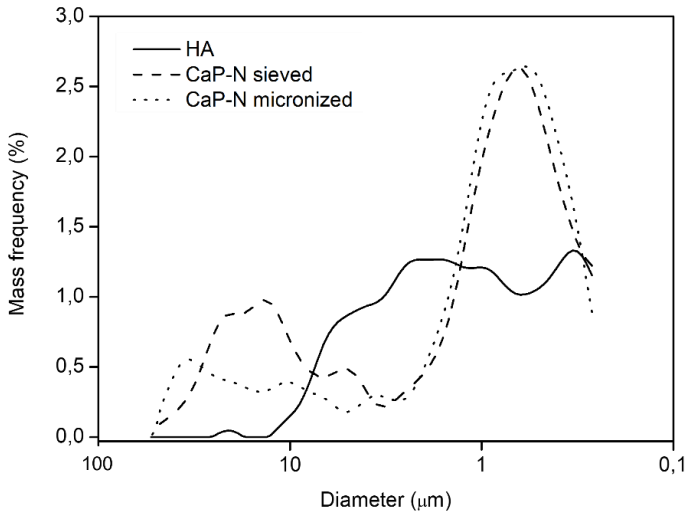

Figure 5.5 - Particle size distribution of HA, CaP-N sieved at 20 µm or micronized, measured by Sedigraph

From Figure 5.5, no significant difference between the two techniques used to reduce the particles' dimension was observed. However, a more homogeneous size distribution was observed after the micronization. Moreover, the median of CaP-N micronized (0.755) was closer to HA median (0.571), while the sample of CaP-N sieved was characterized by a higher median value (0.819). Furthermore, CaP-N micronized sample present greater homogeneity in terms of size distribution compared to HA used as a standard.

From these results, micronization was chosen as the best method for the preparation of a micrometric and homogeneous CaP-N that will be used as SPF booster ingredient in sunscreen formulas.

Finally, the data collected showed that it was possible to obtain a pure CaP-based material from fish bones and therefore, this material was used for further investigations related to the optimization of novel sunscreen formulation.

5.3.2. Optimization of the interaction between UV-filters and CaP-N

CaP-N-based emulsions with three organic filters (OCE, OCN, and PAD), were prepared to evaluate the best interaction between UV-filter and CaP-based material. Then, SPF analysis of each emulsion was conducted, and the results are reported in Table 5.6.

Table 5.6 – SPF values measured on each formulation prepared at two concentration of UV-filter (10% and 20%), and with or without the presence of CaP-N booster (0%, 5% and 9%).

Formulation name	UV-filter (%)	CaP-N booster (%)	SPF value	SD
10% OCE	10	-	22.1	2.2
15% OCE	10	5	26.5	4.6
19% OCE	10	9	27.2	3.9
20% OCE	20	-	40.6	9.2
25% OCE	20	5	53.8	6.4
29% OCE	20	9	80.8	12.7
10% OCN	10	-	21.7	2.9
15% OCN	10	5	23.2	1.8
19% OCN	10	9	23.4	2.4
20% OCN	20	-	24.6	5.1
25% OCN	20	5	35.0	2.1
29% OCN	20	9	32.0	1.7
10% PAD	10	-	7.4	0.3
15% PAD	10	5	6.6	0.2
19% PAD	10	9	6.5	0.2
20% PAD	20	-	9.2	0.1
25% PAD	20	5	8.0	0.2
29% PAD	20	9	7.7	0.2

Concerning the SPF values of the emulsion constituted by only UV-filters with a concentration of 10% and 20% reported in Table 5.6, it was possible to observe that the SPF values obtained by measuring PAD emulsions does not significantly vary, while SPF

measured on OCN emulsions highlighted a visible increase. Moreover, the SPF values of OCE emulsions showed that the value almost doubles as the filter concentration doubles. This trend was also observable in formulation that contained CaP-N booster. In detail, the cream with 10 % of OCE highlighted an SPF increase of 20 % with 5 % of CaP-N and 23 % with 9 %, while in sunscreen with 20 % of OCE the maximum booster effect was almost 100 %. Furthermore, the booster effect visible in formulation with 10 % of OCN was equal to 8 % with 9 % of CaP-N, while in formulation with 20 % of OCN there was a SPF increase of 42 % with only 5 % booster. On the other hand, emulsions with PAD and CaP-N at any concentration showed a decrease in SPF values, which indicated that there was no interaction and thus there was no booster effect in those formulations.

To sum up, these results show an extreme synergy between OCE and CaP-N, probably because this UV-filter is not only high performing, but it was formulated and better dispersed in the emulsion with CaP-N, giving higher booster effect. For these reasons, it was decided to use this filter for the further experiments.

5.3.3. Optimization of the booster effect of the CaP material

CaP-N was doped with Zn and Mn to optimize the booster effect and the physical and chemical properties of the obtained materials were characterized by XRD, ICP, SEM and UV-Vis. Firstly, the determination of the phases present in the samples was carried out by XRD analysis (Figure 5.6).

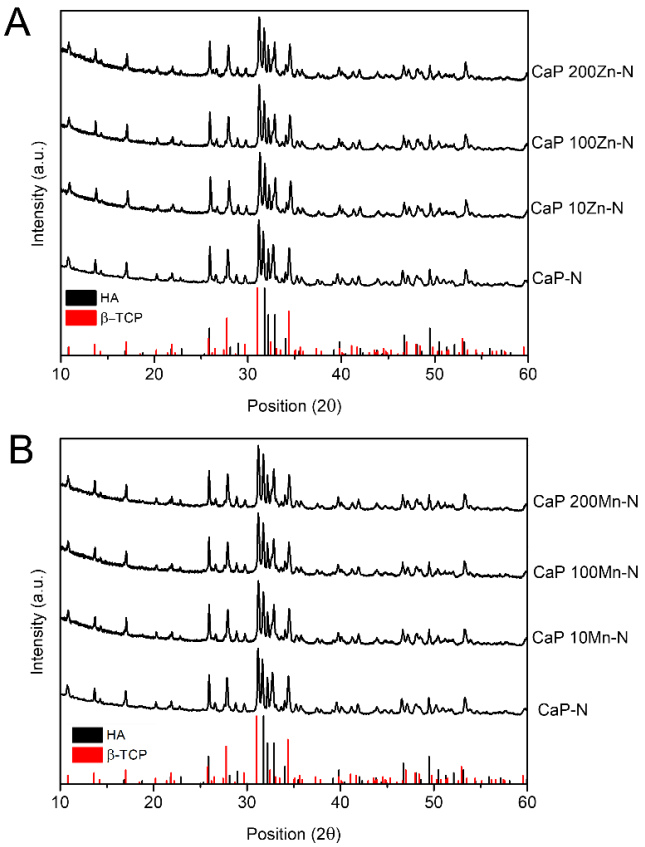

Figure 5.6 - XRD patterns of the obtained material by the doping process on CaP-N with (A) Zn and (B) Mn.

As can be seen from each XRD pattern reported in Figure 5.6, every sample showed a biphasic composition. In particular, Rietveld refinement, reported in Table 5.7 showed that the doping process does not significantly change the composition of the material. In addition, in XRD patterns there were not visible any peaks related to the oxides of Zn and Mn.

Table 5.7 – Phase composition and quantification by Rietveld refinement on XRD patterns.

Sample	HA (%)	SD	β-TCP (%)	SD
CaP-N	41.6	1.0	58.4	1.1
CaP Zn10-N	38.6	0.3	61.4	0.3
CaP Zn100-N	36.7	0.3	63.3	0.3
CaP Zn200-N	37.2	0.4	62.8	0.4
CaP Mn10-N	39.5	0.3	60.5	0.3
CaP Mn100-N	38.8	0.4	61.2	0.4
CaP Mn200-N	39.2	0.3	60.8	0.3

Moreover, to investigate the chemical composition of the obtained materials and to evaluate the amount of doped element present in the prepared CaP-N materials, the ICP analysis was performed, and the results are presented in Table 5.8.

Table 5.8 - ICP results of CaP-N and CaP-N doped at different concentrations of Zn and Mn

Sample	Ca (wt.%)	P (wt.%)	Mn (wt.%)	Zn (wt.%)	Ca/P	(Ca+Mn) /P	(Ca+Zn)/ P
CaP-N	33.2 ± 0.1	18.6 ± 0.1	-	-	1.38 ± 0.01	-	-
CaPZn10-N	30,2 ± 1,5	17,0 ± 0,8	-	2,0 ± 0,1	1,37 ± 0,01	-	1,43 ± 0,01
CaPZn100-N	26,1 ± 2,3	14,3 ± 1,3	-	1,3 ± 0,4	1,42 ± 0,01	-	1,46 ± 0,01
CaPZn200-N	29,3 ± 1,2	16,2 ± 0,6	-	1,4 ± 0,1	1,39 ± 0,01	-	1,43 ± 0,01
CaPMn10-N	29,6 ± 1,0	16,3 ± 0,5	0,9 ± 0,1	-	1,41 ± 0,01	1,44 ± 0,01	-
CaPMn100-N	29,0 ± 0,9	16,0 ± 0,5	0,8 ± 0,1	-	1,40 ± 0,01	1,43 ± 0,01	-
CaPMn200-N	29,7 ± 1,5	16,5 ± 0,9	0,8 ± 0,2	-	1,39 ± 0,01	1,42 ± 0,01	-

From Table 5.8 it was possible to highlight that in both Zn-doped and Mn-doped CaP-N, Ca and P wt.% were lower than those of CaP-N. Moreover, the highest Zn wt.% obtained was 0.9 (0.1) and it did not increase as the amount of nominal Zn increased. The same trend was noticeable for Mn-doped CaP-N, in which the highest Mn wt.% amount was equal to 2.0 (0.1). Finally, there were no differences between the measured Ca/P and (Ca+Zn)/P or Ca/P and (CaP+Mn)/P ratios. From these results, the low detected dopant element percentages were attributed to the high crystallinity and thus less reactivity for cation exchange reactions of the materials. For these reasons, the materials doped with 10% of Zn or Mn have been analyzed in detail. CaP Zn100-N, CaP Zn200-N, CaP Mn100-N and CaP Mn200-N were no longer considered because the increase of the doping amount

used in the synthesis did not lead to a significant increase in the doping element contained in those materials.

Subsequently, these materials were further analyzed by UV-Vis in order to compare and evaluate if the doping process has changed their reflectance spectra (Figure 5.7).

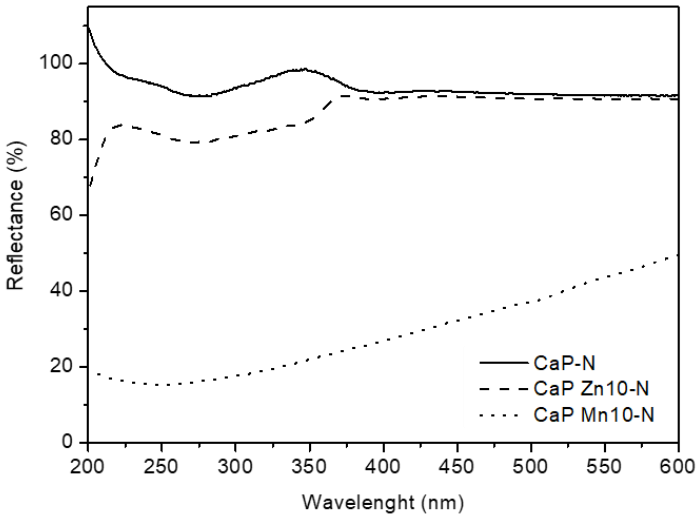

Figure 5.7 - Reflectance spectra of samples at different doping percentage

The sample with the highest reflectance was CaP-N, followed by CaP Zn10-N and finally by CaP Mn10-N. From Figure 5.7 it was possible to notice that doped samples had a lower reflectance than CaP-N. This could be explained by the presence of few, small and/or amorphous nano-sized particles of oxide which have not been detected by XRD. Indeed, their presence would explain the lowering of the reflectance as these oxides could be the responsible for the absorption of radiation. However, it was noticeable a drastic reduction in reflectance for the Mn-doped powder. This could be explained by its colour that changes from the white of undoped CaP to a brownish tone, confirming the formation of a secondary phase made of manganese oxides (Figure 5.8).

Figure 5.8 - Images of CaP-N (A), CaP Zn10-N (B) and CaP Mn10-N (C).

Figure 5.8 shows the color of the materials. Visually, the undoped CaP-N appeared as a greyish-white powder, whereas doped CaP-N appears differently. In particular, Zn-doped powders were white while Mn-doped powders appeared brownish. The presence of a small amount of oxides was confirmed by FEG-SEM analyses (Figure 5.9).

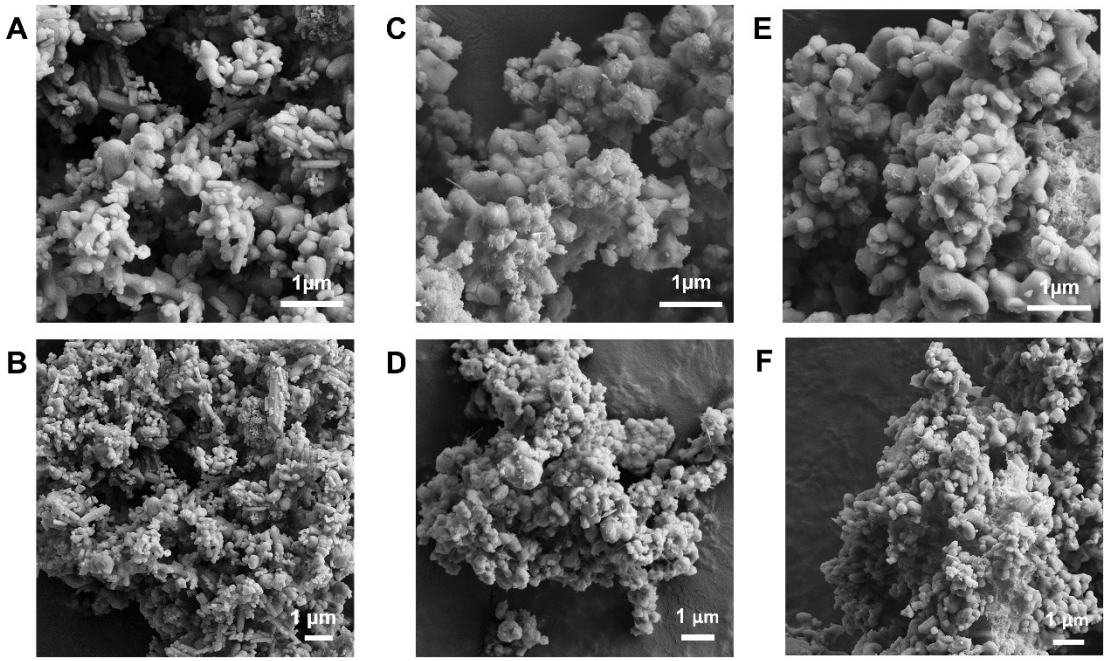

Figure 5.9 - SEM images of CaP-N (A and B), CaP Mn10-N (C and D) and CaP Zn10-N (E and F) at two magnification: 50K and 25k, respectively.

From Figure 5.9 it was possible to observe that the morphology of the material was maintained even after the doping process. On the other hand, the presence of oxides was visible in both CaP Mn10-N and CaP Zn10-N as novel structures on the surface of the material crystals. In particular, samples which contain Mn showed nano-whiskers crystals, while NP were observable in samples with Zn. These results confirmed the formation of small amount of oxides noticed in the previous UV reflectance.

Furthermore, the two doped materials were used to prepare the formulas for the booster optimization and the prepared formulations were reported in Table 5.9.

Table 5.9 – List of the formulations prepared with and without undoped CaP-N, CaP Zn10-N and CaP Mn10-N with OCE.

Formulation name	UV-filter (%)	CaP-N (%)	CaP10Zn-N (%)	CaP 10Mn-N (%)	SPF value	SD
10% OCE	10	0	-	-	22.1	2.2

15% OCE	10	5	-	-	26.5	4.6
19% OCE	10	9	-	-	27.2	3.9
20% OCE	20	0	-	-	40.6	9.2
25% OCE	20	5	-	-	53.8	6.4
29% OCE	20	9	-	-	80.8	12.7
10% OCE-Zn	10	-	0	-	22.1	2.2
15% OCE-Zn	10	-	5	-	20.5	1.2
19% OCE-Zn	10	-	9	-	23.0	2.9
20% OCE-Zn	20	-	0	-	40.6	9.2
25% OCE-Zn	20	-	5	-	57.5	4.8
29% OCE-Zn	20	-	9	-	65.2	10.8
10% OCE-Mn	10	-	-	0	22.1	2.2
15% OCE-Mn	10	-	-	5	21.5	1.4
19% OCE-Mn	10	-	-	9	19.5	2.2
20% OCE-Mn	20	-	-	0	40.6	9.2
25% OCE-Mn	20	-	-	5	62.5	6.9
29% OCE-Mn	20	-	-	9	67.9	10.2

The data reported in Table 5.9, revealed that Zn or Mn doping did not yield any significative benefit in terms of booster effect than the formulation containing undoped CaP-N and OCE. The attempt to increase the booster effect of the material through doping did not provide the expected results probably because of the presence of oxides. For these reasons, further experiments must be carried out in order to achieve, optimize and evaluate how the doping process could affect the booster effect of the material in formulations.

5.3.4. Stability test

The stability study was performed measuring several parameters (odour, colour, appearance, pH and functional alteration) of sunscreen emulsions developed as described in paragraph 5.2.6 at different time points (t0, 1 day, 1 week, 1 month, 3 months). Initially, each formulation was characterized evaluating their SPF, which are reported in Table 5.10.

Table 5.10 – SPF measurements of marketable formulations prepared at several theorical SPF.

Sample	CaP-N	SPF in vitro
SPF 10	Yes	6.9 ± 1.5
SPF 5	No	7.1 ± 0.9
SPF 15	Yes	27.1 ± 3.4
SPF 10	No	20.0 ± 3.8
SPF 30	Yes	23.1 ± 2.9
SPF 25	No	21.7 ± 1.7

From the SPF values reported in Table 5.10 it was possible to notice that the absence of CaP-N in the formulations resulted in a lower SPF than the formulation in which was present. In particular, this trend was observed in the sample pair SPF 15 and SPF 10.

Concerning the stability tests, no significant changes in appearance, functional characteristics, color, and pH were observed in the emulsions prepared without CaP-N. In opposition, the emulsions containing CaP-N showed a color change from a grayish white to a yellowish tone. This variation was more evident in formulations with higher SPF, especially the one at SPF 30 which was characterized by a brownish tone. In addition, it was possible to notice that this phenomenon was more evident in the samples stored at 40°C than in those stored at RT.

Moreover, the odor was evaluated through an organoleptic analysis. The original odor of the emulsions was affected by the ingredients contained in the formulations because no perfume was added to them. The strongest variation in odor was evaluated in the formulations held at 40°C, especially in those with higher SPF. In general, the formulations with CaP-N booster were characterized by an acidic smell over time compared to creams without the booster. The variations in color and odor were indicative of a degradation process caused by the addition of CaP-N in emulsions. On the other hand, the formulation prepared without CaP-N did not show substantial variations. Finally, no signs of reversible separation between the two phases can be observed in the formulations. An exception to this trend was observed in SPF 30 emulsion stored at 40 °C, in which separated water was observed on the top after 3 months.

5.4. Conclusion

Cosmetic products are commonly used to clean, beautify, or alter the appearance without affecting body physiology or functions. Despite their health hazards as heavy metals or parabens, human appearance is considered an important aspect of life due to beauty standards promoted or imposed by societies. Therefore, the cosmetics market is growing. An example are sunscreens, which are commonly constituted by organic filters. These ingredients are poorly sustainable as they are hardly degradable and potentially harmful to consumers and the environment. To overcome these health concerns, it is necessary to reduce the organic filters quantity through the addition of SPF boosters. They are ingredients able to enhance the sunscreen SPF without increasing or even reducing the concentration of organic filters in the formulation. Among the possible SPF booster materials and in the interest of circular economy, it is necessary to develop innovative, natural, and safe cosmetics using non-toxic materials that have high biocompatibility and biodegradability.

For these reasons, this chapter was focused on the production and characterization of CaPs derived from fish bone industry waste following a circular economy approach to implement them in a sunscreen formulation. Synthetic HA, commonly used in cosmetics, was synthesised as a standard for the novel material in order to develop and optimize it for the final application. Therefore, it was achieved a CaP-N sample formed by HA and β-TCP, with a higher crystallinity and higher dimension of the particles than synthetic HA.

In particular, the particles of CaP-N remained in the microscale, which was essential considering the current need in cosmetic industry for non-nano ingredients due to the numerous controversies of NPs. It was also confirmed the safety of this material as it did not show any photocatalytic activity, resulting photostable to use inside sunscreens or in other cosmetic formulations.

The results obtained from the first part of the work, confirmed that it was possible to develop and optimize a CaP, like commonly used HA for cosmetics, from natural sources, which represented an interesting example of circular economy. Furthermore, it was evaluated the capability of the optimized material to be used as SPF booster in sunscreen formulations. Firstly, the best interaction between CaP-N booster and three organic filters (OCE, OCN and PAD) has been investigated. OCE was the UV-filter that gave the highest

SPF increase, showing an extreme synergy with CaP-N, and thus it was selected for the optimization of the material. For this purpose, CaP-N was subjected to a doping treatment with Zn and Mn. From the characterizations performed, Zn and Mn oxides were detected in a small amount, and no other differences were observed with the undoped sample. Subsequently, formulas were realized with OCE, and CaP-N doped with Zn and Mn. The obtained data demonstrate that doping does not yield any substantial benefits in terms of booster effect. Indeed, CaP-N gave better performances than doped one. Lastly, the results obtained from the accelerated stability study carried out on marketable creams, suggested that the emulsions with CaP-N tend to destabilize earlier, undergoing through a degradation process.

In conclusion, the results obtained in this work demonstrated that it was possible to increase the SPF value of a sunscreen formulation by introducing natural CaP-based SPF boosters. This innovative material constituted an interesting alternative to synthetic raw materials, a step towards the circular economy in the cosmetic sector, and a possible answer to the industry waste management. Moreover, it was involved the development of high added value compounds with financial and environmental advantages. On the other hand, further studies are needed to better investigate and understand how doping with photoactive elements can lead to improve CaP-N performances as SPF boosters.

References:

1. Fisher, G. J. *et al.* Pathophysiology of Premature Skin Aging Induced by Ultraviolet Light. *N. Engl. J. Med.* **337**, 1419–1429 (1997).
2. Baldermann, C. & Weiskopf, D. Verhaltens- und Verhältnisprävention Hautkrebs. *Der Hautarzt* **71**, 572–579 (2020).
3. Green, A. C., Williams, G. M., Logan, V. & Strutton, G. M. Reduced Melanoma After Regular Sunscreen Use: Randomized Trial Follow-Up. *J. Clin. Oncol.* **29**, 257–263 (2011).
4. van der Pols, J. C., Williams, G. M., Pandeya, N., Logan, V. & Green, A. C. Prolonged Prevention of Squamous Cell Carcinoma of the Skin by Regular Sunscreen Use. *Cancer Epidemiol. Biomarkers Prev.* **15**, 2546–2548 (2006).
5. Tovar-Sánchez, A., Sánchez-Quiles, D. & Blasco, J. *Sunscreens in Coastal Ecosystems*. vol. 94 (Springer International Publishing, 2020).
6. Sánchez-Quiles, D. & Tovar-Sánchez, A. Sunscreens as a Source of Hydrogen Peroxide Production in Coastal Waters. *Environ. Sci. Technol.* **48**, 9037–9042 (2014).
7. Schneider, S. L. & Lim, H. W. Review of environmental effects of oxybenzone and other sunscreen active ingredients. *J. Am. Acad. Dermatol.* **80**, 266–271 (2019).
8. Fivenson, D. *et al.* Sunscreens: UV filters to protect us: Part 2-Increasing awareness of UV filters and their potential toxicities to us and our environment. *Int. J. Women's Dermatology* **7**, 45–69 (2021).
9. Siller, A., Blaszak, S. C., Lazar, M. & Olasz Harken, E. Update About the Effects of the Sunscreen Ingredients Oxybenzone and Octinoxate on Humans and the Environment. *Plast. Surg. Nurs.* **38**, 158–161 (2018).
10. Narla, S. & Lim, H. W. Sunscreen: FDA regulation, and environmental and health impact. *Photochem. Photobiol. Sci.* **19**, 66–70 (2020).
11. Li, W. *et al.* Occurrence and behavior of four of the most used sunscreen UV filters in a wastewater reclamation plant. *Water Res.* **41**, 3506–3512 (2007).
12. Downs, C. A. *et al.* Toxicopathological Effects of the Sunscreen UV Filter, Oxybenzone (Benzophenone-3), on Coral Planulae and Cultured Primary Cells and Its Environmental Contamination in Hawaii and the U.S. Virgin Islands. *Arch.*

Environ. Contam. Toxicol. **70**, 265–288 (2016).

13. Huang, Y., Law, J. C.-F., Lam, T.-K. & Leung, K. S.-Y. Risks of organic UV filters: a review of environmental and human health concern studies. *Sci. Total Environ.* **755**, 142486 (2021).
14. Berardesca, E., Zuberbier, T., Sanchez Viera, M. & Marinovich, M. Review of the safety of octocrylene used as an ultraviolet filter in cosmetics. *J. Eur. Acad. Dermatology Venereol.* **33**, 25–33 (2019).
15. Rigano, L. & Lionetti, N. Nanobiomaterials in galenic formulations and cosmetics. in *Nanobiomaterials in Galenic Formulations and Cosmetics* 121–148 (Elsevier, 2016). doi:10.1016/B978-0-323-42868-2.00006-1.
16. Bennat & Müller-Goymann. Skin penetration and stabilization of formulations containing microfine titanium dioxide as physical UV filter. *Int. J. Cosmet. Sci.* **22**, 271–283 (2000).
17. Smijs, T. & Pavel. Titanium dioxide and zinc oxide nanoparticles in sunscreens: focus on their safety and effectiveness. *Nanotechnol. Sci. Appl.* 95 (2011) doi:10.2147/NSA.S19419.
18. Monteiro-Riviere, N. A. *et al.* Safety Evaluation of Sunscreen Formulations Containing Titanium Dioxide and Zinc Oxide Nanoparticles in UVB Sunburned Skin: An In Vitro and In Vivo Study. *Toxicol. Sci.* **123**, 264–280 (2011).
19. de Sá, R. G. *et al.* Photoprotective activity of zirconia nanoparticles. *Colloids Surfaces B Biointerfaces* **202**, 111636 (2021).
20. Osmond, M. J. & Mccall, M. J. Zinc oxide nanoparticles in modern sunscreens: An analysis of potential exposure and hazard. *Nanotoxicology* **4**, 15–41 (2010).
21. Gulson, B. *et al.* Small Amounts of Zinc from Zinc Oxide Particles in Sunscreens Applied Outdoors Are Absorbed through Human Skin. *Toxicol. Sci.* **118**, 140–149 (2010).
22. Millington, K. R., Osmond, M. J. & McCall, M. J. Detecting free radicals in sunscreens exposed to UVA radiation using chemiluminescence. *J. Photochem. Photobiol. B Biol.* **133**, 27–38 (2014).
23. Lewicka, Z. A., Yu, W. W., Oliva, B. L., Contreras, E. Q. & Colvin, V. L. Photochemical behavior of nanoscale TiO2 and ZnO sunscreen ingredients. *J. Photochem.*

Photobiol. A Chem. **263**, 24–33 (2013).

24. Tucci, P. *et al.* Metabolic effects of TiO2 nanoparticles, a common component of sunscreens and cosmetics, on human keratinocytes. *Cell Death Dis.* **4**, e549–e549 (2013).
25. Nery, É. M., Martinez, R. M., Velasco, M. V. R. & Baby, A. R. A short review of alternative ingredients and technologies of inorganic UV filters. *J. Cosmet. Dermatol.* **20**, 1061–1065 (2021).
26. Pal, A., Hadagalli, K., Bhat, P., Goel, V. & Mandal, S. Hydroxyapatite—a promising sunscreen filter. *J. Aust. Ceram. Soc.* **56**, 345–351 (2020).
27. Piccirillo, C. *et al.* A hydroxyapatite–Fe 2 O 3 based material of natural origin as an active sunscreen filter. *J. Mater. Chem. B* **2**, 5999–6009 (2014).
28. Cunha, C. S. *et al.* Films of chitosan and natural modified hydroxyapatite as effective UV-protecting, biocompatible and antibacterial wound dressings. *Int. J. Biol. Macromol.* **159**, 1177–1185 (2020).
29. de Araujo, T. S., de Souza, S. O. & de Sousa, E. M. B. Effect of Zn 2+ , Fe 3+ and Cr 3+ addition to hydroxyapatite for its application as an active constituent of sunscreens. *J. Phys. Conf. Ser.* **249**, 012012 (2010).
30. de Araujo, T. S., de Souza, S. O., Miyakawa, W. & de Sousa, E. M. B. Phosphates nanoparticles doped with zinc and manganese for sunscreens. *Mater. Chem. Phys.* **124**, 1071–1076 (2010).
31. Rozaini, M. Z. H., Hamzah, H., Mohtar, N. F., Razali, M. H. & Ibrahim, N. H. Characterization of Photoprotective Hydroxiapatite from Fringescale sardinella (Valenciennes, 1847) Bones as Natural Sunscreen for Cosmeceutical Treatments. *Key Eng. Mater.* **792**, 67–73 (2018).
32. Helmi Rozaini, M. Z. *et al.* Calcium Hydroxyapatite-Based Marine Origin: Novel Sunscreen Materials for Cosmeceutical Treatments. *Orient. J. Chem.* **34**, 2770–2776 (2018).
33. Ghazali, S. R., Rosli, N. H., Hassan, L. S., Helmi Rozaini, M. Z. & Hamzah, H. Biocompatibility of Hydroxyapatite (HAp) derived from clamshell as active ingredients in sunscreen product. *IOP Conf. Ser. Earth Environ. Sci.* **646**, 012059 (2021).

34. Pyo, E., Kim, Y., Park, J. B. & Kwon, K.-Y. A Silver-doped Hydroxyapatite for an Active Sunscreen Material. *Bull. Korean Chem. Soc.* **37**, 1395–1396 (2016).

35. Carella, F., Degli Esposti, L., Adamiano, A. & Iafisco, M. The Use of Calcium Phosphates in Cosmetics, State of the Art and Future Perspectives. *Materials (Basel).* **14**, 6398 (2021).

36. Amin, R. M., Elfeky, S. A., Verwanger, T. & Krammer, B. A new biocompatible nanocomposite as a promising constituent of sunscreens. *Mater. Sci. Eng. C* **63**, 46–51 (2016).

37. Morsy, R., Ali, S. S. & El-Shetehy, M. Development of hydroxyapatite-chitosan gel sunscreen combating clinical multidrug-resistant bacteria. *J. Mol. Struct.* **1143**, 251–258 (2017).

38. Piccirillo, C. *et al.* Extraction and characterisation of apatite- and tricalcium phosphate-based materials from cod fish bones. *Mater. Sci. Eng. C* **33**, 103–110 (2013).

39. Coelho, T. M. *et al.* Characterization of natural nanostructured hydroxyapatite obtained from the bones of Brazilian river fish. *J. Appl. Phys.* **100**, 094312 (2006).

40. Hadagalli, K. *et al.* Effect of Fe 3+ substitution on the structural modification and band structure modulated UV absorption of hydroxyapatite. *Int. J. Appl. Ceram. Technol.* **18**, 332–344 (2021).

41. C. Teixeira, M. A. *et al.* Effect of preparation and processing conditions on UV absorbing properties of hydroxyapatite-Fe2O3 sunscreen. *Mater. Sci. Eng. C* **71**, 141–149 (2017).

42. Piccirillo, C. *et al.* Increased <scp>UV</scp> absorption properties of natural hydroxyapatite-based sunscreen through laser ablation modification in liquid. *J. Am. Ceram. Soc.* **102**, 3163–3174 (2019).

43. Nishikawa, H. Thermal behavior of hydroxyapatite in structural and spectrophotometric characteristics. *Mater. Lett.* **50**, 364–370 (2001).

44. Gomes, S., Kaur, A., Grenèche, J.-M., Nedelec, J.-M. & Renaudin, G. Atomic scale modeling of iron-doped biphasic calcium phosphate bioceramics. *Acta Biomater.* **50**, 78–88 (2017).

45. Gomes, S., Nedelec, J.-M. & Renaudin, G. On the effect of temperature on the

insertion of zinc into hydroxyapatite. *Acta Biomater.* **8**, 1180–1189 (2012).

46. Prasad, A., Devendar, B., Sankar, M. R. & Robi, P. S. Micro-Scratch Based Tribological Characterization of Hydroxyapatite (HAp) Fabricated through Fish Scales. *Mater. Today Proc.* **2**, 1216–1224 (2015).
47. Ideia, P. *et al.* Extraction and characterization of hydroxyapatite-based materials from grey triggerfish skin and black scabbardfish bones. *Int. J. Appl. Ceram. Technol.* **18**, 235–243 (2021).
48. Iafisco, M., Ruffini, A., Adamiano, A., Sprio, S. & Tampieri, A. Biomimetic magnesium–carbonate-apatite nanocrystals endowed with strontium ions as anti-osteoporotic trigger. *Mater. Sci. Eng. C* **35**, 212–219 (2014).
49. Sofronia, A. M., Baies, R., Anghel, E. M., Marinescu, C. A. & Tanasescu, S. Thermal and structural characterization of synthetic and natural nanocrystalline hydroxyapatite. *Mater. Sci. Eng. C* **43**, 153–163 (2014).
50. Pal, A. *et al.* Synthesis of hydroxyapatite from Lates calcarifer fish bone for biomedical applications. *Mater. Lett.* **203**, 89–92 (2017).
51. Rahman, Q. I., Ahmad, M., Misra, S. K. & Lohani, M. Effective photocatalytic degradation of rhodamine B dye by ZnO nanoparticles. *Mater. Lett.* **91**, 170–174 (2013).
52. Giahi, M., Saadat Niavol, S., Taghavi, H. & Meskinfam, M. Synthesis and characterization of ZnO–TiO2 nanopowders doped with fe via sol–gel method and their application in photocatalytic degradation of anionic surfactant. *Russ. J. Phys. Chem. A* **89**, 2432–2437 (2015).
53. Reinosa, J. J., Docio, C. M. Á., Ramírez, V. Z. & Lozano, J. F. F. Hierarchical nano ZnO-micro TiO2 composites: High UV protection yield lowering photodegradation in sunscreens. *Ceram. Int.* **44**, 2827–2834 (2018).

6. CaPs for agricultural applications

6.1. Introduction

In this chapter the preparation of CaPs obtained from fish bones for agricultural application as fertilizers and as biostimulants for plants was reported. The use of CaPs for this kind of applications has recently gained attention as these materials are widely renowned for their intrinsic biocompatibility and biodegradability,[1,2] so their use does not raise any safety issue. Moreover, CaPs contain phosphorous (P), which is a primary nutrient for plants and a key element in crop fertilization. On the other hand, P availability on the planet is diminishing due to its extensive extraction from finite ore deposits to meet the world fertilizer demand.[3] Moreover, the mining of P directly induced adverse effects on the environment, as it involves both the release of huge amounts of acids used to obtain P from phosphorite (the rock extracted from the mine) and of harmful wastes, mostly toxic metals, and radioactive elements.[4] This led toward numerous negative effects on water and air quality, water consumption, local hydrology, and human health. Therefore, it is of fundamental importance to develop the circular economy of this element and enlarge its pool of resources with alternative and renewable ones, such as food by-products. In this respect, fish bone is an abundant and P-rich by-product from fish processing, containing up to the 18 wt.% of P in the form of CaP.[5] Even in developed countries the transformation of fish bone into marketable products is neglected and is usually considered unprofitable.[6,7] Many works have recently encouraged the recovery of valuable chemicals from it, such as collagen, fatty acids and HA that can find use in several fields, like nutrition, agriculture, chemistry and regenerative medicine.[8–10] The valorisation of fish bones could also be a key to generate new incomes and increase the adaptive capacity of fishing communities of least developed countries (LDCs), even facilitating their transition towards aquaculture. Several techniques for fish waste processing into value-added products are largely applied at the industrial scale in developed countries, where fish by-products are converted into biogas, animal feed, chemical building blocks, bioplastics and bio stimulants.[11] In LDCs the application of most of these conversion processes is difficult as they typically involve the use of chemicals and industrial facilities such as air dryer, reaction vessels, and grinding machine.

Part of the content of this chapter was published as “F. Carella, M. Seck, et al. Thermal conversion of fish bones into fertilizers and biostimulants for plant growth – A low tech valorization process for the development of circular economy in least developed countries”

In this view, the aim of the work reported in this chapter, was focused on the development of a simple and easy scalable thermal process for the conversion of Sardinella aurita fish bones, promoting the circular economy in LDCs. This obtained materials are designed to be used as "drug delivery systems" for plant, in which the drug is P. Indeed, the thermal conversion of fish bones leads to the production of CaP-based fertilizers and bio stimulants for plant growth.

As temperatures above 1000 °C could be difficult to achieve in LDCs,[12] the process was performed at 300 °C, 600 °C and 900 °C. Moreover, the environmental benefits deriving from the application of this kind of materials have been reported by several studies in the literature.[13–16] The only difference between these biochar-based materials and the one reported in the present chapter, consists in the production. Indeed, CaP-based materials were carried out not by pyrolysis, but in an oxidizing environment.

The obtained CaPs were characterized from the physical-chemical point of view and then tested as biostimulants for seed germination on Lepidium sativum, as fertilizer for the growth of Zea mais seedlings and as bio stimulants for the elongation of Zea mais coleoptiles. Finally, an analysis on the environmental and economic aspects related to the transformation process was performed to confirm its large-scale applicability in LDCs.

6.2. Materials and methods

6.2.1. Materials

4-(2-Hydroxyethyl) piperazine-1-ethanesulfonic acid ($C_8H_{18}N_2O_4S$, anhydrous, ≥ 99.5% pure), ultrapure nitric acid (HNO_3, ≥ 70 wt% in water, ICP-OES and ICP-MS purity), sodium acetate (CH_3COONa, ReagentPlus®, ≥ 99.0% pure) and acetic acid (CH_3COOH, ReagentPlus®, ≥ 99.0% pure) were supplied by Sigma-Aldrich. All the solutions were prepared with ultrapure water (0.22 μS, 25 °C, MilliQ, Millipore). Furthermore, Sardinella aurita by-products were collected by a women cooperative that deals with filleting fish in the artisanal port of Saint louis in Senegal. Subsequently, bones were manually divided from organic phases, washed under running water and sundried for 48 h.

6.2.2. Fish bone processing

The conversion of fish bones into the final products was performed by a thermal treatment. In particular, fish bones were heated in air at the final temperatures of 300,

600 and 900 °C, and the obtained samples were named SB300, SB600 and SB900, respectively (Figure 6.1). The thermal ramp of 100 °C h^{-1} was followed by a one-hour isotherm at the final temperature. Once thermal treated, powders were cooled at room temperature, grinded and sieved at 50 µm to achieve a uniform granulometry.

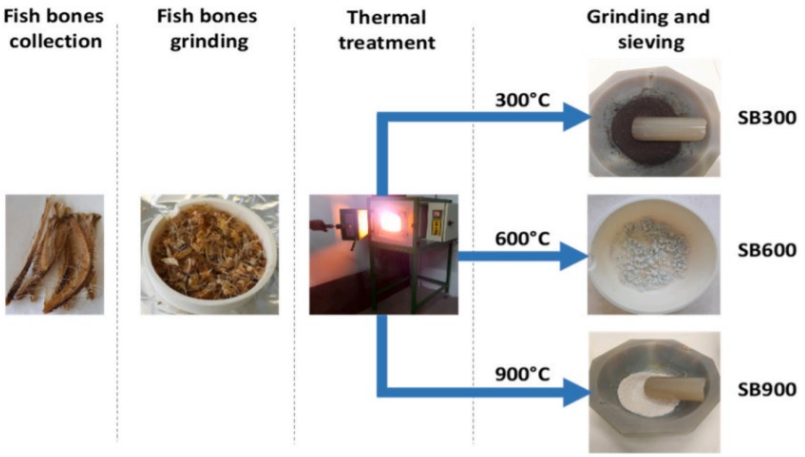

Figure 6.1 - Schematic representation of the process used to convert fish bones into the samples.

The obtained materials were analyzed to evaluate their morphology with SEM microscope, and their physical and chemical properties with FT-IR, TGA, DLS, ICP, XRD and SSA.

Concerning the ICP analysis, the sample preparation method was slightly changed for SB300 sample because of the high organic phase in it. In particular, SB300 was dissolved by microwave assisted digestion. Briefly, 20 mg of the sample was added with 5 mL of HNO_3 (70,0 wt.%) and 1 mL of H_2O_2 (35,0 wt.%) in a PTFE sealed vessel located in a High-Performance Microwave Digestion (MLS 1200 Mega - Milestone, Bergamo, Italy) oven. The digestion program was made by the following steps: 2 min at 250 W, 2 min at 0 W, 6 min at 250 W, 5 min at 400 W, and 5 min at 600 W. Dissolved samples were finally cooled at room temperature and added with ultrapure water up to 100 mL.

6.2.3. CHN analysis

Total nitrogen (N_{tot}) and carbon (C_{tot}) contents of SB300, SB600 e SB900 were determined by dry combustion of powdered samples using a CHN elemental analyzer (Carlo Erba Instruments, Mod 1500, series 2).

6.2.4. Samples release in water

The release of calcium and phosphate from the samples was performed in water. Briefly, 10 mg of each sample was suspended in 20 mL of deionized water at 25°C and at pH 6.5 to simulate the conditions used for *in vitro* and *in vivo* tests described below. At scheduled time points (30min, 1h, 2h, 3h, 4h, 6h, 24h, 48h, 72h and 96h), supernatants were collected by centrifugation at 10.000 rpm for 5 min, and the resulting pellets were resuspended in the same amount of fresh deionized water. The supernatants were filtered with Fluoropore PTFE filters with 0.22 µm pore size. Subsequently, 3 mL of HNO_3 were added to each supernatant, and then the samples were placed in a water bath sonicator at 37 °C for 30 min prior to ICP analysis.

6.2.5. Phytotoxicity test

The phytotoxicity tests were conducted by Institute for Bioeconomy (IBE-CNR) team. In particular, samples were suspended in water at two concentrations (50 wt.% and 75 wt.%), and distilled water was used as the control. The test is based on the determination of the germination and growth potential effect of Lepidium sativum seeds in terms of germination index (GI). GI was calculated according to Equation 6.1:

$$GI(\%) = 100 * \frac{N_{treat} * L_{treat}}{N_{ctrl(72h)} * L_{ctrl(72h)}} \qquad \text{Equation 6.1}$$

where N_{treat} was the number of germinated seeds in the treatment, L_{treat} was the mean length (mm) of the radicles in the treatment, and $N_{ctrl(72\,h)}$ and $L_{ctrl(72\,h)}$ were the number of germinated seeds and the mean length (mm) of the radicles in the control at the end of the experiment (after 72 h), respectively. Firstly, seeds of *Lepidium sativum L.* were examined under an optical microscope and manually selected to remove discoloured or damaged ones. Subsequently, for each sample, including the control, were prepared five Petri dishes (Ø 9 mm) with filter paper on the bottom of them. 10 seeds of Lepidium sativum L. previously soaked in distilled water for 1 h were placed in each Petri dish. After, they were watered with 5 mL of the respective treatment solution and incubated at 22 °C for 3 days. The number of germinated seeds and the radicle length was measured after certain time points (0h, 6h, 9h, 12h, 24h and 72 h).

6.2.6. Growth doses effect test

A pot experiment on corn seedlings (Zea mays) was performed by Institute for Bioeconomy (IBE-CNR) team to test samples potential as phosphorous-based fertilizers. Corn seedlings were grown in a not calcareous sandy soil composed by a pH of 6.68 and a content of C_{tot} 0.44 wt.% and N_{tot} 0.08 wt.% mixed with samples at four different proportions (1.0 wt.%, 5.0 wt.%, 10.0 wt.%, and 15.0 wt.%). Untreated soil was used as control. For each mixture, 7 replicas were prepared in 125 mL jars. The experimentation took place in growth chamber in a controlled environment (25 °C with 12 h light and dark cycles) for 3 weeks. At harvest time, each plant sample was dried at 60 °C for 48 h and their Growth index (Gm) was calculated based on the dry weight of the biomass using Equation 6.2:

$$Gm(\%) = \frac{G_C}{G_t} * 100 \qquad \text{Equation 6.2}$$

where Gc is the average dry aboveground biomass of each treatment, and Gt is the average dry aboveground biomass of the control, both expressed in grams.

6.2.7. Corn coleoptile elongation rate test

The corn coleoptile elongation rate test was also performed by Institute for Bioeconomy (IBE-CNR) team to evaluate the biostimulant effect of the samples. Corn seedlings were grown in the dark for one week until coleoptiles were 2–3 cm long. The apical part (3–4 mm) of the coleoptiles was removed and a segment of 2 cm was cut from the remaining part. These segments were placed into 10 cm petri dishes containing 20 mL of test solutions of each sample at different concentrations (1.37 mg L^{-1}, 5.5 mg L^{-1} and 11.0 mg L^{-1}) named hereafter solution A, B and C, respectively. Deionized water was used as the control, and a water solution at 1.75 mg L^{-1} of a well-known bio stimulant, inodole-3-aceticacid (IAA), was used as reference. Four replicates were performed for each treatment, the experimental unit consisting of 36 petri dishes for just as many coleoptiles. Corn coleoptile length was measured after 48 h of dark.

6.3. Results and discussion

6.3.1. CaPs from natural source characterization

The materials obtained from the calcination of S. aurita bones were analysed by XRD (Figure 6.2), which indicates the presence of HA as the main phase, with very different degree of crystallinity among the samples.

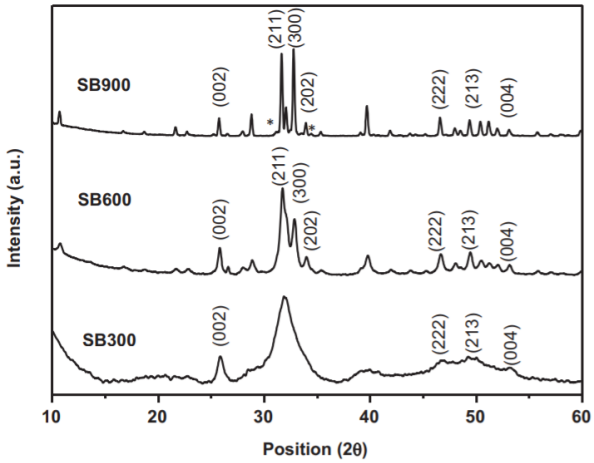

Figure 6.2 - XRD spectra of samples SB300, SB600 and SB900. Main HA peaks are numbered by their relative miller index. Peaks ascribed to β-TCP are labeled by an asterisk (*).

Figure 6.2 shows XRD pattern of SB300, SB600 and SB 900. In particular, SB300 spectra is featured by broad, diffuse peak in the 2θ range from 28° to 35°, supporting the occurrence of a very poorly crystalline HA phase. Moreover, the broad peak centred at about 32° results from the overlap of three peaks (31.77°, 32.19°, and 32.90°) corresponding to the HA planes (211), (112) and (300), respectively. The intensity of the background noise collected in the SB300 XRD pattern is higher respect to the other samples, probably due to the presence of organic matter (e.g. black carbon or char). The SB600 spectrum, instead, has peaks located at 2θ values of 25.9°, 31.7°, 32.9°, 34.0°, 46.7°, and 49.5° corresponding to the (002), (211), (300), (202), (222), and (213) planes of HA, respectively. Diffraction peaks are broad and poorly defined, indicating the presence of nanocrystals with reduced crystal domains and crystalline order. However, the SB600 pattern is characterized by sharper peaks than SB300 spectrum, which is indicative of a higher crystallinity of the material. Finally, the SB900 XRD spectrum is characterized by sharp and resolved peaks ascribable to highly crystalline HA as the main phase, and by much less intense peaks ascribable to β-TCP as the secondary phase. The ratio among peaks intensities is similar to those found in other samples, with the

exception of the peak corresponding to plane (300). Indeed, the intensity of this reflection is higher than plane (211), which is the main reflection of standard HA. This is probably due to the superimposition of the β-TCP reflection corresponding to plane (306).
Moreover, ATR analysis performed on the samples confirms the presence of HA as the dominant phase in all the samples (Figure 6.3).

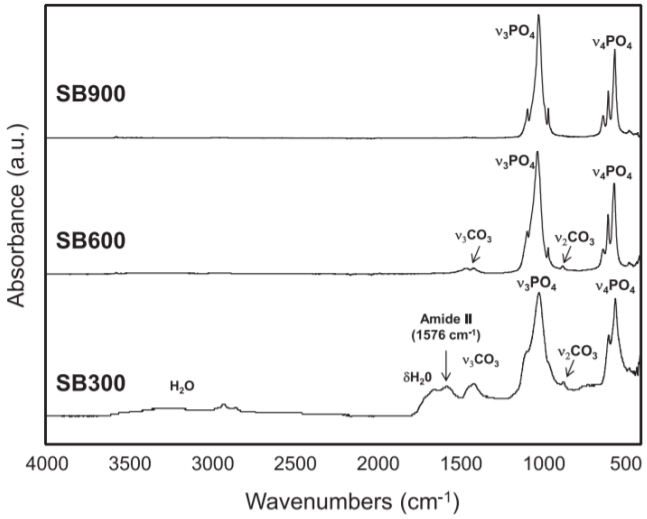

Figure 6.3 - ATR spectra of SB900, SB600 and SB300.

Figure 6.3 highlights that the spectrum of SB300 is the only one characterized by a broad peak at 3400 cm^{-1} and a shoulder at 1640 cm^{-1}, ascribable as H_2O. The major difference between ATR spectra consists in the intensity of the bands at 1448 cm^{-1} and 1412 cm^{-1}, which are ascribed to the asymmetric stretching vibration mode of C–O bonds of carbonate ions. In particular, they are much higher for samples SB300 respect to sample SB600 and are absent in SB900. Furthermore, the out-of-plane bending (ν_2) of the carbonate ion at 880 cm^{-1} has the same relative intensity in the SB300 and SB600 sample, while it is absent in SB900 sample. Lastly, SB300 IR-spectrum is the only one featuring a band at 1576 cm^{-1} due to amide II stretching of C–N and bending of N–H bonds, that is indicative of the residual collagen molecules still present after the thermal process.[17,18] In general, the most intense IR band in all the material ATR spectra is located in the 995–1120 cm^{-1} range, corresponding to the triply degenerated asymmetric stretching vibration mode (ν_3) of the phosphate tetrahedron. Furthermore, it is possible to notice that the triply degenerated bending mode (ν_4) of the PO_4 in the 550–650 cm^{-1} range adopts a sharper triplet characteristic, and thus an increase crystallinity degree, going from sample SB300 to SB600, and finally to SB900.

Based on the XRD, Rietveld and ATR analysis performed on the samples, it was calculated the crystallinity index (C), the HA crystals domain and the infra-red splitting factor (IR-CF) (Table 6.1). In particular, the C and the HA crystals domain were calculated following the Equation 2.3 and the Equation 2.4, respectively, both reported in Chapter 2. The IR-CF, instead, was calculated from the IR spectra by adding the measured intensities of the two $v_4(PO_4)_3$ vibration bands at 565 and 605 cm^{-1} in the absorbance mode and dividing their sum by the intensity of the valley between these absorption bands and the baseline, after a baseline correction between 1200 and 250 cm^{-1}.[19] The C calculation and the determination of phase composition by Rietveld refinement were not possible for SB300 sample because of its very poor crystallinity, resulting in weak and broad peaks in its XRD spectra.

Table 6.1 - Phase composition determined by Rietveld analysis, crystallinity index and IR-CF calculated on all the samples.

Sample	C (%)	HA (wt.%)	β-TCP (wt.%)	$D(002)_{HA}$ (nm)	$D(310)_{HA}$ (nm)	IR-CF[a] (a.u.)
SB300	< 5[b]	n.d.[b]	n.d.	30.3 ± 1.0	6.3 ± 0.5	3.0 ± 0.3
SB600	50.0 ± 2.0	98.9 ± 1.0	n.d.	49.6 ± 1.5	43.4 ± 1.2	5.5 ± 0.5
SB900	60.0 ± 3.0	95.0 ± 1.0	5.0 ± 2.0	151.0 ± 3.0	93.8 ± 2.3	7.6 ± 0.6

[a] Data from FT-IR analysis. Values are reported as mean ± standard deviation of n = 3 measurements.

[b] Crystallinity index and HA (wt. %) were not measurable for SB300.

As visible from Table 6.1, C values show that the higher is the temperature of fish bone transformation treatment, the higher is the crystallinity of the obtained CaPs. The obtained results confirm those reported by Glæsner et al., which produced and studied bone chars by thermal treatment of bone meal from a slaughterhouse.[13] Moreover, Rietveld analysis revealed that SB600 consists of HA as the only crystalline phase, while SB900 is characterized by crystalline HA as the main phase and by β-TCP as its secondary phase. Furthermore, Table 6.1 shows that HA crystals domain sizes increased with increasing temperature of the thermal treatment. Indeed, SB300 is characterized by very small and needle-like HA nano-crystallites elongated on the c-axis, while SB600 shows a growth along the (310) direction obtaining almost spherical and more isotropic crystallites of nanometric dimensions. A further increase of temperature to 900°C leads to the formation of much larger crystallites elongated on the c-axis, even though with a

smaller aspect ratio than SB300 crystallites. Eventually, the IR-CF values confirm the results obtained from XRD data and previous calculation.

The chemical composition of the samples was evaluated by ICP-OES, CHN and TGA analysis, which are reported in Table 6.2.

Table 6.2 - Samples composition determined by ICP[(a)], CHN[(b)] analysis and TGA[(c)]. Values are reported as mean ± standard deviation of n = 3 replicates.

	SB300	**SB600**	**SB900**
Ca (wt.%) [(a)]	17.1 ± 1.2	34.7 ± 1.4	38.8 ± 1.3
P (wt.%) [(a)]	8.3 ± 0.4	16.7 ± 0.6	18.8 ± 0.5
Ca/P [(a)]	1.59 ± 0.10	1.60 ± 0.20	1.54 ± 0.20
N_{tot} [(b)]	5.0 ± 0.1	0.1 ± 0.1	-
C_{tot} [(b)]	29.4 ± 0.6	3.1 ± 0.1	0.1 ± 0.1
H_2O content (wt.%) [(c)]	2.7 ± 0.2	0.9 ± 0.1	0.5 ± 0.1
Organic matter (wt.%) [(c)]	49.4 ± 2.0	0.4 ± 0.1	0.1 ± 0.1
Inorganic Carbon (wt.%) [(c)]	5.0 ± 1.0	2.7 ± 0.2	0.5 ± 0.1
Residual mass (wt.%) [(c)]	42.8 ± 3.0	95.9 ± 2.0	98.9 ± 1.5

The data showed in Table 6.2 confirm the previous analysis. Indeed, it is shown that SB600 and SB900 sample are mainly composed of CaP, while in SB300 sample the amount of Ca and P detected are much lower, due to the organic phase remained after the thermal treatment. Moreover, Ca/P ratios of the samples are lower than the HA stoichiometric value of 1.67, as often found in Ca-deficient HAs obtained from natural sources.[20–22] In particular, Ca/P ratio of SB900 is the lowest probably because of the presence of a β-TCP secondary phase, which is characterized by a lower Ca/P ratio respect to HA.

Furthermore, the results of the CHN analysis show the high content of organic matter in SB300 sample, confirming IR analysis. Indeed, this sample highlights a higher content of carbon and nitrogen than the other two samples. Eventually, since sulphur is present with very low concentrations inside fish bones (0.61 wt.% of the collagen) its contribution to samples composition can be neglected.[23]

Concerning the TGA analysis, the amount of structural water, organic matter, and inorganic carbon for each sample was quantified by the thermal weight losses in the temperature ranges: 100 - 270 °C, 270 - 700 °C and 700 - 1100 °C, respectively. The residual mass was calculated as the mass of the samples at 1100 °C. TGA results confirm

the other analysis carried out on SB300 sample, showing that this is composed by CaP for 42.8 wt.%, organic matter for 49.4 wt.%, and a small amount of water. SB300 sample is also featured by a thermal loss in the range between 700 °C and 1100 °C of 5.0 wt.%, which is correlated to the typical carbonate content of fish bone CaP.[7,24] SB600 and SB900 samples, instead, are both composed by a high mineral content (> 95 wt.%), and very small amounts of water and organic matter. The only difference among these two samples is the weight loss during the decarboxylation of the HA, which is higher for SB600 than SB900. This can be due to the almost completed decarboxylation at 900°C for SB900 sample.

Afterwards, the morphology of the samples was investigated by FEG-SEM (Figure 6.4).

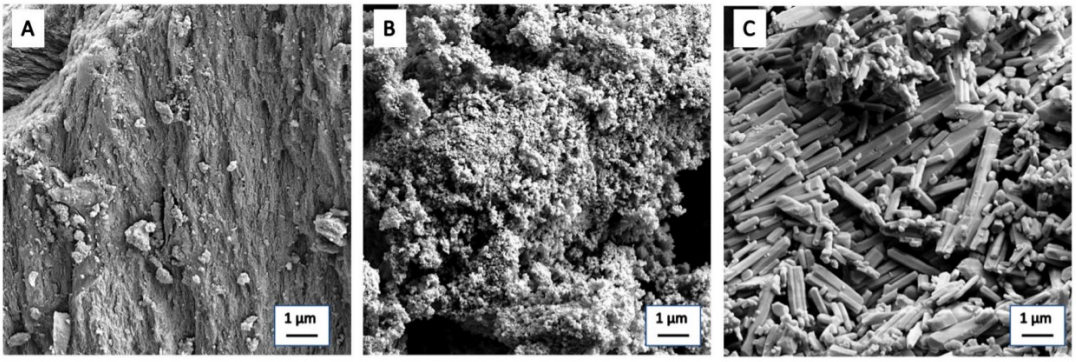

Figure 6.4 - From left to right, SEM images of sample SB300 (A), SB600 (B) and SB900 (C).

The Figure 6.4 confirm the progressive crystal growth of the material with increasing calcination temperature of fish bone. SB300 sample (Figure 6.4A) show a high content of char associated to the mineral part. Indeed, it is possible to observe a morphology resembling the bone tissue, with an aligned arrangement of the char corresponding to the oriented structure of the original fish bone. On the other hand, in SB600 (Figure 6.4B) and SB900 (Figure 6.4C) samples the original bone organic matrix was completely removed by the thermal treatment, making particles size and morphology easier to analyse. In particular, SB600 is characterized by small and round shaped HA particles with nanometric size in the range between 50 and 100 nm, while SB900 consists of more regular and coarser rod like particles with micrometric size in the range between 0.2 and 2 µm.

Subsequently, the hydrodynamic diameter distribution and the electric double layer on the surface of particles were determined by DLS. Moreover, the specific surface area

(SSA) of the particles was evaluated by BET. The resulting Z-average, ζ-potential and SSA are reported for each sample in Table 6.3.

Table 6.3 – DLS and BET results.

Sample	Zeta-average (nm)	ZP (mV)	SSA (m^2g^{-1})
SB300	n.d.	n.d.	46.9 ± 1.0
SB600	176 ± 5	-15.4 ± 1.0	6.7 ± 0.2
SB900	529 ± 19	-19.2 ± 0.5	5.3 ± 0.2

For SB300, DLS analysis could not provide any information due to the very fast precipitation of the particles in water. Moreover, the material has a higher SSA value than the other two samples, that is in line with what is typically reported for bone char obtained at low temperature.[25] However, concerning the other two samples, Z-averages of SB600 is smaller than SB900, while the ZP of SB900 particles is slightly more negative than SB600 particles.

The chemical stability of the samples was evaluated as the release of PO_4^{3-} and Ca^{2+} from the materials in contact with deionized water, that can be considered as an index of calcium phosphate dissolution (Figure 6.5).

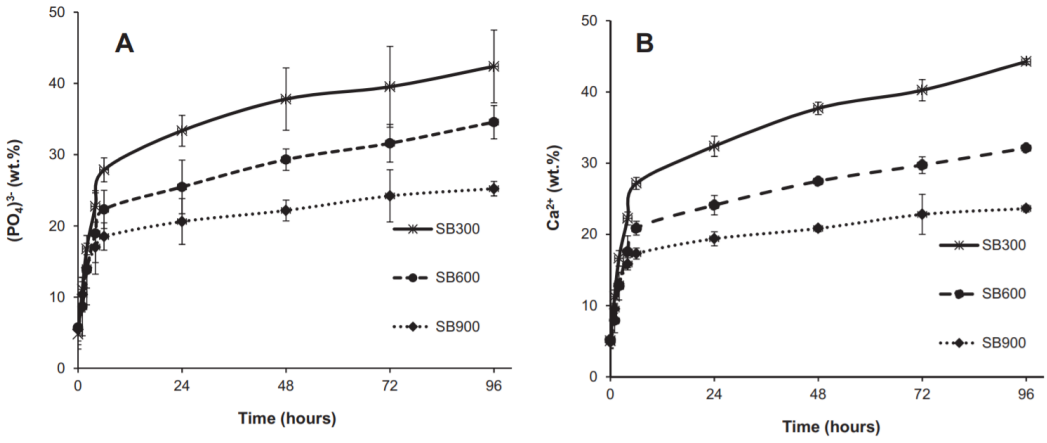

Figure 6.5 - Release curves of phosphate (A) and calcium (B) ions in water from SB300, SB600 and SB900, up to 4 days (96 h) expressed as the percentage of phosphate and calcium of the samples released in water. Values are reported as mean ± standard deviation of n = 3 replicates.

From Figure 6.5 it is possible to notice that the release of calcium and phosphorous follows the same trend with almost identical percentages of dissolution. As an example, the releases of Ca^{2+} after 96 h are equal to 44.3 %, 32.1 % and 23.6 %, while those of PO_4^{3-} at the same time point are equal to 42.4 %, 34.6 % and 25.2 % for SB300, SB600 and

SB900, respectively. Samples dissolution is much faster in the first 24 h, with a burst release in the first 4 h, after which the slope of the release curves starts to decrease. As expected, samples stability increases with the increase of calcination temperature. At day 4, more than the 40 % of calcium and phosphorous in SB300 is released, while the percentages for SB900 is around the 22 %. These release differences correspond to the crystallinity of the samples. Indeed, the lowest one is ascribable to SB300, which is composed by very poorly crystalline HA nanoparticles. On the other hand, the highest one is ascribable to SB900, which consists of larger and crystalline rod-like particles.

6.3.2. *In vitro* and *in vivo* analysis on CaPs from natural source

After the physical-chemical characterization, samples were tested as biostimulants and as fertilizers on plants. First, it was evaluated the effect of the materials on Lepidium sativum L. seeds germination (Figure 6.6).

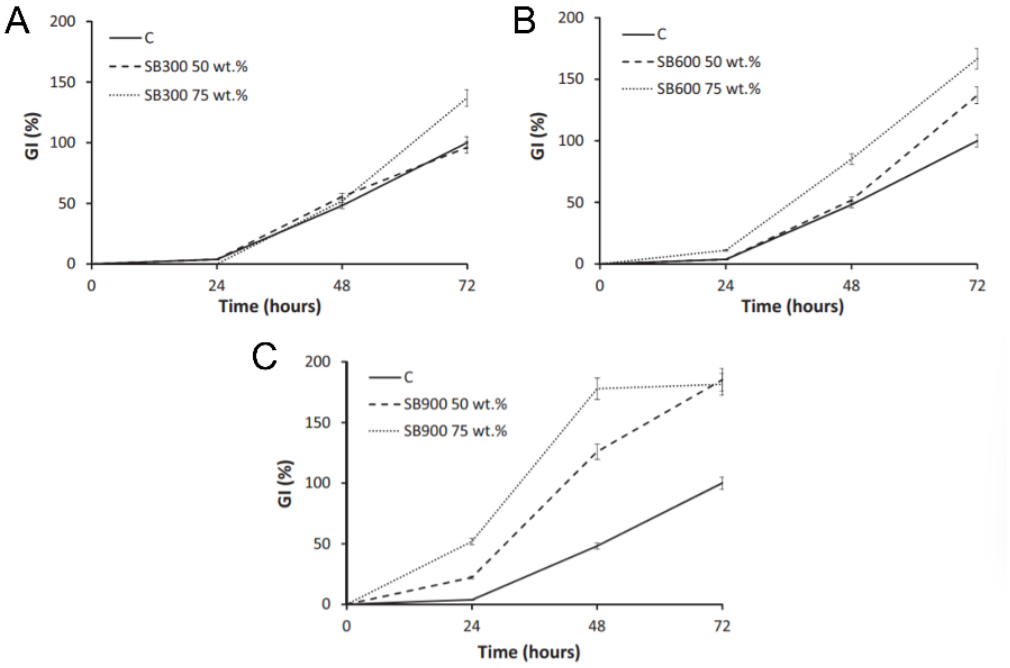

Figure 6.6 - Results of the germination tests on Lepidium sativum L. seeds treated with water (control) and with two different concentrations (50 wt.% and 75 wt.%) of SB300 (A), SB600 (B) and SB900 (C).

From Figure 6.6 it is possible to notice that all samples sorted a positive effect on seed germination in a dose dependent manner, which agree with a previous work focused on tomato seeds and plants treated with synthetic HA nanoparticles.[26] Interestingly, the stimulating effect was directly proportional to the temperature of fish bones treatment. Indeed, seeds treated with SB900 have both fast germination and radicles growth, with

the highest GI which almost double the control (180 %) for the high-dose treatment already after 48 h. The same GI value was reached for seeds treated with the lower dose of SB900 at the end of the experiment (i.e., after 72 h). Germination was slower in the case of seeds treated with SB600. In particular, high levels of GI (175 %) were reached only with high doses and after 72 h. Concerning the lower dose of SB600, a positive effect on seed germination was observed after 72 h, with GI value of 145 %. Similar results were obtained treating seeds with a high dose of SB300. On the other hand, no difference between seeds treated with low dose of SB300 and the control was observed.

Furthermore, the materials were then tested as soil fertilizers on *Z. mais* seedlings (Figure 6.7). As for the germination test, all the materials sort a dose-dependent positive effect on plants growth in terms of dry biomass after 3 weeks.

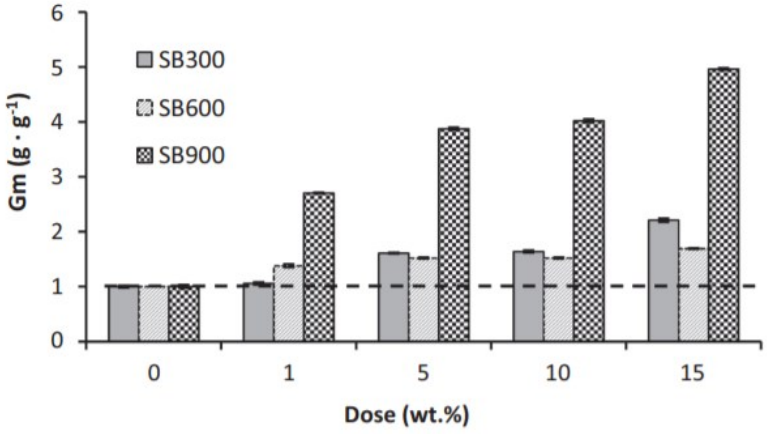

Figure 6.7 - Growth doses effect tests on corn seedlings (Zea mays) grew in not calcareous sandy soil mixed with SB300, SB600 and SB900 at different doses. The black dashed line represents the value of Gm = 1 of the control. Gm values are reported as mean ± standard deviation of n = 7 replicates.

As it is possible to notice from Figure 6.7, SB900 gave the best result since its lowest tested dose (1.0 wt.% in the soil). Indeed, plants dry biomass was more than doubled respect to the control (Gm = 2.8) and it was higher than the Gm values measured for the treatment with SB600 or SB300 at their highest doses. Plants grown in soils with 5.0 wt.% and 10.0 wt.% of SB900 shown a dry biomass 4 times higher than the control, with a Gm of 3.9 and 4.0, respectively. Finally, the dry biomass of plants grown in soils with the highest dose of SB900 was 5 times higher (Gm = 5.0).

A milder fertilizing effect was observed on plants treated with soils mixed with SB300 at 5.0 wt.%, 10.0 wt.% and 15.0 wt.%, while no difference respect to the control can be seen for the lowest tested dose of 1.0 wt.%. Finally, the smallest effect was observed for plants

treated with SB600, whose dry biomass at the end of the experiment was much closer to the control respect to the other samples. Surprisingly, these results show that the highest biomass growth is obtained for plants treated with the least soluble sample (SB900), followed by the treatment with the most soluble one (SB300), and lastly by SB600.

Since the growth dose effect and the samples solubility experiments were carried out at similar pH, P release in water can be seen as an index of the element mobility in the soil. Commonly, CaP performances as fertilizers were considered directly proportional to their capacity to mobilize P in the soil, and hence is inversely proportional to their crystallinity and chemical stability.[27] Contrary to what expected, these results show that there is no correlation between the materials performance as fertilizer, the P release derived from samples dissolution in water and the crystallinity of the sample.

Eventually, the coleoptile elongation rate test was performed on a water suspension of the samples (Figure 6.8).

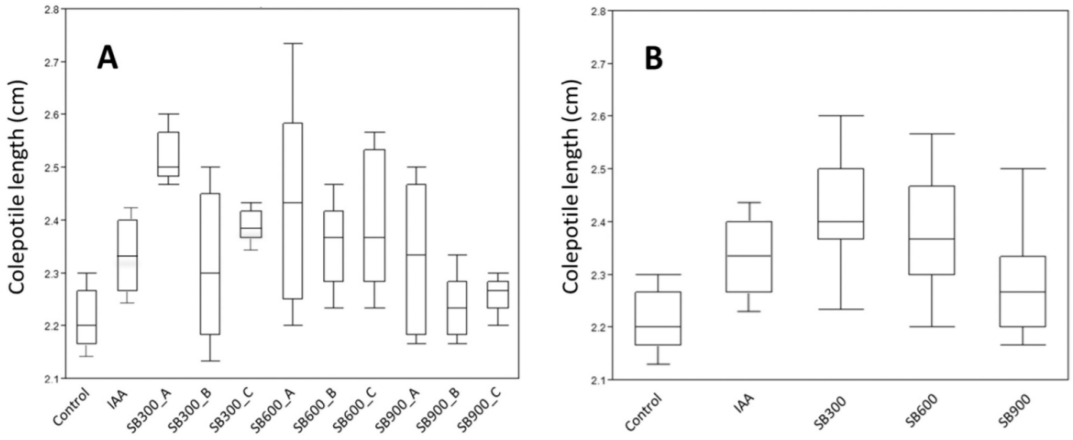

Figure 6.8 - Box plot of corn coleoptile elongation test in water suspensions of each samples at different concentrations (1.37, 5.50 and 11.00 mg L^{-1}) obtaining A, B and C series, respectively. Water was used as control, and a solution of IAA was used as reference. On the left, (A) results are expressed separately for each tested concentration and samples, as the mean and standard deviation of 4 replicates. On the right, (B) results are expressed as the mean and standard deviation of the tests at different concentrations combined together (n = 12).

The results reported in Figure 6.8 showed that SB300 and SB600 samples improve coleoptile elongation at every tested concentration, while SB900 sorted a statistically significant effect respect to the control only at its lowest concentration. Surprisingly, the fastest coleoptile growth was always observed for treatments at the lowest concentration for all the samples, suggesting that the bio stimulation effect was not dose dependent. This was in contrasts with the action of other bio stimulants, like those based

on humic acids, whose effect on coleoptile elongation of Z. mais was reported to be dose dependent.[28] However, it is renowned that other kinds of biostimulants like NPs can sort a dose-independent positive effect on seedling growth and root development in different plant species.[29,30]

6.4. Conclusion

In this chapter, it was explored the potential of a low-tech circular economy approach to the problems of poor adaptive capacity and phosphorous scarcity in LDCs that could be implemented at the community level. It was demonstrated that it is possible to convert fish bone into materials with a higher potential value for the agricultural market by a straightforward and easily scalable thermal process that could be applied at the community level in LDCs. The yield of the S. aurita bones thermal process, here reported, changes with the temperature of treatment. Indeed, it was equal to 71.0 ± 2.1 wt.%, 34.0 ± 1.0 wt.% and 32.0 ± 1.1 wt.% for fish bones treated at 300 °C, 600 °C and 900 °C, respectively. The difference in the yield was due to the increasing amount of organic component burnt in the process. Data showed that the obtained samples were mainly composed of CaP, but SB300 was composed by a different composition. Indeed, the low temperature used in the process had led to a huge remaining organic part in the sample. Furthermore, SB300 and SB600 were composed by HA, while SB900 also contained a small percentage of β-TCP. To sum up the in vitro and in vivo tests, sample SB900 gave the best results among the tested materials in terms of L. sativum seeds stimulation of germination and radicles growth, and in terms of fertilization for Z. mais growth. On the other hand, it gave poor results when used as bio stimulant to improve Z. mais coleoptile elongation. SB600 gave good results as bio stimulant when used to boost seed germination and radicle growth, and to increase corn coleoptile elongation. However, when SB600 was used as soil fertilizer, its effect on corn growth was negligible. Finally, SB300 showed very good potential as corn coleoptile bio stimulant and as corn fertilizer, while its effect on seed germination was negligible respect to those registered for the other two samples.

In future, to improve the bio stimulant effect of these materials, the adsorption of humic substances could be developed, as they are commonly used for this purpose.

However, these results demonstrated that this process could be environmental and economically important both for the planet and for LCDs. Indeed, the large-scale application of this process could sort several positive effects in these countries, as: (i) it will empower local food production systems and will foster the development of a circular economy of phosphorous, (ii) it will decrease the dependence of LDCs agriculture from phosphate importation, and (iii) it will increase the adaptive capacity of LDCs local communities by increasing their economic income.

References:

1. Sprio, S. *et al.* Bio-inspired assembling/mineralization process as a flexible approach to develop new smart scaffolds for the regeneration of complex anatomical regions. *J. Eur. Ceram. Soc.* **36**, 2857–2867 (2016).
2. Tampieri, A. *et al.* Hydroxyapatite: From Nanocrystals to Hybrid Nanocomposites for Regenerative Medicine. in *Handbook of Bioceramics and Biocomposites* 119–144 (Springer International Publishing, 2016). doi:10.1007/978-3-319-12460-5_6.
3. Gilbert, N. Environment: The disappearing nutrient. *Nature* **461**, 716–718 (2009).
4. Reta, G. *et al.* Environmental impact of phosphate mining and beneficiation: review. *Int. J. Hydrol.* **2**, (2018).
5. *Phosphorus Recovery and Recycling*. (Springer Singapore, 2019). doi:10.1007/978-981-10-8031-9.
6. Terzioğlu, P., Öğüt, H. & Kalemtaş, A. Natural calcium phosphates from fish bones and their potential biomedical applications. *Mater. Sci. Eng. C* **91**, 899–911 (2018).
7. Boutinguiza, M. *et al.* Biological hydroxyapatite obtained from fish bones. *Mater. Sci. Eng. C* **32**, 478–486 (2012).
8. Araujo, J., Sica, P., Costa, C. & Márquez, M. C. Enzymatic Hydrolysis of Fish Waste as an Alternative to Produce High Value-Added Products. *Waste and Biomass Valorization* **12**, 847–855 (2021).
9. Piccirillo, C. *et al.* Luminescent calcium phosphate bioceramics doped with europium derived from fish industry byproducts. *J. Am. Ceram. Soc.* **100**, 3402–3414 (2017).
10. Maidaniuc, A. *et al.* Effect of the processing parameters on surface, physico-chemical and mechanical features of bioceramics synthesized from abundant carp fish bones. *Ceram. Int.* **46**, 10159–10171 (2020).
11. Radziemska, M., Vaverková, M. D., Adamcová, D., Brtnický, M. & Mazur, Z. Valorization of Fish Waste Compost as a Fertilizer for Agricultural Use. *Waste and Biomass Valorization* **10**, 2537–2545 (2019).
12. Field, C.B., V.R. Barros, D.J. Dokken, K.J. Mach, M. D. M., T.E. Bilir, M. Chatterjee, K.L. Ebi, Y.O. Estrada, R.C. Genova, B. Girma, E.S. Kissel, A.N. Levy, S. M. & P.R. Mastrandrea, and L. L. W. (eds. . IPCC, 2014: Summary for policymakers. In: Climate Change 2014: Impacts, Adaptation, and Vulnerability. Part A: Global and

Sectoral Aspects. Contribution of Working Group II to the Fifth Assessment Report of the Intergovernmental Panel on Climate Change. *Cambridge Univ. Press. Cambridge, United Kingdom New York, NY, USA* 1–32 (2014).

13. Glæsner, N., Hansen, H. C. B., Hu, Y., Bekiaris, G. & Bruun, S. Low crystalline apatite in bone char produced at low temperature ameliorates phosphorus-deficient soils. *Chemosphere* **223**, 723–730 (2019).
14. Zhang, C. *et al.* Biochar for environmental management: Mitigating greenhouse gas emissions, contaminant treatment, and potential negative impacts. *Chem. Eng. J.* **373**, 902–922 (2019).
15. Ippolito, J. A., Laird, D. A. & Busscher, W. J. Environmental Benefits of Biochar. *J. Environ. Qual.* **41**, 967–972 (2012).
16. González-Cencerrado, A., Ranz, J. P., López-Franco Jiménez, M. T. & Gajardo, B. R. Assessing the environmental benefit of a new fertilizer based on activated biochar applied to cereal crops. *Sci. Total Environ.* **711**, 134668 (2020).
17. Camacho, N. P., West, P., Torzilli, P. A. & Mendelsohn, R. FTIR microscopic imaging of collagen and proteoglycan in bovine cartilage. *Biopolymers* **62**, 1–8 (2001).
18. Metreveli, N. O. *et al.* UV–vis and FT-IR spectra of ultraviolet irradiated collagen in the presence of antioxidant ascorbic acid. *Ecotoxicol. Environ. Saf.* **73**, 448–455 (2010).
19. Iafisco, M. *et al.* Nanocrystalline carbonate-apatites: role of Ca/P ratio on the upload and release of anticancer platinum bisphosphonates. *Nanoscale* **4**, 206–217 (2012).
20. Degli Esposti, L., Carella, F., Adamiano, A., Tampieri, A. & Iafisco, M. Calcium phosphate-based nanosystems for advanced targeted nanomedicine. *Drug Dev. Ind. Pharm.* **44**, 1223–1238 (2018).
21. Lim, K.-T. *et al.* Evaluation of Bone Regeneration Potential of Long-Term Soaked Natural Hydroxyapatite. *ACS Appl. Bio Mater.* **2**, 5535–5543 (2019).
22. Ozawa, M. & Suzuki, S. Microstructural Development of Natural Hydroxyapatite Originated from Fish-Bone Waste through Heat Treatment. *J. Am. Ceram. Soc.* **85**, 1315–1317 (2004).
23. Nehlich, O. & Richards, M. P. Establishing collagen quality criteria for sulphur isotope analysis of archaeological bone collagen. *Archaeol. Anthropol. Sci.* **1**, 59–

75 (2009).

24. Neuman, W. F. & Mulryan, B. J. The discrepancy in the carbonate found in fish bone and blood. *Calcif. Tissue Res.* **2**, 237–241 (1968).
25. Brunson, L. R. & Sabatini, D. A. An Evaluation of Fish Bone Char as an Appropriate Arsenic and Fluoride Removal Technology for Emerging Regions. *Environ. Eng. Sci.* **26**, 1777–1784 (2009).
26. Marchiol, L. *et al.* Influence of Hydroxyapatite Nanoparticles on Germination and Plant Metabolism of Tomato (Solanum lycopersicum L.): Preliminary Evidence. *Agronomy* **9**, 161 (2019).
27. Montalvo, D., McLaughlin, M. J. & Degryse, F. Efficacy of Hydroxyapatite Nanoparticles as Phosphorus Fertilizer in Andisols and Oxisols. *Soil Sci. Soc. Am. J.* **79**, 551–558 (2015).
28. Savy, D. *et al.* Quantitative Structure-Activity Relationship of Humic-Like Biostimulants Derived From Agro-Industrial Byproducts and Energy Crops. *Front. Plant Sci.* **11**, (2020).
29. Rico, C. M., Majumdar, S., Duarte-Gardea, M., Peralta-Videa, J. R. & Gardea-Torresdey, J. L. Interaction of Nanoparticles with Edible Plants and Their Possible Implications in the Food Chain. *J. Agric. Food Chem.* **59**, 3485–3498 (2011).
30. Siddiqui, M. H. & Al-Whaibi, M. H. Role of nano-SiO2 in germination of tomato (Lycopersicum esculentum seeds Mill.). *Saudi J. Biol. Sci.* **21**, 13–17 (2014).

7. Conclusion and future perspectives

CaPs constitute the inorganic component of hard tissues in vertebrates and their main known application is in medicine, because of their high biocompatibility, bioactivity, lack of toxicity or inflammatory and immunity responses, osteoconductivity, osteoinductivity and bioresorbability. The physical and chemical characteristics of these materials are related to their functions and can be tailored modifying the parameters in CaP synthesis. CaPs are widely present in nature and therefore, they can be also prepared in several ways from biogenic sources. Focusing on the food wastes, the rapid growth of the fish industry has increased the interest to face the high amount of fish waste to be treated. Therefore, the evaluation of fish bones as a source of CaPs has recently gained the attention of researchers.

The aim of this thesis consisted in the preparation of CaPs with both traditional and innovative methods, followed by the evaluation of the materials achieved for several applications.

In detail, the first materials prepared in this Ph.D. thesis was developed by wet chemical processes for biomedical applications. The study provides the proof of concept for an innovative inhalable CaP NP based drug delivery system potentially able to counteract PA infection in CF. The results have demonstrated that CaP NPs can be functionalized with antimicrobial Col through electrostatic interaction between the positively charged amine groups of Col and the negatively charged surface of CaP NPs. Furthermore, it was observed that the CaP NPs can penetrate a layer of artificial mucus and the adsorbed Col on CaP-NPs retains its therapeutic effect presenting antimicrobial and antibiofilm efficacy similar to free Col. In this first part of the thesis, a novel promising nanomaterial in the treatment of CF to overcame antibiotics resistance was developed.

The second material reported along this work was a 3D porous scaffold developed for the bone regeneration and prepared from natural sources (mussel shells). The obtained CaP powder achieved from the thermal treatment of mussel shells was used to prepare a macroporous 3D scaffold by direct foaming technique. The chemical, physical and mechanical requisites to produce a scaffold suitable to be used as bone substitute were achieved, but further studies regarding the *in vitro* and *in vivo* behaviour of this kind of scaffolds must be performed.

In the third part of this Ph.D. thesis, a novel and safe CaP-based ingredient for sunscreen formulations was designed, prepared and optimized from natural sources (fish bones). In particular, it was studied a material able to enhance the sun protection factor (SPF) of a solar formulation, called “SPF booster”. The results obtained demonstrated that it was possible to increase the SPF value of a sunscreen formulation by introducing natural CaP-based SPF boosters. This innovative material constituted an interesting alternative to synthetic raw materials, a step towards the circular economy in the cosmetic sector, and a possible answer to the industry waste management. On the other hand, further studies are needed to better investigate and understand how doping with photoactive elements can lead to improve CaP-N performances as SPF boosters.

The last part of this thesis was focused on the development of a circular economy for P reuse also in the least developed countries (LDCs). In particular, CaP-based waste materials were easily processed and tested for fertilizer application in agriculture. It was demonstrated that it is possible to convert fish bone into materials with a higher potential value for the agricultural market by a straightforward and easily scalable thermal process that could be applied at the community level in LDCs. The obtained materials showed very good potential as bio stimulant for corn coleoptile and as corn fertilizer. In future, to improve the biostimulant effect of these materials, the adsorption of humic substances could be developed, as they are commonly used for this purpose.

To sum up, the results obtained in this Ph.D. thesis demonstrated the tunability of CaPs in both their properties and thus their applications. Marine wastes can constitute an interesting sustainable source for the development of high added value CaP-based systems for biomedical, cosmetic and agriculture applications. In the future, the use of biowastes as a source for the production of CaPs for several kinds of applications could represent an innovative approach for both economic and environmental point of view.

List of publications

1. L. Degli Esposti, **F. Carella**, M. Iafisco*, *Inorganic nanoparticles for theranostic use*, Electrofluidodynamic Technologies (EFDTs) for Biomaterials and Medical Devices, Chapter 17, (pp.351-376), 2018.
   DOI: 10.1016/B978-0-08-101745-6.00017-7
2. L. Degli Esposti, **F. Carella**, A. Adamiano, A. Tampieri, M. Iafisco*, *Calcium phosphate-based nanosystems for advanced targeted nanomedicine*, Drug development and industrial pharmacy, 44(8), (pp.1223-1238), 2018.
   DOI: 10.1080/03639045.2018.1451879
3. M. Iafisco*, L. Degli Esposti, G. B. Ramìrez-Rodriguez, **F. Carella**, J. Gòmez-Morales, A. C. Ionescu, E. Brambilla, A. Tampieri, J. M. Delgado-Lòpez*, *Fluoride-doped amorphous calcium phosphate nanoparticles as a promising biomimetic material for dental remineralization*, Scientific Reports, 8(1), (pp.1-9), 2018.
   DOI: 10.1038/s41598-018-35258-x
4. **F. Carella**, L. Degli Esposti, D. Barreca, G. A. Rizzi, G. Martra, P. Ivanchenko, G. E. Casado, J. G. Morales, J. M. Delgado Lòpez, A. Tampieri, M. Iafisco*, *Role of citrate in the formation of enamel-like calcium phosphate oriented nanorod arrays*, CrystEngComm, 21(32), (pp.4684-4689), 2019.
   DOI: 10.1039/C9CE00508K
5. A. Adamiano, V. M. Wu, **F. Carella**, G. Lamura, F. Canepa, A. Tampieri, M. Iafisco*, V. Uskokovic*, *Magnetic calcium phosphates nanocomposites for the intracellular hyperthermia of cancers of bone and brain*, Nanomedicine, 14(10), (pp.1267-1289), 2019.
   DOI: 10.2217/nnm-2018-0372
6. A. Lolli, M. Blosi*, S. Ortelli, A. L. Costa, I. Zanoni, D. Bonincontro, **F. Carella**, S. Albonetti*, *Innovative synthesis of nanostructured composite materials by a spray-freeze drying process: Efficient catalysts and photocatalysts preparation*, Catalysis Today, 334, (pp.193-202), 2019.
   DOI: 10.1016/j.cattod.2018.11.022

7. C. Velino, **F. Carella**, A. Adamiano, M. Sanguinetti, A. Vitali, D. Catalucci, F. Bugli*, M. Iafisco*, *Nanomedicine Approaches for the Pulmonary Treatment of Cystic Fibrosis, Frontiers in bioengineering and biotechnology*, 7, (pp.406), 2019.
DOI: 10.3389/fbioe.2019.00406
8. S. Scialla, **F. Carella**, M. Dapporto, S. Sprio, A. Piancastelli, B. Palazzo, A. Adamiano, L. Degli Esposti, M. Iafisco*, C. Piccirillo*, *Mussel Shell-Derived Macroporous 3D Scaffold: Characterization and Optimization Study of a Bioceramic from the Circular Economy*, Marine Drugs 18(6), (pp.309), 2020.
DOI: 10.3390/md18060309
9. A. Adamiano*, G. Fellet, M. Vuerich, D. Scarpin, **F. Carella**, C. Piccirillo, J. R. Jeon, A. Pizzutti, L. Marchiol, M. Iafisco, *Calcium Phosphate Particles Coated with Humic Substances: A Potential Plant Biostimulant from Circular Economy*, Molecules, 26(9), (pp.2810), 2021.
DOI: 10.3390/molecules26092810
10. **F. Carella**, L. Degli Esposti, A. Adamiano, M. Iafisco*, *The Use of Calcium Phosphates in Cosmetics, State of the Art and Future Perspectives*, Materials, 14(21), (pp.6398), 2021.
DOI: 10.3390/ma14216398
11. **F. Carella**, M. Seck, L. Degli Esposti, H. Diadiou, A. Maienza, S. Baronti, P. Vignaroli, F. P. Vaccari, M. Iafisco, A. Adamiano*, *Thermal conversion of fish bones into fertilizers and biostimulants for plant growth – A low tech valorization process for the development of circular economy in least developed countries*, Journal of Environmental Chemical Engineering, 9(1), (pp.104815), 2021.
DOI: 10.1016/j.jece.2020.104815
12. M. Iafisco, **F. Carella**, L. Degli Esposti, A. Adamiano, D. Catalucci, J. Modica, A. Bragonzi, A. Vitali, R. Torelli, M. Sanguinetti, F. Bugli, *Biocompatible antimicrobial colistin loaded calcium phosphate nanoparticles for the counteraction of biofilm formation in cystic fibrosis related infections*, Journal of Inorganic Biochemistry - submitted
13. L. Degli Esposti, A. C. Ionescu, **F. Carella**, A. Adamiano, E. Brambilla and M. Iafisco, *Antimicrobial activity of remineralizing ion-doped amorphous calcium phosphates for preventive dentistry*, Frontiers in Materials, section Biomaterials - submitted

Scientific contributions to congresses and schools

1. F. Carella, A. Adamiano, A. Tampieri and M, Iafisco. *From food industry byproduct to phosphorous fertilizers and sunscreen applications*, Summer School in Making business with green chemistry and sustainable energy, Sarteano, Italy 2019, Best poster award.
2. F. Carella, M. Iafisco, M. Seck, H. Diadhiout, A. Tampieri and A. Adamiano. *PhosFATE: from food industry by-product to phosphorous fertilizers*, 4th Green and Sustainable Chemistry Conference, Dresden, Germany, 2019.
3. F. Carella, A. Adamiano and M. Iafisco. *From food industry by-product to a novel UV filters production for sunscreen applications*, NANO-DAY IV, Milano, Italy, 2019.
4. F. Carella, C. Velino, L. Degli Esposti, A. Adamiano, F. Bugli, M. Sanguinetti, A. Vitali, D. Catalucci, A. Tampieri and M. Iafisco. *Antimicrobial-loaded calcium phosphate nanoparticles as a potential new therapy for cystic fibrosis-related infections*, International School of Chemistry (Web Edition) "Chemistry for Everyday life", Camerino, Italy (converted to web edition), 2020.
5. F. Carella, C. Velino, L. Degli Esposti, A. Adamiano, F. Bugli, M. Sanguinetti, A. Vitali, D. Catalucci, A. Tampieri and M. Iafisco. *Antimicrobial-loaded calcium phosphate nanoparticles for the counteraction of biofilm formation and antibiotic resistance: towards a potential new therapy for cystic fibrosis related infections, 11th World Biomaterials Congress.* Glasgow, Scotland (converted to web edition), 2020.
6. F. Carella, F. Bugli, A. Rossi, L. Degli Esposti, A. Adamiano, M. Sanguinetti, A. Bragonzi, A. Vitali, D. Catalucci and M. Iafisco. *Colistin-loaded calcium phosphate nanoparticles as drug delivery system for the treatment of infections related to cystic fibrosis*, Congresso Nazionale Biomateriali (SIB 2021), Lecce, Italy, 2021.